Quantifying Polymer Chain Orientation in Strong and Tough Nanofibers with Low Crystallinity: Towards Next Generation Nanostructured Superfibers

*Dimitry Papkov[1,2], Nicolas Delpouve[3], Laurent Delbreilh[3], Steven Araujo[3], Taylor Stockdale[1], Sergey Mamedov[4], Kaspars Maleckis[1†], Yan Zou[1§], Mohammad Nahid Andalib[1], Eric Dargent[3], Vinayak Dravid[5], Martin V. Holt[6], Christian Pellerin[7], Yuris A. Dzenis[1,2]**

[1]Department of Mechanical and Materials Engineering, University of Nebraska-Lincoln, Lincoln, NE 68588-0526

[2]Nebraska Center for Materials and Nanoscience, University of Nebraska-Lincoln, Lincoln, NE 68588-0298

[3]Département Systèmes Désordonnés et Polymères, Equipe Internationale de Recherche et de Caractérisation des Amorphes et des Polymères, Normandie Univ, UNIROUEN, INSA ROUEN, CNRS, GPM, 76000 Rouen, France

[4]HORIBA Scientific, Division of HORIBA Instruments, Inc., 20 Knightsbridge Road, Piscataway, NJ 08854

[5]Department of Materials Science and Engineering, Northwestern University, Evanston, IL 60208

[6]Center for Nanoscale Materials, Argonne National Laboratory, Argonne, IL 60439

[7]Département de chimie, Université de Montréal, Montréal, QC H3C 3J7, Canada

Current Addresses:

[†]Department of Surgery, University of Nebraska Medical Center, Omaha, NE, 68198-7690

[§]Department of Mechanics, Huazhong University of Science and Technology, Wuhan, Hubei, China, P.C. 430074

*Correspondence to: ydzenis@unl.edu

ToC Figure

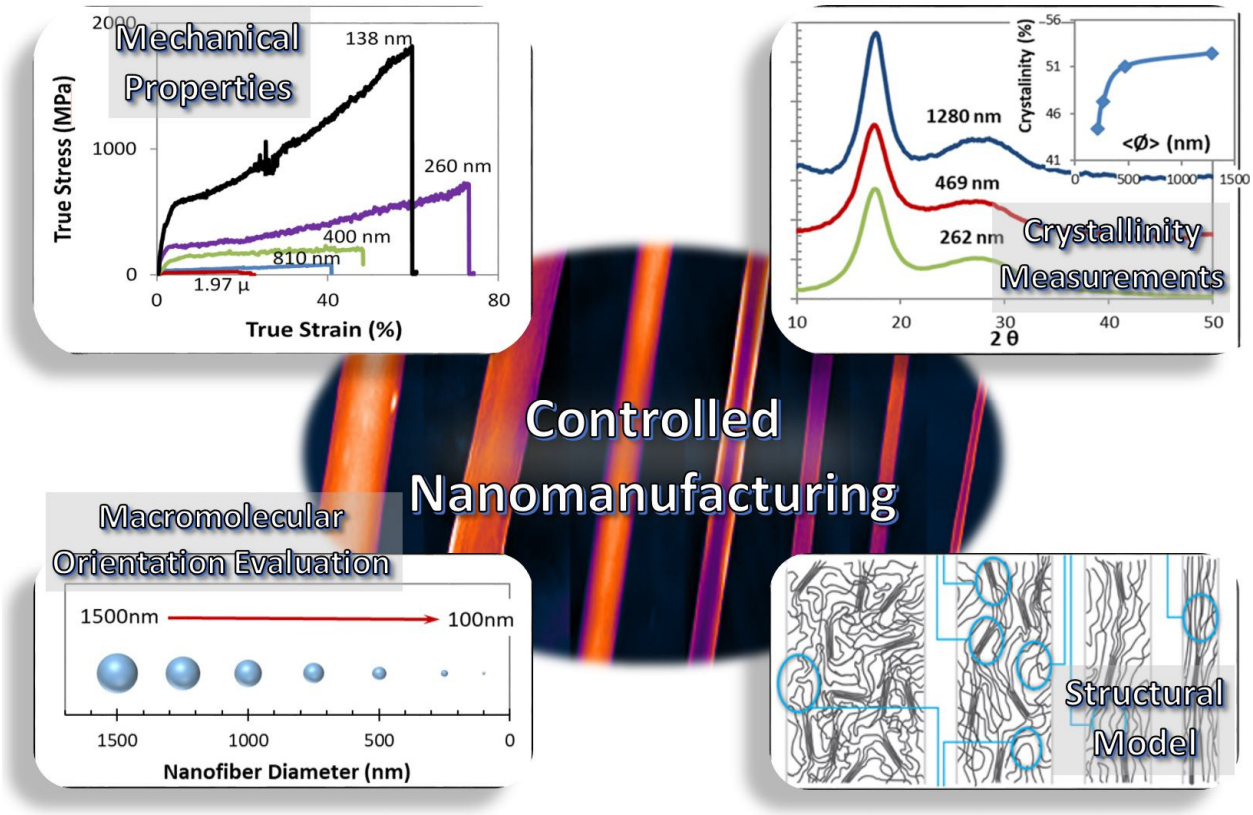

Table of Contents

Abstract

Advanced fibers revolutionized structural materials in the second half of the 20th Century. However, all high-strength fibers developed to date are brittle. Recently, pioneering simultaneous ultrahigh strength and toughness were discovered in fine (<250 nm) individual electrospun polymer nanofibers (NFs). This highly desirable combination of properties was attributed to high macromolecular chain alignment coupled with low crystallinity. Quantitative analysis of the degree of preferred chain orientation will be crucial for control of NF mechanical properties. However, quantification of supramolecular nanoarchitecture in NFs with low crystallinity in the ultrafine diameter range is highly challenging. Here, we discuss applicability of traditional as well as emerging methods for quantification of polymer chain orientation in nanoscale one-dimensional samples. Advantages and limitations of different techniques are critically evaluated on experimental examples. It is shown that straightforward application of some of the techniques to subwavelength-diameter NFs can lead to severe quantitative and even qualitative artifacts. Sources of such size-related artifacts, stemming from instrumental, materials, and geometric phenomena at the nanoscale, are analyzed on the example of polarized Raman method, but are relevant to other spectroscopic techniques. A proposed modified, artifact-free method is demonstrated. Outstanding issues and their proposed solutions are discussed. The results provide guidance for accurate nanofiber characterization to improve fundamental understanding and accelerate development of nanofibers and related nanostructured materials produced by electrospinning or other methods. We expect that the discussion in this review will also be useful to studies of many biological systems that exhibit nanofilamentary architectures and combinations of high strength and toughness.

Keywords: electrospinning, nanofibers, macromolecular orientation, polymer chain alignment, size dependent artifacts

1. Introduction: The Need for Quantitative Evaluation of Macromolecular Orientation

Nanomaterials and nanotechnology have the potential to produce the next step change in materials research and form the basis for the new generation of advanced fibers and composites. Ever since the discovery of carbon nanotubes, and more recently graphene and graphene oxide, and the measurement of their extraordinary mechanical properties, intensive research effort has been devoted to translating these properties to the macro scale. However, so far, the mechanical properties of nanocomposites, using these materials, have fallen well below properties of existing advanced fiber-reinforced composites, and multiple fundamental problems remain.[1,2] At their core, these problems are associated with the discontinuous nature of these nanoparticles.[3,4]

Continuous nanofibers (NFs) represent an emerging class of nanomaterials with critical advantages for structural and functional applications.[5,6] Continuous NFs are expected to possess enhanced and unusual properties, unavailable in micron-sized fibers, while at the same time alleviating processing problems associated with discontinuous nanomaterials produced by bottom-up synthetic methods. Electrospinning is a technique that produces continuous NFs by jetting polymer solutions in high electric fields. The process in its simplest form results in random nonwoven nanofiber mats. However, techniques for aligned assemblies and individual nanofiber production are also available. Unique combination of nano- and macro- dimensions in electrospun NFs and relative ease of their fabrication, handling, and processing into applications explain rapidly growing interest in continuous NFs for a variety of applications from tissue engineering[7,8] to electronics and opto-electronics.[9–11] Ultra-high electrospinning draw ratios of

up to five orders of magnitude, unheard of in traditional manufacturing techniques, hold promise of extraordinary mechanical properties. However, to date, electrospun NFs were considered mechanically weak.

Recently, we have reported dramatic size effects in mechanical properties of individual electrospun polyacrylonitrile (PAN) NFs.[12] Contrary to the classical strength/ductility trade-off in structural materials, nanofibers exhibited simultaneous increases in strength, modulus, and toughness with the decrease in NF diameter (see Fig. 1). Major improvements were observed in the ultrafine diameter range (<250 nm). Similar behavior was later observed in other polymer systems, extending to diameters as low as a few tens of nanometers. Some biological systems with comparable-sized substructures have also demonstrated combination of high toughness and strength. Such a combination of simultaneously high mechanical properties is extremely rare but very desirable in virtually any engineering application.[13] It can reduce the need for overdesign resulting in unnecessary large factors of safety in current structures. Materials with simultaneously high strength and toughness are considered to be "The Holy Grail" of structural materials research.[13] However, despite several important advances, no definitive progress has been yet achieved in this area and all structural materials that are in use today suffer from classical strength-toughness trade-off.

In conventional advanced polymer fibers, specialized manufacturing techniques, such as liquid crystalline- and gel- spinning, have been developed to achieve high polymer chain alignment, leading to extraordinary strength and modulus. However, polymer chain alignment in these fibers is accompanied by high crystallinity, leading to linearly elastic deformation with low strain at failure and toughness. Strain at failure of all current advanced polymer fibers does not exceed 5% (some developmental fibers, such as carbon nanotube and graphene based fibers, as

well as biological fibers such as spider silk can exhibit higher strains to failure, but they are generally not classified as advanced fibers due to their relatively low strength).

In contrast, low and reducing crystallinity was verified experimentally in electrospun PAN NFs with decreasing NF diameters.[12] Similarly, low crystallinity was observed in other studies of PAN[14,15] and other electrospun polymer systems.[16–19] Low NF crystallinity resulted in persistent elasto-plastic deformation with high (tens to hundred percent) strains at failure and ultrahigh toughness. The observed low and decreasing crystallinity is unusual, as fibers of smaller diameters are expected to have improved polymer chain alignment. This, in turn, should lead to increased polymer crystallinity.

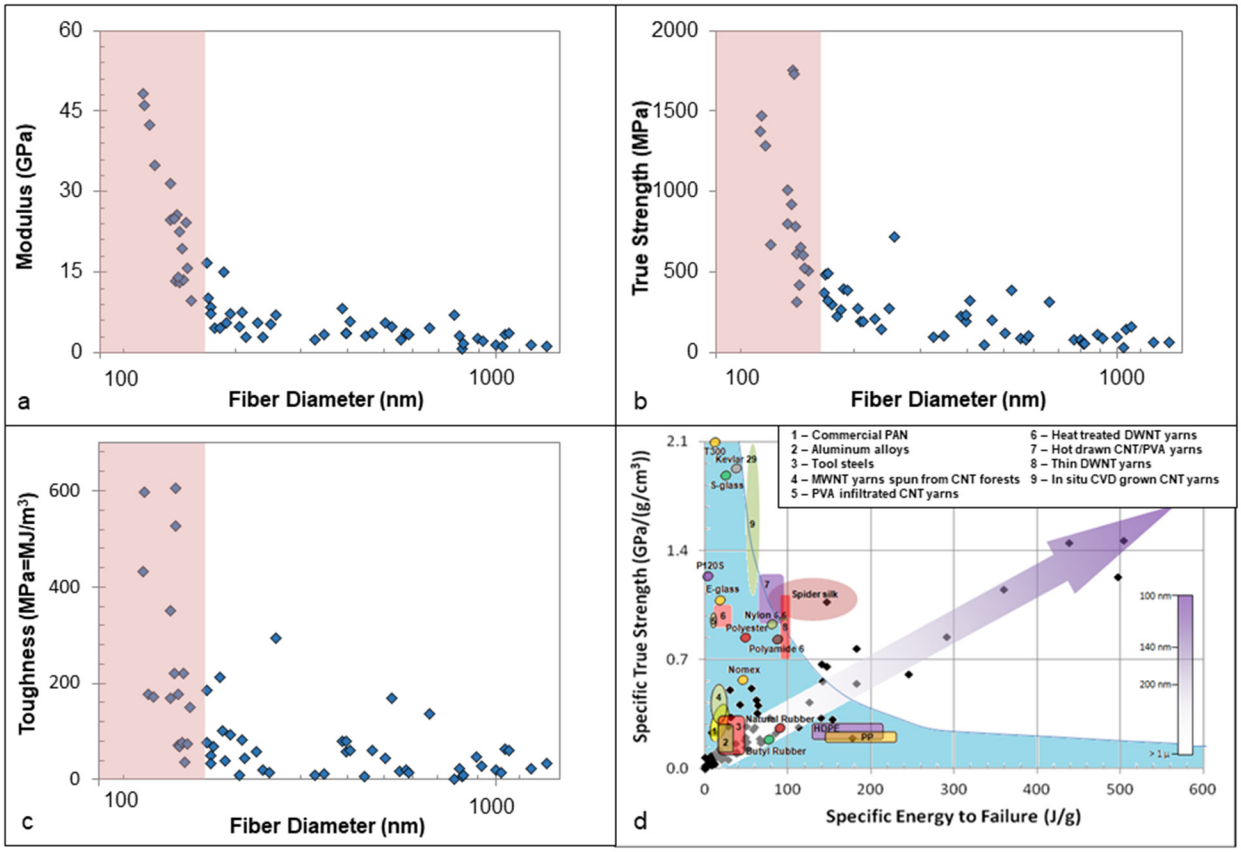

Figure 1: Simultaneous increases in strength, modulus, and toughness of individual electrospun PAN NFs. Size effects in (a) Modulus; (b) True strength, and (c) Toughness (as defined by the area under the stress/strain curve). (d) Comparison of specific strength and energy to failure in

NFs and typical commercial and developmental fibers and materials[20–26] (adapted from ref 12). The shaded area in panels (a)-(c) corresponds to the diameter region of highest interest.

One possible reason for this unusual combination of high degree of chain alignment and low crystallinity is ultra-fast solvent evaporation during electrospinning[27] that can act similarly to fast quenching in traditional manufacturing processes and retard crystallization. The exact range of crystallinities in electrospun nanofibers will depend on the polymer system and nanomanufacturing conditions. For example, crystallinities in ultrafine electrospun PAN and Nylon 6 NFs produced in our lab were as low as 40% and 50% (compare this to typical 75-95% crystallinities of conventional high-strength polymer fibers). This resulting low crystallinity canlead to retention of high NF deformability, beyond the yield point, and to ultrahigh toughness. In summary, the observed simultaneous high strength and modulus are thus attributed to high preferred polymer chain orientation. On the other hand, high toughness is the result of low crystallinity (see schematic of the structural model of electrospun NFs in Fig. 2). Thus, the discovered properties stem from an unusual structure, resulting from inherent and unique peculiarities of the electrospinning process, unachievable thus far in conventional manufacturing technologies that rely on orders of magnitude slower solvent removal from the 100-1,000 times thicker polymer jets.

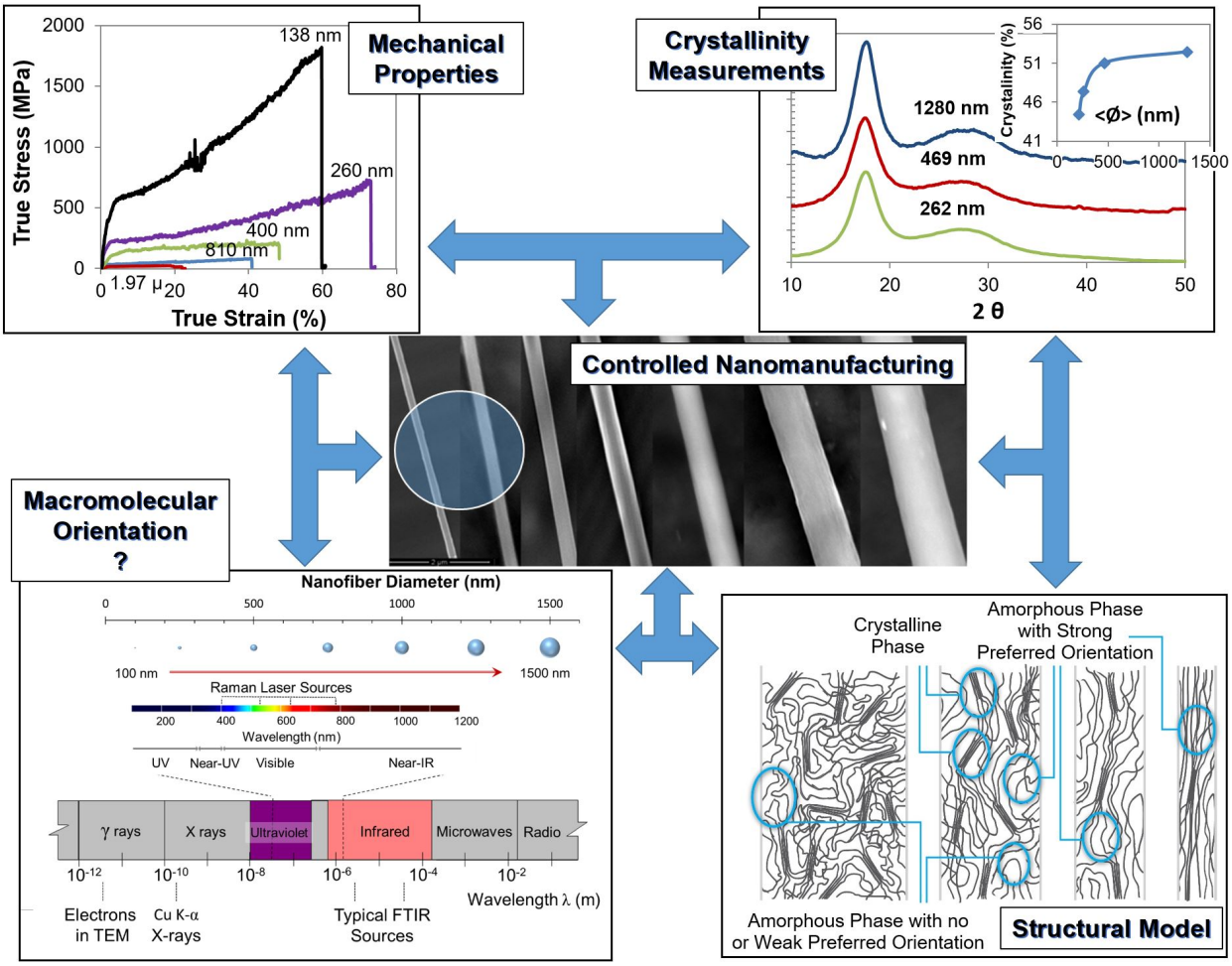

Figure 2: Towards the development of supernanofiber. Manufacturing/Structure/Properties relationship schematic. The bottom left panel illustrates the critically needed information on polymer chain orientation in ultrafine individual NFs.

Alignment of polymer chains is expected to improve with the reduction of NF diameter due to increased draw ratios and confinement effects. Increases in NF modulus (see Fig. 1a) must correlate with improved polymer chain alignment. Direct experimental quantification of orientation is critical for the materials development and properties optimization (see schematic in Fig. 2). In the past, in-depth studies of structure-properties relationships of advanced fibers[28–30] led to their extraordinary properties and their presence as a dominant force among the structural materials today. A similar understanding of structure/properties relationship in electrospun nanofibers can produce the next generation of advanced fibers. However, electrospun NFs are

two to four orders of magnitude thinner than the conventional mechanically spun fibers, making interrogation of individual nanofilaments extremely difficult. On the other hand, inherent instabilities of the electrospinning process[27] result in difficulties with preparation of perfectly aligned monodisperse NF bundles that could, in theory, overcome the problems associated with experimental analysis of individual NFs. Due to these difficulties, to date, only a limited number of studies of polymer chain orientation in electrospun NFs was performed[31] (see Table S1 in Supplementary Information, SI, for a list of prior orientation studies in electrospun NFs).

The goal of this review is to critically evaluate characterization techniques that can provide orientation information for fine NFs produced by electrospinning or other nanofabrication methods (see bottom left panel in Fig. 2). The discussion is also relevant to biological materials with nanofibrillar architecture. Several traditional as well as emerging orientation characterization techniques are reviewed. Their applicability for examination of fine NFs is analyzed and demonstrated on experimental examples that were specifically prepared and analyzed for the purpose of this paper. It is shown that each of the described techniques can provide valuable information, but also faces unique challenges. In the discussion below, the methods are grouped into those that require bundles/mats of NFs and those that can be used on individual NFs. Advantages and limitations are discussed within the context of ultrafine-diameter NFs. Polarized Raman microscopy, as a technique with high immediate potential, is examined in depth. Possible artifacts related to applications of different techniques to subwavelength-diameter NFs (*i.e.*, simultaneously strong and tough NFs of the highest interest for structural applications) are described in depth for the first time, and ways to overcome them are proposed. Although the artifacts are described on an example of polarized Raman method, the discussion is

relevant to other spectroscopic techniques as well. Finally, future outlook and outstanding issues are discussed.

2. Methods of Orientation Evaluation that Require Nanofiber Mats or Bundles

2.1. X-ray Diffraction

X-ray diffraction (XRD) relies on the interaction of X-rays with crystalline material. Diffraction patterns obtained are then used to recreate the three-dimensional arrangement of atoms within the material crystals. XRD can be used to estimate degree of crystallinity in semi-crystalline polymers. The interaction between X-ray radiation and the material is generally weak. As a result, even radiation sensitive materials such as polymers can be examined by XRD without significant damage. However, due to this weak interaction, the observed signal is also relatively weak. Consequently, XRD requires relatively large amount of material, and cannot generally be used to examine individual NFs (see discussion on potential use of X-ray microscopy in individual NF studies in Section 7.1). Random NF mats can be used for the quantification of polymer crystallinity,[12] while oriented bundles can generally be used for orientation studies.[32–35]

An example of the application of XRD to examine crystal orientation in PAN NF bundles is shown in Figure 3. Bundles with different average diameters were examined (see Fig. 3a,d for SEM images). Diameter distribution (see Fig. 3b,e), and relative degree of fiber alignment within the bundle (see Fig. 3c,f) were constructed. 2D XRD pattern for the bundles was recorded (see the left part of Fig. 3g,h).

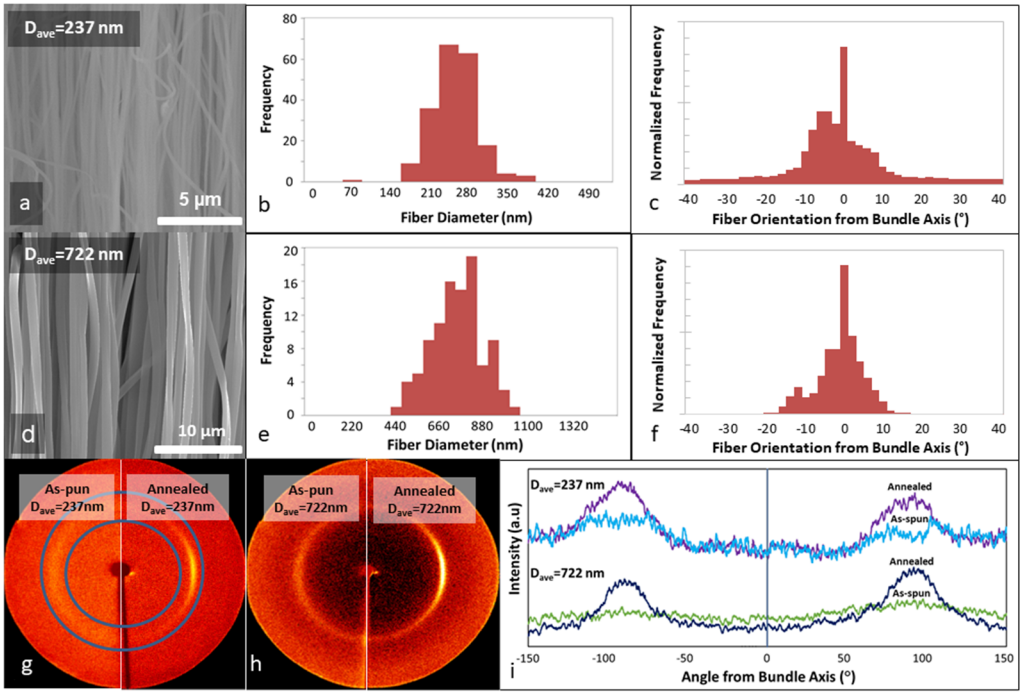

Figure 3: Evaluation of crystal orientation using XRD. (a), (d) SEM images of the examined NF bundles with two different average diameters; (b), (e) NF diameter distribution within the bundles; (c), (f) Orientation distribution of NFs within the bundles; (g), (h) 2D XRD diffractogram of the different bundles in panels (a) and (d). The left part of the diffractograms is for as-spun bundles, and the right part is for the same bundles annealed at 130°C at constant bundle length; (i) Extracted azimuthal scans for the arcs corresponding to the crystal peaks. The intensity is integrated between the two concentric circles as shown in panel (g).

Consistent with the previous results,[12] crystallinity in as-spun bundles was low (as evidenced by the diffuse arcs in the left part of Fig. 3g,h). The 2D plots can generally be used to qualitatively compare the crystal orientation in the different samples. For quantitative examination of crystal orientation, an azimuthal scan of intensity as a function of angle from the bundle axis can be obtained (see Fig. 3i) by integrating the intensity under the crystalline reflection at 2θ~17° (see the area marked by two concentric circles in Fig. 3g). The degree of preferred crystal orientation is then sometimes expressed by evaluating the full width at half maximum of the peaks (FWHM) corresponding to the arcs in the XRD diffractogram. This approach is commonly used, for example, for examining commercial carbon fibers.[36] A second

order parameter of the orientation distribution function, also called the Herman function, $\langle P_2 \rangle$, can also be extracted and analyzed.[37]

As seen in the left parts of the panels 3g,h, preferred crystal orientation was observed in as-spun NF bundles. However, low crystallinity led to very low signal to noise ratio (see Fig. 3i). As a result, evaluation of FWHM corresponding to the crystal arcs was difficult.

Crystallinity of polymer NFs can be increased by annealing. Right part of Figures 3g,h shows the diffractogram for the bundles annealed at 130°C. More pronounced preferred crystal orientation (as expressed by sharper peaks in Fig. 3i) is evident. FWHM can generally be computed for the crystalline arcs in the annealed samples. However, crystallization is a complex phenomenon. It is impacted by additional parameters beyond the degree of macromolecular alignment in as-spun NFs. As a result, caution should be exercised in relating the information on the crystal orientation in the annealed samples to the original chain orientation in largely amorphous as-spun NFs.

Two additional effects complicate the relationship between chain orientation in the NFs and the one observed in XRD. First, as can be seen in Figures 3c,f, NFs are not perfectly aligned along the bundle axis. Consequently, the orientation seen in XRD is a combination of orientation of NFs within the bundles, and of crystals within individual NFs. The second effect is that of NF diameter polydispersity (see diameter distributions in Fig. 3b,e). The degree of preferred orientation is expected to be different for NFs with different diameters. As a result, NF diameter polydispersity will confound the interpretation of XRD orientation results.

2.2. Polarized Fourier Transform Infrared Spectroscopy

Polarized Fourier Transform Infrared Spectroscopy (FTIR) is another technique to investigate orientation in polymers. Each infrared band corresponds to a specific vibrational

mode within the polymer structure, thereby providing orientation information with molecular selectivity. Jasse and Koenig[38] provided a detailed description of the use of polarized FTIR for quantitative characterization of polymer chain orientation. The polarized absorption of a given IR band is proportional to the square of the dot product between the transition dipole moment vector and the electric field polarization vector of the incoming radiation. For a simple localized vibration such as the nitrile stretching band of PAN, the transition dipole moment is along the bond axis. Consequently, orientation information can be obtained from dichroic ratio (ratio of absorption intensities of orthogonally polarized light).[39,40] When the conformation of the molecule is known, dichroic ratio can be converted into a Herman orientation function, $\langle P_2 \rangle$ (see details in SI).

Contrary to XRD, polarized FTIR can provide information on orientation in both crystalline and amorphous phases. However, it is still limited in its applicability to NFs. In particular, the minimal spot size achievable by focusing the beam using a far-field microscope is on the order of 5-10 micrometers because of the large wavelengths of IR radiation. This strongly reduces the signal to noise ratio for individual NFs since their diameter is significantly smaller than the spot size and leads to quantification errors due to stray light.[41] As a result, similarly to XRD, FTIR measurements are normally conducted on large bundles or mats of NFs using a large spot size of several hundreds of micrometers.[32,33,42–44]

Example of polarized FTIR examination was carried on PAN NF bundles. In case of PAN orientation information can be obtained by examining the bands associated with the nitrile group and the different CH vibrations.[45] There are several overlapping peaks in the CH region, which require band fitting and assignment. On the other hand, the nitrile stretching band is prominent and is isolated from other bands. As a result, evaluation of the infrared dichroism of

the nitrile stretching mode is the most common approach. The molecular conformation of PAN is that of an irregular helix.[46] The angles between the nitrile groups and the axis of this helix are not constant, but several studies have estimated the average α angle to be in the vicinity of 70°.[39,47] As a result, if preferred chain orientation is present, the absorbance with the polarization parallel to the fiber is expected to be smaller than the one with polarization perpendicular to the fiber, resulting in dichroic ratios less than 1. However, because the α angle is significantly smaller than 90°, the dichroic ratio of PAN nitrile band is not expected to be very small even in the presence of significant degree of preferred backbone chain orientation (R is approximately 0.32 for $<P_2>$ of 0.9). Herman orientation factor was extracted in the past for uniaxially drawn PAN films.[39,47] Examination of oriented electrospun NF bundles was attempted as well (see discussion below).[15]

Oriented bundles of NFs with different average diameters were examined in this work by polarized FTIR in transmission (suspended fibers) and in transflection (fibers on an aluminum foil) modes. The transmission FTIR spectra shown in Figure 4a for the bundle with average NF diameter of 500 nm present a very pronounced baseline drift toward higher wavenumbers due to light scattering (similar results are obtained by transflection). Such scattering is commonly observed for samples dispersed in a matrix, such as KBr pellets, due to refractive index contrast between the sample and matrix. It is maximal at wavelengths similar to the size of the particles. In the case of nanofibers, scattering is due to the refractive index mismatch between the fibers and the air between fibers. It therefore depends on the NFs diameter and average distance between NFs in the bundle. The scattering amplitude is systematically larger for light polarized parallel to the fibers. This could be explained by large differences in the spatial variation of refractive index between the fibers and air (amplitude and periodicity) with light polarized along

or perpendicular to the fiber bundle axis, as well as differences in the curvature of the objects being probed with each polarization (more details will be given below).

Figure 4b shows a zoom of the nitrile stretching band after baseline correction. Surprisingly, and contrary to what was expected based on the known conformation of PAN, the intensity of the nitrile band was stronger with light polarized parallel to the NF bundle than with the incoming light polarized perpendicular to the bundle. The dichroic ratio for the nitrile band varied between 1.2 and 1.9 for all samples, either in transmission or in transflection, while values smaller than 1 were expected. What's more, the carbonyl stretching band at 1666 cm^{-1}, which is due to the presence of residual DMF in the fibers that is usually expected to be isotropic (see qualification below), is also more intense in the parallel-polarized spectra. This indicates that spectral distortions strongly affect the quantitative and even qualitative information in the spectra of PAN nanofibers.

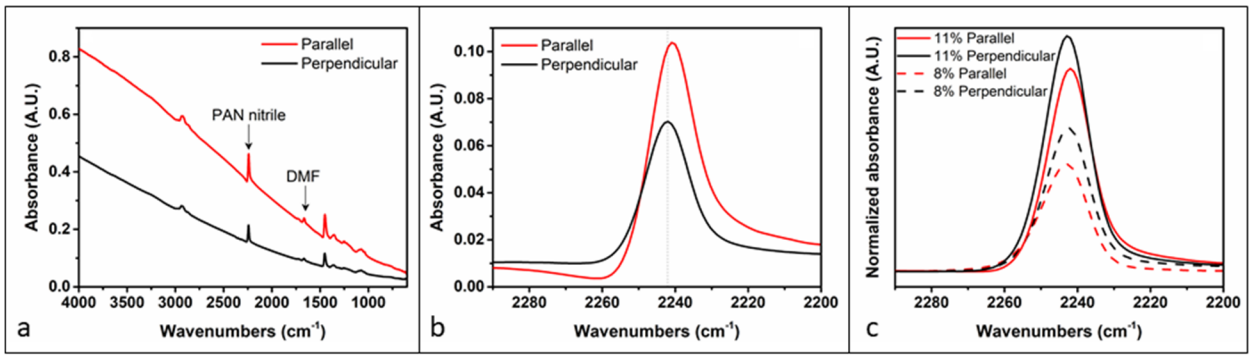

Figure 4: Polarized infrared spectra of bundles of PAN nanofibers. a) Original transmission spectra for the bundle prepared from the 8 % solution, showing large scattering; b) Baselined transmission spectra in the nitrile stretching band region showing anomalous dispersion and incorrect relative intensities; c) Transflection spectra of fibers prepared from 8 and 11 % solutions and normalized using a band from residual DMF.

It can also be seen that the nitrile band has a pronounced derivative shape that distorts the expected band shape and leads to an apparent shift of the maximum intensity by 2 cm^{-1} toward low wavenumbers with parallel polarization compared to perpendicular polarization. This

derivative-like shape is due to the reflection of the IR beam at the fiber surface in addition to absorption by the sample. The absorption depends only on the imaginary part of the complex refractive index of the sample (the absorption index, k) while the reflection depends on both k and the real part (the refractive index, n) of the complex refractive index. The "anomalous dispersion" of n (n is lower on the high-wavenumber side of the band and is higher on the low-wavenumber side) affects the fraction of reflected light and provokes the derivative-like bandshape. As a consequence, the apparent absorbance does not simply depend on the absorption coefficient of the fibers as one would expect. In fact, such dispersive bandshape can be seen in most IR spectra of fiber bundles reported in the literature.[15,48–51] The shift in band position between polarized spectra can also be observed in some cases when the spectra are shown at a scale allowing the observation.[52,53] This emphasizes that the spectral distortions reported here for PAN fibers are common when probing NF bundles by FTIR and can affect the quantified orientation values reported.

In an attempt to quantify the orientation in spite of the spectral distortions, the intensity of the nitrile band was normalized with respect to that of DMF. The transflection spectra were used because of a smaller effect of anomalous dispersion (see Fig. 4c). When doing this, orientation parameters $\langle P_2 \rangle$ of 0.14±0.03 and 0.33±0.04 were obtained for the samples with average diameters of approximately 750 and 500 nanometers, respectively. These results demonstrate that, properly analyzed, FTIR data can provide useful information on polymer chain orientation in NF bundles. However, it must be noted that the normalization procedure relied on the assumption that the residual solvent molecules are randomly oriented. In the past, Bashir *et al*[39,54] showed that some solvent molecules can form polymer/solvent complexes with PAN. As a

result, solvent molecules were found to have preferred orientation. If this is true for DMF, the normalization procedure will yield incorrect results, and the spectra cannot be corrected.

2.3. Differential Scanning Calorimetry Combined with Dielectric Relaxation Spectroscopy

A combined Differential Scanning Calorimetry **(**DSC)/Dielectric Relaxation Spectroscopy **(**DRS) examination is a powerful tool that can provide information on polymer structure. DSC examines changes in material heat capacity as a result of phase transformations, while DRS looks at changes in dielectric properties caused by the same transformations.

DSC is widely used to evaluate crystallinity of polymers and other aspects of polymer structure. It can also be used to gain information on polymer chain orientation by looking at the polymer glass transition. Changes in glass transition temperature and the shape of the step observed in DSC reflect differences in mobility of the macromolecular segments. In absence of changes in chemical structure, these differences are usually associated with changes in supramolecular structure such as degree of crystallinity and macromolecular alignment. Many studies[55–59] reported broadening of the glass transition when the amorphous phase mobility was hampered by crystalline growth or orientation.

A traditional two-phase model of semi-crystalline polymers is often insufficient to properly describe the polymer structure. The amorphous phase of the polymer can be subdivided into a rigid and mobile fractions (RAF and MAF, respectively). RAF, which results from incomplete decoupling between crystal and amorphous phases, is conceptually similar to an interphase in modern microstructural models of composites. In addition, a phase with intermediate level of order between crystal and an amorphous phase, called mesophase, can also appear.

DSC and Modulated Temperature DSC (MT-DSC) were used to investigate the microstructure of electrospun fibers in several polymer systems.[60–68] Existence of both mesophase, and RAF was observed.[62,69] The latter is likely due to the non-equilibrium nature of the electrospinning process, which produces microstructures with the amorphous phase sufficiently oriented to allow the creation of mesophase but prevents the formation of crystals.

The concept of cooperative rearranging region (CRR), defined as a subsystem which, upon sufficient thermal fluctuation, can rearrange into another configuration independently of its environment,[70] has also been linked to orientation of the amorphous phase. In this theory, the relaxation process related to the glass transition is cooperative in nature. A structural unit can move only if a certain number of neighboring structural units, the so-called CRR, are also moving. The CRR size or cooperativity length can be estimated using an appropriate model[71]. Several studies reported decrease of the cooperativity length in the amorphous phase of oriented drawn semi-crystalline samples[56–58,72] as well as the existence of anisotropy in the CRR size[73,74] with increase in macromolecular alignment.

To date, only a few studies investigated molecular dynamics in the amorphous phase of electrospun fibers. A straightforward correlation between results obtained for drawn materials and electrospun fibers might not be appropriate since the processes that generate macromolecular orientation are different. In contrast to what is often observed during drawing of polymer films, the electrospinning can possibly lead to macromolecular orientation while avoiding the effects related to the confinement of the amorphous phase by crystals.

Quantification of molecular mobility in highly oriented semi-crystalline systems is very challenging. Relaxation spectroscopy and more specifically DRS has been shown capable of investigating the evolution of local and/or delocalized molecular mobility during chain

orientation processes.[57] These processes have been associated with the appearance of oriented crystalline phases during strain induced crystallization and orientation of amorphous chains.[72] DRS monitors the relaxation processes associated with local or cooperative molecular mobility in amorphous fractions.[75] DRS is also sensitive to the presence of interfaces between mobile (mainly amorphous) and crystalline phases. In polymers these interphasic responses are classically attributed to RAF.

Few studies report the use of DRS for investigating the molecular mobility in electrospun nanofibers. The amorphous fraction in NFs is expected to be highly constrained by both the macromolecular orientation and the presence of mesophase[62] that can act as RAF. Estimating the mobility of the mobile amorphous fraction (MAF) is challenging due to the presence of RAF. This limitation is similar to studies of bulk polymers where the growth of constrained amorphous phase (RAF) is accompanied by a gradual disappearance of the MAF mobility.[76] In addition, due to the difficulty of investigating individual NFs, most of the studies are carried out on NF mats (see Fig. 5a). NF mats have a large amount of interfaces, leading to Maxwell-Wagner-Sillars (MWS) interfacial polarization.[77–79] This effect increases the complexity of studying molecular mobility relaxation processes (orientation polarization effects), especially at low frequencies. In order to suppress this effect, we removed the Teflon film in our experiments, which is otherwise usually positioned at the sample/sensor interface.

An example application of a combined DSC/DRS was performed on random PAN NF samples with different average NF diameters. The samples were electrospun from 8, 10, and 12 wt% of PAN in DMF under spinning conditions similar to ones used in XRD studies. The average diameter for the mats was 232 nm, 451 nm, and 785 nm, respectively. Modulated Temperature DSC (MT-DSC) experiments were performed on a DSC Q100 Thermal Analysis®

instrument. The in-phase component C` of the complex heat capacity was extracted. Dielectric relaxation spectra were measured with an Alpha Analyzer from Novocontrol in the frequency interval 10^{-1} – 2.10^{6} Hz. Additional information on the experimental procedures and data reduction for the DSC and DRS measurements can be found in the SI.

Different samples exhibited pronounced differences in the C` behavior in the glass transition domain localized around 80°C (see Fig. 5b). Analysis showed that the glass transition temperature increased from 78 to 87°C with the decrease of the average NF diameter. Furthermore, the glass transition was significantly broadened, until the heat capacity step became invisible and was transformed into a continuous variation of the heat capacity with temperature (sample with the smallest average diameter of 232 nm). This behavior is the signature of a hindered relaxation dynamics due to increased level of constraints in the amorphous phase for the sample with the smallest average NF diameter. Although such change in material behavior can also be caused by increase in polymer crystallinity, we know from previous examinations that the crystallinity of PAN nanofilaments decreases with the decrease in their diameter. Furthermore, the mat with the average fiber diameter of 232 nm exhibited the highest heat capacity. It is the signature of a higher content of amorphous phase relaxing at the glass transition. Thus, this result supports the assumption that reduction of the fiber diameter is accompanied by a decrease in polymer crystallinity. Consequently, the change in this case is caused by increased macromolecular alignment. It is important to note that constraint due to increase in surface to volume ratio for smaller NFs (confinement) should lead to the opposite effect of reduced T_g. This conclusion is supported by the examination of the real and imaginary part of the permittivity obtained from DRS measurements.

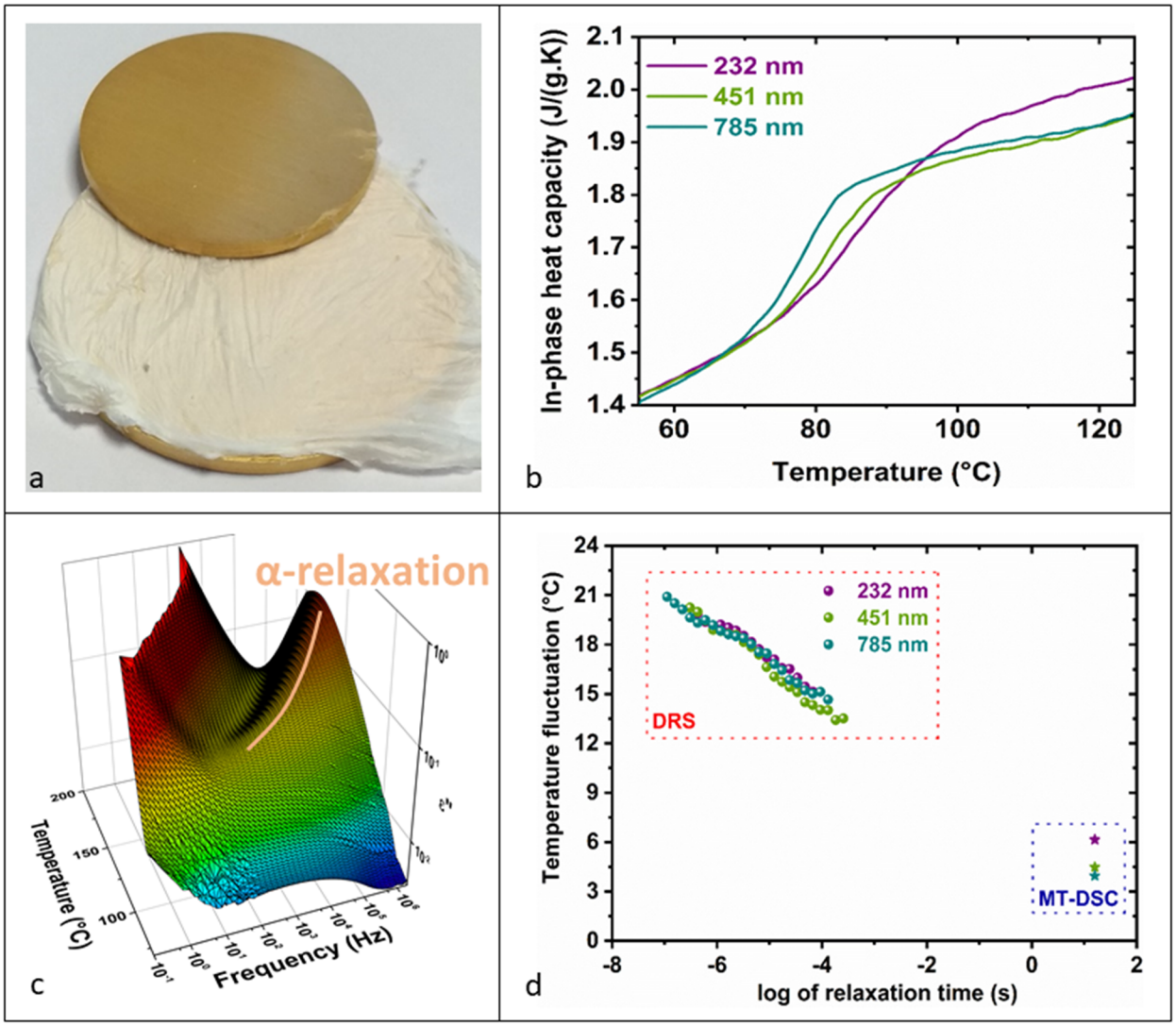

Figure 5: MT-DSC/DRS examination of PAN NF mats with different average nanofiber diameters. (a) Fiber mat of average fiber diameter 232 nm before the sample was fixed between DRS electrodes; (b) MT-DSC in-phase (C`) component of the complex heat capacity *versus* temperature; (c) Imaginary part of the complex permittivity *(ε*(ν))* as a function of frequency and temperature; (d) Temperature fluctuation associated with the alpha relaxation from MT-DSC and DRS measurements.

DRS classically provides the signature of the α-relaxation (dielectric manifestation of the glass transition) at temperatures above the calorimetric glass transition temperature. In Figure 5c, it appears as a peak on the imaginary part, which position on the temperature axis is dependent on the applied frequency. Coupling DRS with calorimetry techniques, such as MT-DSC or fast scanning calorimetry (FSC),[80] can extend the range of investigation for the temperature

dependence of the relaxation time. Temperature fluctuation δT associated with the α-relaxation is a signature of the distribution of the relaxation times in the amorphous phase. It increases with temperature, but can also vary due to structural causes, reflecting structural differences between samples when examined at comparable temperatures. As can be seen in Figure 5d, the initial difference in temperature fluctuation observed at the glass transition from MT-DSC disappears at high temperature recorded in DRS. Since the melting temperature of PAN is about 300°C, this change could not be caused by the disappearance of the crystalline phase. However, it might be attributed to the constraint slackening in the initially oriented structure (entropic relaxation of polymer chains), when crossing the glass transition temperature.

Therefore, this set of results indicates that electrospinning induces orientation of macromolecules, which becomes more pronounced in samples with smaller NF diameters. This orientation significantly impacts structural dynamics around the glass transition. At higher temperatures, the orientation gradually vanishes, as macromolecules become more flexible and stress relaxation occurs. Overall, the example shows that changes in relaxation behavior around T_g can provide information on polymer chain alignment that complements results obtained by other methods. Relaxation mechanisms related to chain mobility are inherently mechanical in nature and can therefore provide valuable insight into mechanisms of NF mechanical behavior and toughness. Analysis of T_g is especially useful for polymers in which the melting temperature is higher than the onset of thermal degradation, as is the case with PAN.

2.4. Nuclear Magnetic Resonance (NMR) Spectroscopy

Nuclear Magnetic Resonance (NMR) Spectroscopy is a spectroscopic technique that can provide detailed information on molecular structure, conformation, and dynamics (relaxation). In this technique, the sample is placed in a high magnetic field and is excited by a radio frequency

pulse from the ground state to an excited state. The frequency required to flip the nucleus from the ground to the excited state is characteristic of the nucleus observed, and is sensitive to the local electronic environment (shielding vs. deshielding). The most common NMR techniques involve nuclei with spin $I = ½$, such as ^{1}H and ^{13}C. Nuclei with spin $I = (2n+1)/2$, such as ^{17}O and ^{27}Al can also be examined. Nuclei with spin $I = 0$ (^{12}C, ^{18}O) are not NMR-active.

Solid state NMR (SSNMR) is less developed than solution NMR, and can suffer from sensitivity and technological problems. However, it emerged as an important technique for studying polymer structure. The technique has several advantages, such as the ability to study insoluble materials and conformations not attainable in solution, over the solution based NMR.[81]

In general, SSNMR can be used to study important aspects of solid state polymers such as internuclear distance, atomic coordinates, backbone torsion angle, crystallinity and the mix of different crystal structures, as well as orientation in both the crystal and the amorphous phases.[81,82] NMR interactions such as dipolar (between nuclei with spin $I \neq 0$), quadrupolar (nuclei with spin $I > ½$), scalar coupling (indirect interaction between two spins), and chemical shielding are inherently anisotropic. This anisotropy has been used to study orientation in drawn films and fibers.[81,82] Multiple approaches exist. The most popular uses chemical shift anisotropy (CSA) tensor of rare nuclei such as ^{13}C[83–85] and ^{15}N,[86–88]although naturally abundant nuclei such as ^{19}F were also used.[89]

The chemical shift, observed as the different peaks on the NMR spectrum due to chemical shielding, is a second order tensor. The principal tensor components can generally be obtained from a static examination of an isotropic sample (such as powder sample).[82,90] Some techniques also require an “isotropic” value of the chemical shift to analyze the difference between this parameter and the observed chemical shift values at different fiber/magnetic field

orientations. The isotropic chemical shift can be obtained either from averaging the principal components of the tensor, or by carrying out Magic Angle Spinning, MAS, (rapidly spinning the sample at the angle of 54.74° relative to the applied field) experiments on the powder sample. Once the principal components of the tensor are known, several approaches to obtaining orientation information exist.

The comprehensive approach analyzes and fits line shapes of the chemical shift as a function of the angle between the magnetic field and the fiber/draw axis to obtain multiple order orientation parameters.[89,91,92] Such an investigation is time consuming and complex. Alternatively, in a simplified approach, measurements can be done either in one (parallel)[86,88] or two (parallel and perpendicular)[87] configurations. To obtain orientation information, Gaussian distribution of the orientation function is generally assumed. Fitting the "parallel" spectrum produces a set of possible Euler angles for the rotation of the chemical shift tensor from the principal components axis system to the fiber axis system. Additional fitting of the "perpendicular" spectrum and error minimization procedures are needed to obtain orientation parameters as expressed by the width at half maximum of the orientation distribution. This orientation parameter does not relate directly to structural features, but to an average angle between the main axis of the principal component tensor and the fiber systems. However, if molecular conformation is known, this orientation parameter can be converted into distribution of bond angles in the fiber.[87] Although these approaches are less complex than the comprehensive one, they still require multiple spectra acquisition, examination of powder samples, and relatively complex fitting procedures.

A further simplification is possible. It has been shown that the chemical shift in the configuration where the magnetic field is parallel to the major sample axis linearly correlates to

orientation parameters obtained by other technique.[83] Consequently, it can be used as an indicator of orientation for comparative studies without obtaining the chemical shift tensor components.

The different orientation studies were so far demonstrated for drawn films,[89,91] conventional,[88,93] and biological[94,95] fibers. SSNMR has also been used to determine conformational changes in electrospun silk fibers.[96] In principle the above described approaches can be extended to the study of orientation in NFs. However, to our knowledge, such studies have not yet been conducted or published.

SSNMR is generally less sensitive compared to the solution technique and can suffer from low signal to noise ratio.[81] In solution, anisotropic NMR interactions are averaged over the time domain due to rapid random tumbling for small molecules and rapid segmental motion for high molecular weight polymers. The nuclear dipole-dipole interactions average to zero, while chemical shift anisotropy averages to a non-zero value. This averaging produces sharp, well resolved peaks. On the other hand, in solids, molecular motion is restricted, and the anisotropic interactions as well as the presence of multiple polymer conformations can cause severe line broadening.[81] This problem can become more acute for samples with low crystallinity and amorphous structures as well as in cases where different chemical shifts are not sufficiently spectrally separated.[81]

Several approaches exist to partially remove the line broadening in SSNMR. Magic Angle Spinning (MAS) produces a similar effect to molecular motion in solution. MAS speed requirement in order to suppress line broadening changes depending on the interaction. However, it is generally on the order of several kHz and increases linearly with the increase in the magnitude of the magnetic field used in the NMR system.[81] This can lead to technological

problems of spinning the sample at the required speed. In addition, quadrupolar interaction is only partially averaged by MAS, and leaves line broadening in cases where this interaction exists.

Multiple pulse sequences are used for dipolar decoupling (both for homo-[97] and heteronuclear[98] interactions). Cross polarization (technique where polarization from abundant spins such as ^{1}H or ^{19}F is transferred to dilute spins such as ^{13}C or ^{15}N) is used to enhance signal to noise ratio.[81] In addition, the use of naturally rare nuclei such as ^{13}C or ^{15}N removes line broadening due to homonuclear dipolar coupling since the distances between the adjacent studied nuclei are very large. Specific site or general labeling, using rare isotopes, can also be used to improve sensitivity and signal to noise ratio. More recently, cryogenic probes have gained use in NMR. Such probes reduce thermal noise and improve signal to noise ratio, allowing for shorter (up to four times) acquisition times.[99]

An example of SSNMR application to PAN powder can be found in SI. In solution, the chemical shift of the carbon in the nitrile group appears as a sharp singlet.[100] In contrast, the SSNMR spectrum in our experiment is very broad. The observed broadening is likely the result of convolution of the signals from the crystal and the amorphous phases in the semi-crystalline polymer. A series of experiments on samples with different polymer crystallinities with and without MAS could help identifying different signals. In particular, examination of a fully amorphous and a highly crystalline polymer would be of most help.

Labelling the samples (adding to the natural abundance of the nuclei)[96,101,102] can significantly improve sensitivity of this technique. However, possible effects of labeling on the electrospinning process and resulting nanofibers need to be carefully examined.

2.5. Limitations of Techniques Requiring Bundles of Nanofibers

The techniques described in this section require relatively large material volume to produce good signal to noise ratios. As a result, these techniques rely on examination of bundles to extract average orientation information for electrospun NFs. Two problems complicate the analysis, in addition to the experimental artifacts described in the previous sections.

First, in case of XRD, FTIR, and SSNMR, aligned NF bundles are needed. Alignment of the NFs within the bundles is not perfect (see examples of NF orientation distribution within the bundles in Fig. 3c,f). The above techniques cannot distinguish between NF orientation and the orientation of polymer chains and crystals within the NFs. As a result, misorientation of NFs within the bundles introduces significant measurement errors, leading to underestimation of the orientation of the structural features. The situation is further exacerbated when the degree of NF alignment in the bundles changes between samples, preventing even comparative studies. Generally, misalignment of NFs in the bundles increases with the decrease in NF diameter. Consequently, some of the expected improvement in the degree of preferred orientation in fine NFs can be masked by increased NF misalignment. The problem in case of SSNMR is even more severe as larger amounts of material are needed.

Second, within the bundle, NF diameter is not monodisperse. The level of polydispersity depends on sample fabrication parameters and will generally vary with the average NF diameter in the bundle (see, for example, Fig. 3b,e). Larger NFs within each bundle occupy larger volume. Consequently, most of the signal comes from thicker nanofilaments (see Fig. 6 for an example of the effect of NF diameter distribution on proportion of the volume taken by larger NFs).

While a degree of polydispersity is inherent in samples of electrospun fibers throughout the fiber diameter range, it is especially difficult to obtain bundles with ultrafine average diameters without significant artifacts. Producing NF bundles with smaller average diameters

usually requires reduction of solution viscosity. Electrospinning is a complex multi-physics process involving delicate balance between viscosity, surface tension of the solution, and the applied electric field. At low viscosities, the surface tension dominates and can lead to capillary breakup of the electrospinning jet or to so called beaded NFs.[103] Polymer chain alignment (and likely crystallinity) in beads is different from that in the uniform parts of the NFs.[104] Presence of beads can constitute a large volume fraction of the sample. The techniques described in this chapter provide averaged information for the examined volume. As a result, it is not possible to obtain correct information on crystallinity and degree of macromolecular alignment in NFs in the presence of non-uniformities and other artifacts related to sample preparation.

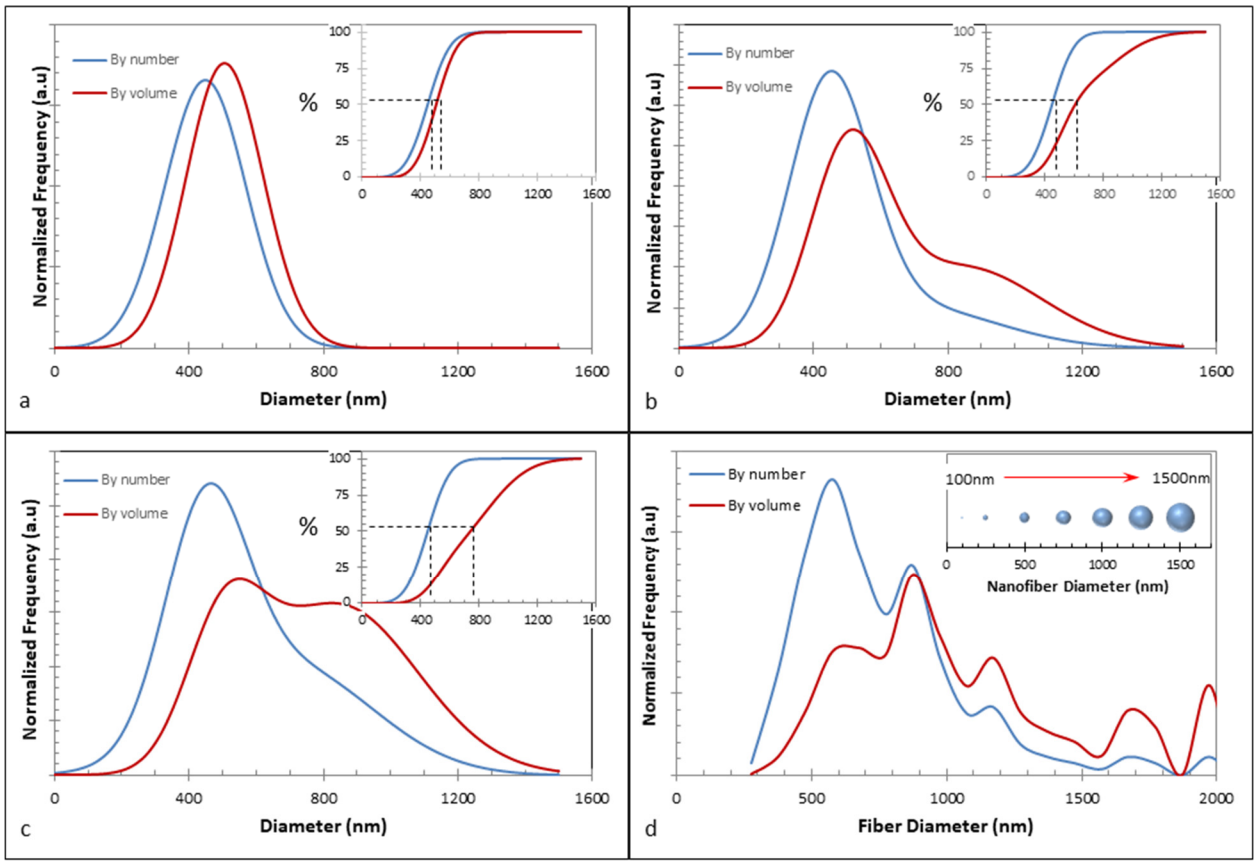

Figure 6: Effect of NF diameter polydispersity on the relative volume associated with each diameter within the distribution. Synthetic diameter distributions – (a) Uni-modal normal distribution with average diameter of 450 nm and a standard deviation of 120 nm; (b)-(c) bi-modal normal distribution with average diameters of 450 and 700 nm and a standard deviations

of 120 and 250 nm at different mode mixes. Insets in (a)-(c) show changes in cumulative distributions when changing from distribution by number to a distribution by volume. Dashed lines show the shift in the median diameter between the number and volume distributions. (d) A real diameter distribution measure for a NF mat. The inset shows the relative cross-sectional area for NFs from a 100 nm and up to a 1500 nm in diameter.

Because of these issues, techniques which rely on nanofiber bundles or mats for the examination of orientation face significant challenges when dealing with the NFs in the ultrafine diameter range.

3. Methods of Analysis Applicable to Individual NFs

In general, evaluation of individual NFs is preferred for structural studies. Such an evaluation would eliminate the problems associated with NF bundles described above. In addition, use of such techniques in conjunction with the newly developed mechanical testing protocols,[12] would allow structure-properties relations to be examined on the same individual NF. Direct correlation of structure and properties on single nanofiber specimens would significantly reduce scatter, provide more precise understanding of the mechanisms of mechanical behavior and result in quicker and more robust property optimization through structural control.

3.1. Selected Area Electron Diffraction

Selected Area Electron Diffraction (SAED) is a crystallographic technique that is typically used inside a Transmission Electron Microscope (TEM). The principles governing electron diffraction are similar to those for X-ray diffraction, with some notable differences. Electrons are charged particles, and thus their interaction with the atoms in the matter is much stronger. In addition, wavelengths corresponding to electrons inside a TEM are much shorter than for X-ray diffraction, resulting in significantly smaller diffraction angles.

Because of the short wavelength of electrons, very small spot sizes in SAED can be achieved by focusing the electron beam. Strong interaction between electrons and material produces a sufficiently strong signal to noise ratio. As a result, SAED is naturally suitable for examination of small individual NFs. The procedure for evaluating the degree of preferred orientation in SAED is similar to XRD. SAED was successfully used in the past to evaluate crystal orientation in carbon nanofibers.[4,105] It was also used on several polymer systems with relatively high crystallinity.[16,18,43,106,107]

Application of SAED for polymers with low and variable crystallinity is more problematic. An example of SAED examination of individual PAN NF is shown in Figure 7. SAED pattern from single as-spun NF (see Fig. 7a for a TEM image of the fiber) showed extremely weak and diffuse ring that did not allow for orientation examination (see Fig. 7b). This result is qualitatively similar to the results obtained for a NF bundle by XRD (see Fig. 3). This is because, similarly to XRD, SAED can only provide information about crystal orientation in the fibers. For this reason, examination of low-crystalline or amorphous structures becomes difficult or impossible.

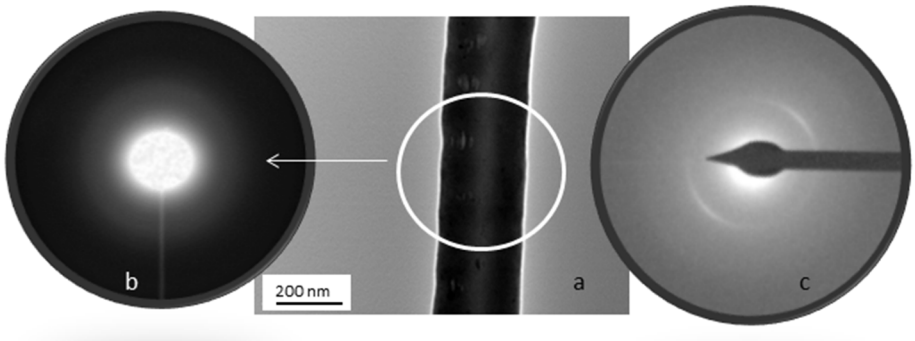

Figure 7: SAED from an individual PAN NF. (a) The area from which the electron diffraction was taken; (b) SAED of as-spun NF, showing an extremely diffuse signal characteristic of a largely amorphous structure; (c) SAED from a NF annealed at 180°C, showing signs of crystallinity and preferred crystal orientation. The change in the crystal structure is consistent with the results for annealing the NFs above the glass transition temperature of PAN, shown in previous work.[12]

Unlike the case of XRD, annealing at 130°C did not result in significant improvement in the observed SAED. Only after annealing the NFs at 180°C, more pronounced crystalline arcs with preferred crystal orientation became visible (see Fig. 7c). However, these arcs were not as pronounced as in XRD. As a result, examination of orientation was still difficult. One possible reason for such a weak diffraction is partial damage to the NF structure from interaction with the electron beam.

The energy in the electron beam is focused on a much smaller area than in XRD. The wavelength of electrons is approximately two orders of magnitude shorter than that of X-rays. This means that the energy of individual electrons is much higher than the energy of X-ray photons. Charged electrons produce a stronger interaction with the material. As a result, polymers and other organic materials are significantly more susceptible to radiation damage in SAED than in XRD. The level of damage to the NF structure is difficult to evaluate. Therefore, SAED data interpretation for polymers with low crystallinity is difficult. Changes in polymer crystallinity due to annealing and/or radiation damage in SAED can also change the original orientation and therefore lead to errors.

3.2. Polarized Optical Light Microscopy

3.2.1. Measurements of Optical Anisotropy

Polarized optical microscopy measures birefringence, the difference in material refractive index depending on light polarization. Non-cubic crystal structures and oriented polymers are often birefringent. As a consequence, results from polarized optical microscopy experiments can often be used as an indicator of the degree of macromolecular orientation.[108] If the intrinsic birefringence (for perfectly aligned system) of the polymer is known, it is possible to convert the

measured birefringence value into the order parameter $\langle P_2 \rangle$ (see a typical schematic of the experimental setup in Figure 8a and a detailed explanation in SI).

Figure 8b-c shows the change in light intensity in drawn and electrospun DNA fibers of 4 μm and 400 nm in diameter, respectively, as a function of the angle between the polarizer and the fiber. The insets in the panels show the variation in the corresponding light intensity. Theoretically, retardation (the difference in the optical path) can be obtained either from the fit or from measurements at any specific angle (generally $\theta = 45°$ is preferred in this case because it produces maximum intensity). If sample thickness can be accurately measured, birefringence can then be calculated. Different orders of birefringence are possible (due to the periodicity of the intensity function). The different orders can be distinguished through the use of waveplates or by measuring birefringence at several wavelengths.

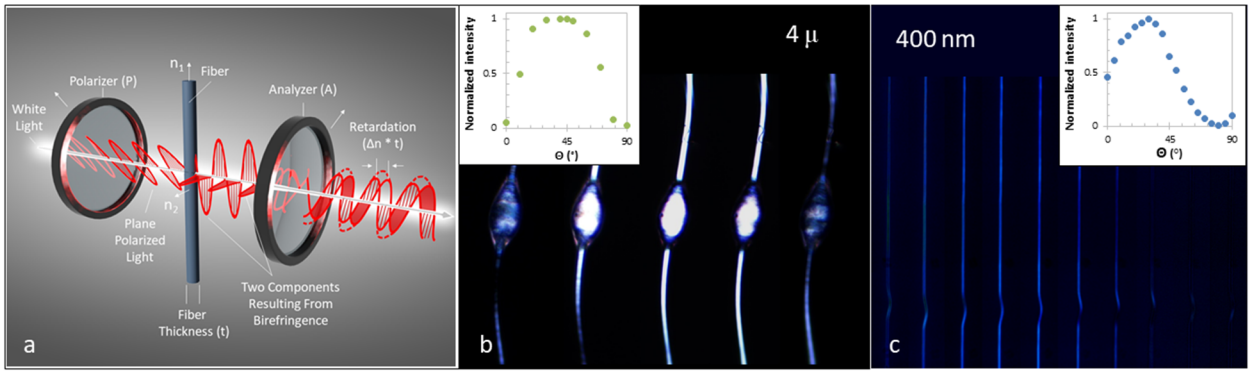

Figure 8: Polarized optical microscopy experiment. (a) Schematic of a typical experimental setup; (b) Mechanically drawn from solution DNA fiber, 4 μm in diameter, observed at different angles between the fiber and the polarizer; (c) Electrospun DNA fiber, 400 nm in diameter, observed at different angles between the fiber and the polarizer. The insets in panels (b) and (c) show the variation in the measured intensity as a function of the angle between the fiber and the polarizer. In the case of mechanically drawn fiber (b), the intensity was measured in the fiber region away from the "bulge" visible in optical photographs. The electrospun nanofiber was uniform in diameter. The results indicate presence of significant preferred orientation in the fibers.

Another approach is *Polarization-Modulation (PM) Microscopy*. This technique applies polarization modulation spectroscopic approach in a microscopy setup to measure differential

absorption due to electronic transitions of the sample (its dichroism) as a function of the incoming light polarization. Existing commercial equipment allows PM spectroscopic measurements to be carried out using ultraviolet, visible, and infrared light. The spatial resolution of PM microscopy can also be improved beyond the diffraction limit, using near-field microscopy (see discussion in Section 7.2). In the *polarization-modulation* setup, the incoming light is modulated (switched) between two orthogonal linearly polarized states at high frequency. The changing absorption at different polarizations can be related to the molecular features of absorbing polymer and the differential absorption can be used as an indicator of molecular orientation. The technique allows for detection of small differences in the transmitted intensity.[109] As such, it is theoretically advantageous for samples smaller than the spot size (such as NFs), where the absorption is expected to be small.

3.2.2. Problems with Data Interpretation for Subwavelength NFs

The techniques described above have several advantages. When visible light is used (similarly to Raman spectroscopy discussed later), the spot size is significantly smaller than in FTIR, allowing for a better signal to noise ratio when examining individual NFs. In principle, ultraviolet (UV) light can be used to further reduce the spot size. However, care needs to be taken since UV light can potentially damage the polymer structure (UV light is especially prone to breaking C=C double bonds). On the other hand, when visible light is used, damage to materials can generally be avoided. In addition, simple, inexpensive polarized light microscopic instrumentation is widely available.

Despite these advantages, the techniques face several challenges. As was mentioned above, in case of birefringence measurements, there is a need to account for variation of sample thickness over the projected sample width (*i.e.* over diameter in the lateral direction of the fiber).

The second problem in comparative studies is the changing crystallinity. The crystalline and the amorphous phases have different intrinsic birefringence and the relative orientation of the phases can also differ. As a result, the measured birefringence is going to produce a composite signal. Disentangling the different components of birefringence for comparison of orientation between NFs with different diameters would require preparation of multiple samples with different degrees of crystallinity and orientation. However, independent variation of crystallinity and orientation is very difficult, especially in samples with low crystallinity/high macromolecular alignment, such as ultrafine NFs.

In case of PM optical microscopy, the absorption of the crystal and the amorphous phases can be different as well, leading to similar problem with data interpretation if they are not well separated spectroscopically.

Finally, since both techniques measure the intensity of the transmitted light, the amount of scattered/reflected light will play a role. The amount of reflected/scattered light will depend on the degree of crystallinity and size of the crystal, and on the curvature of the NF surface (see discussion in Section 4.3.2). Smaller NFs will scatter more light, leading to problems in comparative studies. In addition, the light polarized parallel and perpendicular to the nanofiber will be scattered differently (see additional discussion in Section 4.3.2). This different scattering is potentially the reason for the shift in the maximum intensity in the inset in Figure 8c from the 45° angle. The severity of this problem will again be diameter (curvature) dependent.

Furthermore, since light has approximately Gaussian distribution of intensity across the spot, the location of the spot center relative to the fiber axis will also play a significant role in the amount of reflected light, and hence measured transmitted intensity. This problem will become more acute as the fiber size becomes comparable to the spot size.

As a consequence, even though birefringence is shown to be detectable in individual NFs (see Fig. 8), the problems described above can generally lead to quantitative or even qualitative errors. More studies are needed to establish applicability of the above techniques for orientation analysis of NFs with subwavelength diameters.

4. Evaluation of Polymer Chain Orientation Using Polarized Raman Microscopy

Raman spectroscopy is a technique based on inelastic scattering of monochromatic light by matter. Since the scattering is inelastic, the scattered light has a different wavelength from the incoming light. The difference between the two wavelengths is often referred to as the Raman shift. The observed peaks in the Raman spectrum correspond, similarly to FTIR, to different vibrational modes within the material. However, the two techniques are more sensitive to different types of vibrations. FTIR is sensitive to the changes in permanent dipoles associated with the vibration. On the other hand, Raman signal relies on variation of the polarizability (change in the dipole moment) associated with the vibration. Bonds with weaker permanent dipoles generally have higher polarizability and vice versa. As a result, bands can significantly change in intensity or appear/disappear, depending on their symmetry, when comparing the two techniques. Importantly, Raman spectroscopy is often significantly more sensitive to the polymer backbone vibrations, since these vibrations generally tend to have weak dipole moments, and therefore high polarizability.[110] Raman spectroscopy has been used extensively to obtain information on internal stresses,[111] chemical structure and composition of polymers and blends, as well as on physical changes in polymer conformation and crystallinity,[110] including for sub-micron sized structures.[112]

Raman microscopy is a powerful technique that can generally be used to interrogate individual nanofibers.[31] Advances in laser technology, optics, and detectors in modern confocal

Raman microscopes allow for small spot sizes for higher signal to noise ratio (with spot sizes smaller than 1 micrometer currently possible), excellent spatial and spectral resolutions, as well as improved signal to noise ratios. Both spot size and focal depth are proportional to the laser wavelength. Smallest possible lateral spot size is desirable for best spatial resolution and signal to noise ratio when probing a nanosized sample. On the other hand, small focal depth can sometimes be beneficial (for example for depth profiling or in examining thin films) or detrimental because of the reduction in the signal intensity due to small confocal volume. A wide array of quality lasers from the near-infrared to the ultraviolet is available. This allows for a choice of laser based on the required spatial resolution, sensitivity of the detector and the material to specific wavelengths, and other considerations, such as the need to separate the Raman signal from fluorescence. Confocal Raman microscopy also allows obtaining the signal from the same sample area that is visually observed. This capability is essential when focusing on fibers with submicron and nanometer diameters. As a result, investigations of individual NFs with diameters as small as 100 nanometers and even below, are theoretically possible.

Polarized Raman Microscopy is a method that allows for examination of orientation in the material. Contrary to SAED, polarized Raman analysis can generally provide information on chain orientation in either amorphous or crystalline phases. Consequently, evaluation of the degree of macromolecular orientation in individual NFs with low crystallinity is possible.

4.1. Complete Raman Analysis of Polymer Chain Orientation

Both Raman and FTIR are vibrational spectroscopic methods. However, FTIR is a one-photon absorption technique. Raman spectroscopy, on the other hand, is a two-photon scattering method. This results in several key differences in the analysis compared to FTIR. The intensity of Raman scattered light is proportional to the square of the magnitude of the induced

polarization vector. Polarization vector, in turn, is proportional to the polarizability. The Raman tensor is the spatial derivative of the polarizability with respect to local molecular coordinates.

Examples of the use of polarized Raman microscopy to determine polymer chain orientation were provided by Bower,[113,114] and can also be found in Jasse and Koenig.[38] The complete experimental and data reduction procedures are complex. They require twelve Raman spectra measured in three different laser/sample/detector geometries to fully resolve the orientation functions.[110,115]

Common confocal Raman microscopy systems are limited to backscattering geometry (*i.e.* the detector collects the signal from the sample scattered back towards the objective, rather than at 90° to the direction of the incident light propagation. A schematic of a typical optical path in polarized Raman microscopy can be found in Figure S1 in SI). In addition, samples like thin films and fibers cannot usually be placed with the axis of their large dimension(s) along the light propagation direction.[19] As a result, only a set of intensities under four polarization combinations can normally be measured. With this limitation, additional approximations are needed. It is commonly assumed that the Raman tensor for a specific vibration has cylindrical symmetry. This assumption is not always valid, as certain vibrations were shown in the past to have a non-cylindrical Raman tensor.[116] However, violation of this assumption does not usually have large effect on orientation measurements in samples with uniaxial orientation. In addition, the Raman tensor for a particular vibration is usually assumed to be independent from the degree of polymer chain alignment and polymer crystallinity. This assumption was also shown not to be true.[117] In our experience, the effect of changes in the Raman tensor due to changes in crystallinity is more significant than due to non-cylindrical symmetry.[117] With these approximations the second and the fourth order Herman orientation factors, $\langle P_2 \rangle$ and $\langle P_4 \rangle$, can be calculated (see SI).[118]

In order to obtain the orientation factors, four Raman spectra need to be collected from the same location on the fiber. The four spectra consist of two sets with the incoming light and the analyzer polarized in the same direction parallel and perpendicular to the fiber, I_{VV} and I_{HH} respectively, and two sets of cross-polarizations, I_{VH} and I_{HV}. The ratios between the intensities (depolarization ratios) under cross and parallel polarizations can then be used to calculate the orientation factors. Here and in the rest of the paper intensity refers to integrated intensity (the area under the spectral peak). Measurements of these ratios for isotropic samples are also needed to fully solve the equations.[118] The latter requirement can create significant experimental problems, as adequate isotropic samples are not always available or possible. This problem can be avoided by additional assumption of a normal orientation distribution function.[117] A more detailed description of both the experimental and the mathematical treatment can be found in reference [19]. This method will be referred in the rest of this paper as "comprehensive evaluation/analysis method".

Obtaining multiple spectra for ultrafine NFs can suffer from a variety of problems and instrumental artifacts. These are mostly the consequence of slight drifts of the laser spot relative to the NF (see discussion below; such drift can occur either due to instrumental issues or due to NF movement).[19,104] The comprehensive method relies on ratios of absolute intensities under different polarizations. Even small shifts can produce significant changes in these intensities. These errors will compound and can prevent reliable data reduction to obtain the depolarization ratios. The possibility of errors will also increase with the increase in spectrum acquisition time (for small samples longer acquisition times are needed to produce better signal to noise ratios).

In general, a simplified approach, utilizing reduced number of spectra would be of great value, both to reduce experimental errors and for fast sample evaluation and comparison. This is especially true for ultrafine NF specimens.

4.2. Orientation Evaluation Using Intensity Ratio for a Single Band under Two Polarizations: An Unexpected Artifact

A quantitative indicator of polymer chain orientation can be obtained by examining only VV and HH polarization combinations for a single band. For properly acquired spectra, the I_{VV}/I_{HH} intensity ratio will indicate the degree of orientation of Raman tensor for a certain vibration along the V axis. This indicator does not provide an absolute value of orientation factors, but with the knowledge of molecular conformation, it can be used for comparative studies. Frisk *et al*[115] compared the orientation factors extracted from the comprehensive evaluation to sample birefringence and the I_{VV}/I_{HH} ratio in conventional poly(propylene terephthalate) fibers. They found good correlation between $\langle P_2 \rangle$, birefringence, and 1-I_{VV}/I_{HH}. Therefore, the above simplified approach can theoretically be used to examine size effects in individual NFs. Qualitative comparison of the I_{VV} and I_{HH} spectra was performed on electrospun poly(ethylene oxide) NF bundles.[32] However, only spectra for a single aligned NF bundle were shown, and the I_{VV}/I_{HH} ratio was not calculated.

To evaluate applicability of this simplified technique to PAN NFs, Raman spectra for a drop-cast film (with no preferred orientation) and an electrospun PAN NF under two different polarizations were collected and compared (see Fig. 9a,b). The polarization of the laser and the analyzer were parallel and the orientation of this polarization was changed relative to the film and fiber (see insets in Fig. 9a,b).

All spectra exhibited very strong, sharp band *circa* 2242 cm^{-1}, corresponding to the nitrile stretching mode in PAN, and several strong overlapping bands in the wavenumber range 2800-3100 cm^{-1}, corresponding to different CH vibrations. As was discussed in the context of FTIR, both regions can be used for orientation studies in PAN. However, the nitrile band is generally preferred because it is spectrally isolated from other bands. In the case of the drop cast film (Fig. 9a), as expected, the spectra showed no change for different polarizations. In case of the fiber, the spectra were markedly different for different polarizations (see Fig. 9b). As per description above, this difference should indicate preferred orientation of the polymer chains within the NF.

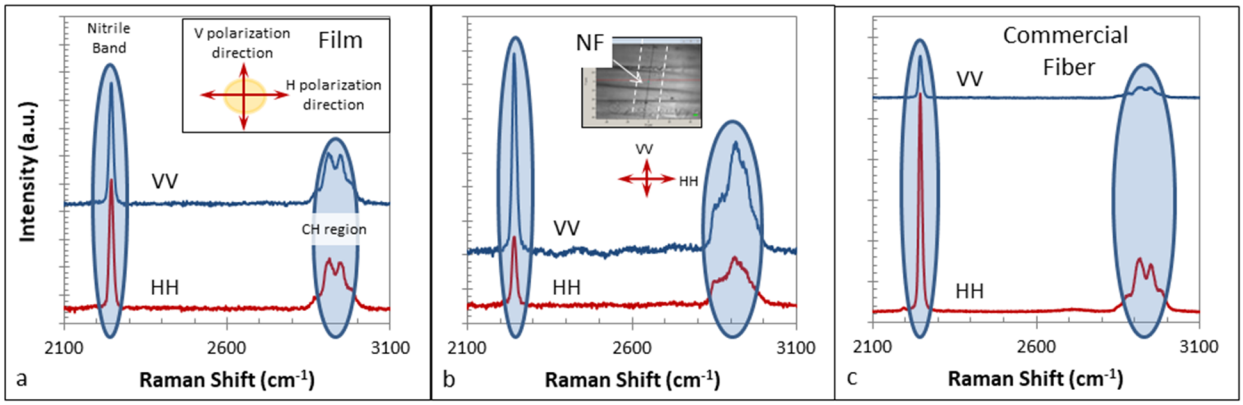

Figure 9: Simplified examination of polymer chain orientation using the same band at two polarizations in Raman (reprinted with permission from ref [119]). In polarized Raman measurements of polymer chain orientation large difference in I_{VV} and I_{HH} intensities indicates large preferred orientation of nitrile groups. (a) Raman spectrum of a drop-cast PAN film in two polarization orientations, showing no preferred orientation. Inset shows schematic of how polarization relates to the film (the measurements are done for both the polarizer and the analyzer in the same orientation); (b) Raman spectrum of an individual PAN NF (~300 nm) in two polarization orientations in the range showing the nitrile band and the CH region, indicating significant apparent orientation. The inset shows an optical microscope image of the NF and the respective polarization orientations. The relationship between the respective intensities is contrary to what is expected based on molecular models of PAN; (c) Raman spectrum of a commercial PAN microfiber (~ 30 μm) in two polarization orientations (orientation is the same as in (b)). The relationship between the respective intensities is as expected based on molecular models of PAN. Adapted from ref [119].

However, unexpectedly (and similarly to the bundle examination by FTIR), the I_{VV} intensity of the nitrile stretching mode was stronger than the I_{HH} ($I_{VV}/I_{HH}>1$). Several NFs with

diameters below ~500 nanometers were tested, producing qualitatively similar results. In fact, I_{VV}/I_{HH} ratio increased with the decrease in NF diameter. These results were independently replicated in the laboratory of one of the co-authors of this study (CP), indicating a systematic nature to the artifact. This ratio of intensities of the band under different polarizations is reversed relative to what is expected based on the molecular conformation of PAN. As described above, the nitrile groups are arranged almost perpendicular to the main chain. Given this large angle between the nitrile group and the main chain, I_{HH} should be stronger than I_{VV} when preferred axial orientation of the main chain is present. A similar relationship between $I_{\perp}$ and $I_{\parallel}$ absorptions was observed in the past using FTIR dichroic ratio both in drawn films[39,45,47] and electrospun PAN NF bundles.[15] Raman examination of commercial conventional PAN microfiber, Dralon X250 (approximately 30 μm in diameter), also exhibited this expected relation between the intensities (see Fig. 9c). Both past FTIR examinations of bundles and our Raman examination of a commercial PAN fiber dealt with diameters significantly larger than the wavelength of the light source. On the other hand, spectra in the Figure 9b are for an individual NFs smaller than ~300 nanometers in diameter (less than half the wavelength of the laser). The change in the I_{HH} to I_{VV} relationship in this case indicates a potential size-related artifact related to small NF diameters.

4.3. Sources of Artifacts in Polarized Raman Analysis of Sub-Wavelength-Diameter Nanofibers

Both the comprehensive analysis and the simplified approach described above require acquisition of multiple spectra under different polarization combinations. The use of multiple polarization combinations can lead to several potential artifacts. Some of these trace back to instrumental issues. Others are inherent in NF geometry (size and curvature) and birefringence.

The description in this section is not meant to be an exhaustive list of potential artifacts, and additional studies are needed to identify the potential sources of errors.

4.3.1. Instrumental sources

One of the well-known instrumental sources of artifacts in polarized Raman studies is the polarization-dependent response of the system. The response of the grating, which is used in Raman microscopes to achieve spectral separation of the signal, is usually dependent on the polarization of the incoming light. The difference in the light intensity after the grating can be sometimes as large as a factor of three depending on the incident light polarization. This poses a significant challenge for polarized Raman studies.

In order to avoid this issue, the linear polarization of the light after the analyzer needs to be converted into a circular polarization or depolarized (through the use of a quarter wave-plate or a scrambler). In circular polarization, two perpendicular polarizations of light with equal amplitude, and a 90° phase shift are combined. This results in constant light intensity for all polarizations. As a consequence, conversion of linear polarization into a circular one avoids the problem of polarization dependent response of the grating.

Linear light polarization is commonly converted into a circular one by inserting a quarter-wave-plate in the optical path (see Figure S2 and section 8 of SI). The wave-plate direction needs to be at 45° relative to the direction of the incoming polarization. However, most Raman systems use a quarter-wave-plates intended to be used with a range of wavelengths. Such wave-plates are imperfect. As a result, instead of a circular polarization, they produce an elliptical one. An elliptical polarization is created when the amplitudes of the two perpendicularly polarized light-waves are unequal, or if the phase shift is not 90° (this can also happen if the quarter-wave-plate is not perfectly aligned). As a result, light intensity in elliptical polarization is not equal for all

polarizations. The ratio of these intensities will change depending on the direction of the incident linear polarization. Consequently, even with a quarter-wave-plate, residual problems with polarization dependence of the grating response remain.

This problem is also accentuated by imperfections in the analyzers that are generally used. A perfect analyzer fully suppresses polarization perpendicular to the axis of the analyzer. Crystal analyzers can approach perfect ones with large ratios of suppression. On the other hand, common film analyzers allow a certain amount of perpendicular polarization through. As a result, the light polarization after the analyzer is not linear, but elliptical. Incoming elliptical polarization on the quarter-wave-plate produces further distortions in the light polarization after the plate (in addition to distortions caused by plate imperfections). This, in turn, leads to unequal grating response.

The problems with imperfect quarter-wave-plate and analyzer can largely be overcome by one of the following instrumental adjustments. First, an achromatic quarter-wave-plate can be used. Such wave-plates produce almost perfectly circular polarization (within 2-3%) in broad spectral range (for example, 630-835 nm). Further, a crystal-based analyzer with high suppression ratio can be used. However, in most cases such analyzers are tailored for a specific wavelength. As a result, a different analyzer is needed for every laser in the system. Currently, such wave-plates are relatively expensive.

Secondly, a crystal with well defined, known orientation can be examined. In such a case, relative intensities of the bands under different polarizations can be predicted. Consequently, the response of the grating under different polarizations can be calibrated and taken into account in the examination of unknown systems.

The third option is to use a grating with the smallest polarization dependence in its response. For example, a response of the 1800 gr/mm grating is strongly polarization dependent, while that of a 600 gr/mm is not. It should be noted, however, that the dispersion (separation of different wavelengths) of the grating is proportional to the grating density. As a result, the use of lower density grating reduces spectral resolution of the signal. This reduction can be partially alleviated by the use long focusing distance spectrographs. However, it can still be an acute problem if the examined bands are close (spectrally) to other bands or if the examined band is very narrow (spectrally). Additionally, even with the use of 600 gr/mm, some residual polarization dependence still remains (on the order of 5% change in intensity depending on the incident polarization).

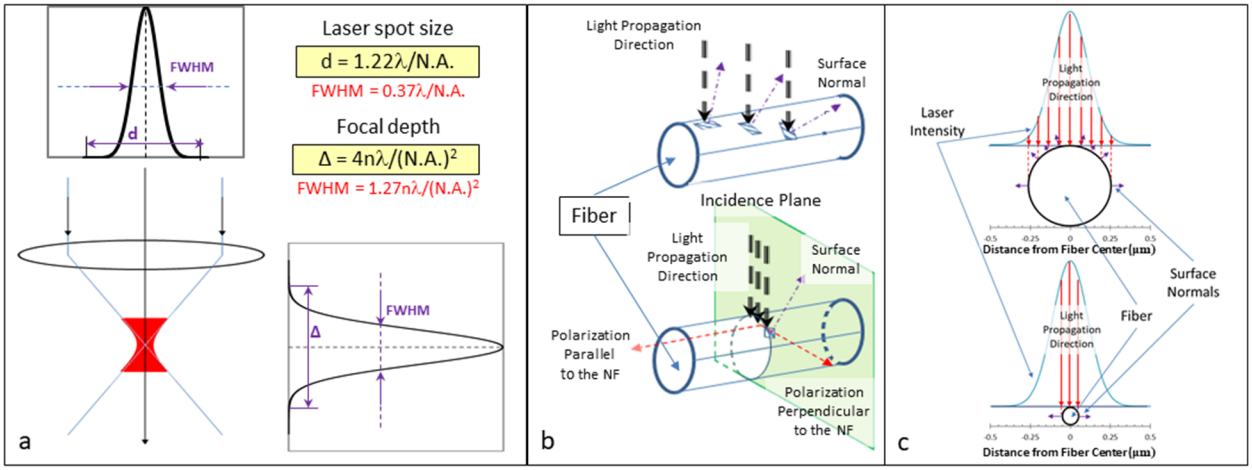

Figure 10: Sources of artifacts in polarized Raman measurements, using multiple polarizations. (a) Schematic of spot size and focal depth in confocal Raman spectroscopy; (b) Changes in the incidence angle due to curvature of the NF surface (top) and relation between the plane of incidence and the laser polarization in NFs resulting in *s*-polarized and *p*-polarized light (bottom); (c) Effect of diameter on total reflectance of the fiber. The panel compares the distribution of laser intensity in the fiber cross-section for diameters of 500 and 100 nm (drawn to scale). For larger fibers, laser intensity at large incidence angles is small, reducing the amount of reflected light. For smaller fibers, laser intensity is almost constant for all incidence angles, and the total reflectance is large.

An additional significant potential artifact is due to slight movement of the nanofiber during the experiment or the polarization switch. This movement can be caused by slight

vibrations in the system, not suppressed by the optical table, or due to physically rotating a half-wave-plate that is inserted in the optical path to rotate the laser polarization. Alternatively, this movement can be the result of areas of the nanofiber suspended in the air over the substrate. This generally happens when the sample is prepared by transferring the nanofiber to the substrate rather than spinning directly on it. The nanofiber movement can be either vertical or lateral (see Fig. S3 in SI for comparison of this effect in fibers with 1 μm and 100 nm diameters and system parameters used in our experiments).

In cases where large fiber movements are detected, the measurements should be discarded. However, subtle movements may be not detectable with current sample tracking techniques. Even small shifts of the fiber can cause significant artificial changes in the signal. The focal depth and the spot size are proportional to the laser wavelength and inversely proportional to the square of the numerical aperture of the objective used (see Fig. 10a). For example, focal depth for the laser and the numerical aperture used in this experiment (633 nm laser wavelength, and numerical aperture of 0.9), the focal depth is approximately 3 μm and the spot size is approximately 0.86 μm.

NF shift changes the confocal volume (volume producing the Raman signal) for different NF diameters. In addition, laser intensity has an approximately Gaussian distribution with respect to the focal plane (as a function of depth) and the center of the spot (laterally). A shift in the NF axis relative to the focal plane either vertically or laterally will change the amount of material in the focal volume (at or close to the optimal laser intensity). For sufficiently small diameters, the shift can move the focal point outside of the NF altogether. As a result, thinner NFs can produce artificially different intensities at different polarizations due to NF movement during the switch. Lateral movement will produce a significantly larger effect due to the fact that

the lateral spot size is significantly smaller than the vertical dimension of the confocal volume (see Fig. S3 in SI).

The artifacts due to nanofiber shift will be present in any sample. However, their effect, when the sample dimensions (or radius) are larger than roughly twice the wavelength of the laser, diminish dramatically. This relationship between the laser wavelength and the "critical" sample dimensions is true for microscope objectives with large numerical aperture (0.9 in the case of this study). In cases of low numerical aperture (low magnification) objectives, the laser spot size can increase dramatically (spot size would be ~3 μm for the same laser as used in this study and numerical aperture of 0.25 compared to ~0.86 μm for the settings used). Although this increase in spot size will reduce the artifacts caused by fiber movement (due to a more uniform light intensity around the center of the spot and the focal plane), it will also drastically decrease the signal to noise ratio. Under these conditions, the "critical" sample dimensions will be significantly larger than half the laser wavelength.

Since the direction of the nanofiber shift is not systematic, the overall effect of these artifacts will be to increase scatter in the results as nanofiber diameter decreases. This problem will become especially acute for NF diameters comparable to or below the vertical step of the typical microscope stage used in Raman systems (~100 nm).

4.3.2. Artifacts Due to Nanofiber Birefringence and Surface Curvature

An additional effect on the signal under different polarizations is the difference in transmittivity/reflectivity of the material. This difference changes the amount of the incident light going into the material to produce the Raman signal and the amount of the Raman signal coming out.

Materials with preferred polymer chain orientation are expected to be birefringent (see discussion of birefringence in Section 3.2.1). In conventional fibers, differences in refractive index for different light polarizations were shown to be as large as ~0.1 (absolute value) depending on the spinning conditions and the polymer intrinsic birefringence.[120]

For a refractive index of 1.5 (typical for polymers) the reflectivity from a flat surface, when light propagates perpendicular to the surface, is ~4%. An increase in the refractive index to 1.6 would change the reflectivity to ~5%. Consequently, this effect is present in any birefringent media (including films and large fibers), but it is largely negligible. However, NF surface is not flat. As a result, the incidence angle (angle between the normal to the surface and the light propagation direction) on most of the illuminated fiber is different from 0° (see Fig. 10b). Reflectivity of the surface generally increases for large incidence angles (see discussion of when this is not the case below), approaching 100% at 90° incidence angle. Consequently, surface curvature of NFs leads to significant increases in reflectivity. A small relative change in reflectivity will be much more significant when the total reflectivity is large. Therefore, the impact of changes in refractive index become more pronounced.

Light intensity has an approximately Gaussian distribution across the laser spot. As a result, for larger fibers, laser intensity at large incidence angles is small, reducing the amount of reflected light. For smaller fibers, laser intensity is almost constant over the fiber projection, *i.e.* for all incidence angles, and the total reflectance is large (see Fig. 10c for comparison between NFs with diameters of 500 and a 100 nm). In addition, the birefringence of the NFs generally also increases with the decrease in their diameter (due to improved polymer chain orientation), increasing the difference in reflectivity when switching the polarization of the incident light.

Consequently, a combination of these two effects can produce a significant diameter dependence in reflectivity between the different incident polarizations of the laser.

Thus far, only the effect of changes in refractive index due to changes in light polarization was considered. However, in addition, reflectivity will change depending on light polarization in case of NFs even without the changes in refractive index. For collimated beams or small numerical apertures, light polarized parallel to the fiber is perpendicular to the plane of incidence (plane created by the normal to the surface and the light propagation direction). It is thus *s*-polarized. On the other hand, light polarized perpendicular to the fiber is parallel to the plane of incidence, and thus *p*-polarized (see Fig. 10b). In case of large numerical apertures (see Fig. S4 in SI for differences between objectives with large and small numerical apertures) the situation is more complicated as a mix of *p*- and *s*-polarized light is present. However, even for large numerical apertures (due to laser spot symmetry) light polarized parallel to the fiber will be predominantly *s*-polarized, while light polarized perpendicular to the fiber will be predominantly *p*-polarized.

Reflectivity of any surface at most angles of incidence is significantly larger for the *s*-polarized light (the difference is smallest for small angles of incidence). At a certain incidence angle (Brewster angle), *p*-polarized light has perfect transmissivity (no light is reflected). This angle is ~56° for a material with refractive index of 1.5 in vacuum.

Since this effect is a result of sample surface curvature, it can be neglected for large samples since the curvature of their surface is small within the laser spot cross-section. However, similarly to the effect of birefringence, due to the distribution of laser intensity along the NF surface (Fig. 10c), its impact will increase with decrease in NF diameter. In large fibers, laser intensity impinging the sample near the Brewster angle is small compared to small incidence

angles. On the other hand, laser intensity in small NFs will be almost constant for all incidence angles. As a result, the relative change in the total reflectance between the two polarizations will increase for smaller NF diameters.

This source of artifacts is, again, largely unique to NFs. Both for thin films and spherical nanoparticles, an approximately equal mix of *p*-polarized and *s*-polarized light will always be present regardless of the direction of laser polarization. As a result, no artificial change in intensity due to change in the laser polarization will occur. On the other hand, in case of NFs, laser polarization perpendicular and parallel to the fiber axis will produce an unequal mix of *p*- and *s*-polarized light at all incidence angles, including the Brewster angle.

4.3.3. Combined Effects and Approaches to Overcome the Artifacts

All of the above effects result in an intensity from one of the polarizations being artificially stronger than the other. Some of the effects are random in the sense of the difference (for example, changes due to the NF movement). On the other hand, effects due to differences in the refractive index and due to *s* and *p* polarization of the light are systematic. All of the described effects (both random and systematic), with the exception of polarization dependent response of the grating, will increase in magnitude with the decrease in NF diameter. Generally, the described effects are expected to act simultaneously. This complicates any attempt to extract orientation factors from a full set of polarization combinations for a broad range of NF diameters. These artificial changes also have a pronounced effect when indicators of orientation (such as I_{VV}/I_{HH} ratio) are used. It should be noted that the artifacts related to material properties and effects of NF curvature will similarly impact techniques such as FTIR and polarized light microscopy that were described in previous sections when applied to NFs with diameters similar to the wavelength of the light source. This can significantly limit the applicability of these

techniques to ultrafine NFs. This limitation is going to be even more severe in case of FTIR because of the long wavelengths used.

The situation may be further exacerbated when the main component of the Raman tensor for the chosen band is not perfectly aligned parallel or perpendicular to the backbone chain of the polymer. For example, in case of PAN the average angle between the nitrile group and the main chain is ~70°. As a result, the depolarization ratios for the nitrile band are not expected to be as large or change as much with changes in orientation (similarly to the dichroic ratio in FTIR). Therefore, the above artifacts can overwhelm changes in intensities due to changes in the degree of polymer chain alignment. Thus, the observed reversed relationship in the VV and HH intensities found for PAN NFs in Figure 9b is likely to be the result of one of the above effects or their combination.

In summary, caution is needed when methods requiring acquisition of multiple spectra under different polarizations are used. As we have shown here, the artifacts described in this section can significantly skew the results of orientation measurements. Example of PAN shows that, in extreme cases, even the sense of the relationship between intensities under different polarizations can change, leading to *qualitatively* incorrect conclusions.

The artifacts described above result from the use of multiple polarization combinations. One way to overcome these artifacts is by using an “internal standard” band to normalize the intensities of the bands used for orientation studies.[110]

A polarization insensitive band has a constant intensity regardless of the polarization of the incoming light.[121,122] Such a band can appear, for example, when the transition vector of the vibration mode is out of the plane created by the two polarization directions. However, for cylindrically symmetric NFs, any vibration mode will always have an “in-plane” component.

Alternatively, a band that produces constant depolarization ratios under different polarizations regardless of polymer chain conformation can be used.[110] Unfortunately, theoretically predicting whether the band will be affected by macromolecular conformation is extremely difficult. Experimental verification is similarly complex. As a result, most of the approaches simply use a band that "appears to be" constant in intensity.[110]

Care needs to be taken when using the internal standard method. For example, McGraw used this approach to study correlation between band intensity ratios and density of poly(ethylene terephthalate).[123] One of the bands was used to normalize the intensity of other bands. However, Melveger later showed[124] that the intensity of the internal standard band used in reference [123] was not, in fact, a true "internal standard", but was dependent on molecular orientation.

An alternative method that can overcome the artifacts was recently proposed and implemented for amorphous fibers.[19,104] In this method, intensity ratio between different bands under single polarization was correlated to the orientation factors obtained from the comprehensive orientation evaluation. Such a correlation can be found for large samples (such as drawn films, for example) with different degrees of preferred orientations. The degree of macromolecular alignment in these samples can be probed by either the comprehensive Raman analysis, or by FTIR. The orientation parameters are then correlated to a ratio between two different bands under a single polarization, creating a calibration curve. This calibration curve can be used for examination of individual NFs under single polarization. At this stage, no change in polarization is required. This eliminates the artifacts described above.

This approach and analysis requires multiple samples, and acquisition of multiple spectra. However, for a particular material, once the calibration curve is constructed, investigation of NFs is relatively straightforward, and was successfully implemented on amorphous systems.[19,104]

However, both the internal standard, and the calibration approach can be further complicated by changes in crystallinity (in particular, additional corrections might be needed to the calibration curve). Effects of crystallinity changes on the Raman spectrum are complicated and depend on the examined band and material. They can include changes in the Raman shift of the bands, appearance of bands associated with a "crystalline" phase, changes in the width of the band, and changes in band intensity ratios.[125–130] The intensity and the wavenumber of the Raman bands depend on the local environment (*i.e.* proximity of other groups, angles between the different bonds, *etc*.). Changes in crystallinity result in changes in the local environment. Higher crystallinity leads to a more uniform environment, and, as a result, to narrower bands (band broadening is the result, in part, of frequency shifts due to different environments present). In addition, crystalline phases can sometimes be associated with specific macromolecular conformations. This leads to changes in band intensity ratios for different conformations, when crystallinity changes.

Impacts of crystallinity and orientation are not easily separated.[126,127,129,131] To fully disentangle these effects, crystallinity and orientation need to be varied independently. In unoriented samples, degree of crystallinity can be controlled by annealing.[125] However, for oriented samples, independent control of macromolecular alignment and crystallinity is difficult. As was discussed in the *Introduction*, in conventional manufacturing techniques improvement in preferred orientation often leads to increases in crystallinity. Thus, achieving high macromolecular alignment with low crystallinity is especially problematic. At the same time,

such orientation/crystallinity architecture is the most relevant to electrospun NFs with unique mechanical performance (simultaneously ultrahigh strength and toughness).[12] As a result, the internal standard and the calibration methods face significant challenges dealing with NFs with variable crystallinity, such as PAN NFs exhibiting unique beneficial mechanical size effects described in ref 12.

4.4. Possibility of Artifact Free Evaluation of Orientation in Nanofibers with Subwavelength Diameter by Two Band Ratio under Single Polarization

Similarly to the simplified Raman analysis described in Section 4.2 above, ratios of intensity between different bands under a single polarization combination can be used as qualitative indicators of macromolecular orientation when appropriate bands are chosen. For example, different band ratios were used in the past to examine polymer chain orientation and crystallinity in conventional poly(ethylene terephthalate) fibers.[127,128]

A simple, quantitative comparison between different samples can be performed, using a single polarization (either VV or HH), if two bands are differently polarized (*i.e.* their polarization is at a different angle to the polymer backbone chain). An optimal choice of bands (to get the maximum change in intensity ratio with the change in polymer chain orientation) would utilize bands polarized parallel and perpendicular to the backbone chain. The ratio between such bands will increase under VV polarization with the improvement in preferred orientation of the backbone chain along the NF axis. HH polarization and the inverse ratio can also be used.

Such an analysis was recently performed on individual PAN NFs.[119] From Huang and Koenig's work[132] the band *circa* 1355 cm^{-1} in PAN (exact position of the band depends on multiple parameters such as crystallinity and internal stress) is polarized parallel to the main

chain. On the other hand, the nitrile band is polarized close to perpendicular to the backbone chain. These two bands and their relative intensities are shown in Figure 11a. Since the nitrile band is significantly stronger, VV polarization was chosen for the experiments to maximize the $I_{1355}/I_{nitrile}$ ratio. Note that the intensity ratio is not an orientation factor like $<P_2>$, and does not necessarily linearly correlates to it.

Variation in measured $I_{1355}/I_{nitrile}$ ratio is shown in Figure 11b. Scatter in the results was relatively high. That is typical for studies of experimental fibers. However, general trend in the Raman intensity ratio as a function of NF diameter is still readily apparent, showing significant increases for fine nanofilaments. This size effect in polymer chain orientation correlates well with the increases in NF modulus (see Fig. 1a).

The observed significant increase in the $I_{1355}/I_{nitrile}$ ratio is especially impressive given the fact that the nitrile group is not fully perpendicular to the main chain. This fact reduces the changes in the $I_{1355}/I_{nitrile}$ ratio with the improved chain orientation.

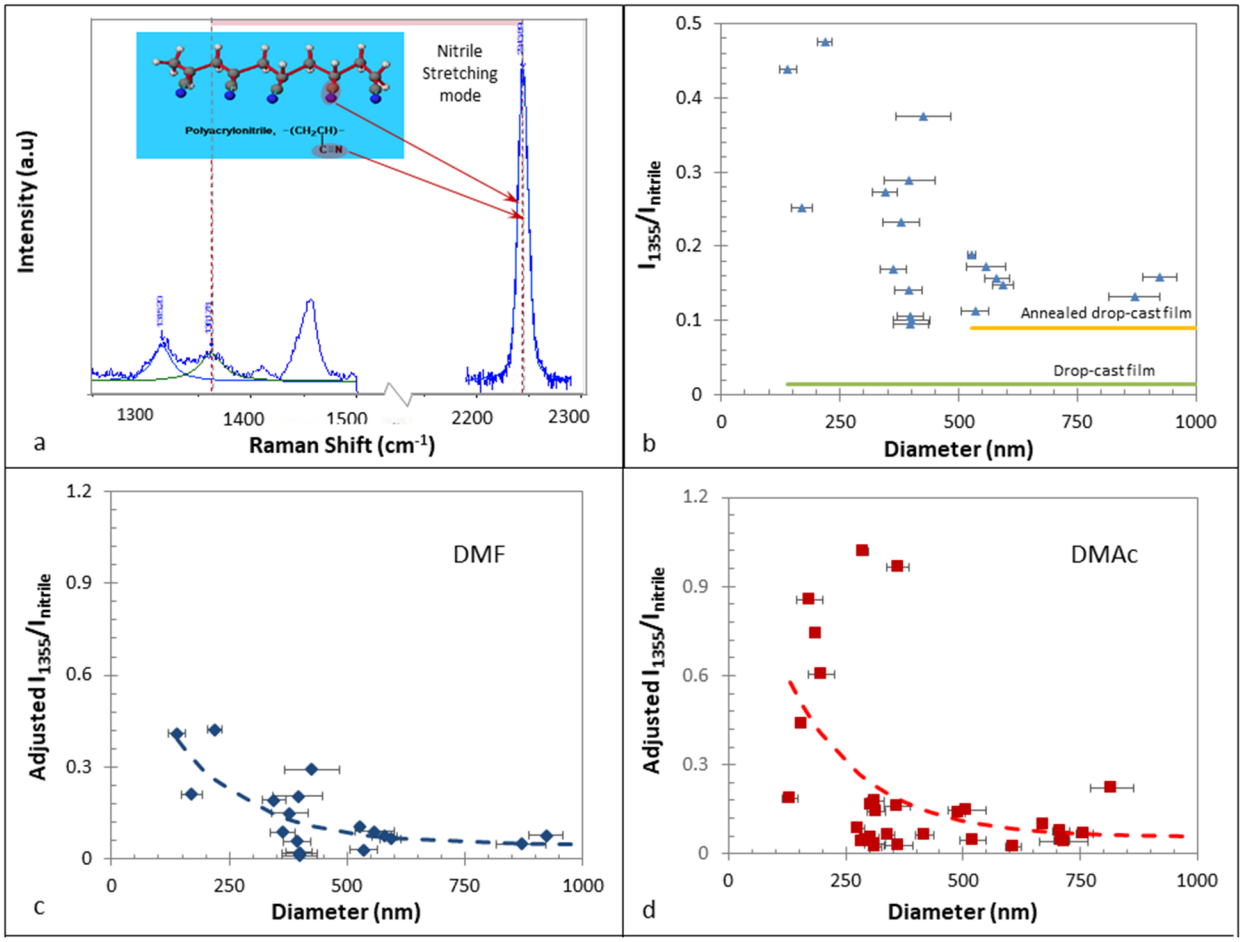

Figure 11: Examination of polymer chain orientation using two band intensity ratio at single polarization combination in Raman spectroscopy. (a) Raman bands used to calculate intensity ratio as a measure of polymer chain orientation; (b) Size effects in the Raman band intensity ratio measured for individual nanofibers of different diameters, compared to the ratios for the as-drop-cast (green line) and annealed (orange line) PAN films. Comparative examination of $I_{1355}/I_{nitrile}$ corrected for changing crystallinity for PAN NFs spun from (c) dimethylformamide (DMF) and (d) dimethylacetamide (DMAc). Adapted from ref [119].

As mentioned, changes in crystallinity in PAN NFs can have an effect on the Raman intensity of the different bands. This effect may overlap with and/or distort the effect of polymer chain alignment. Effect of crystallinity on the $I_{1355}/I_{nitrile}$ Raman intensity ratio was examined on films with no preferred polymer chain orientation, and a correction was introduced[119] (see SI for typical XRD diffractograms used for crystallinity calculations). The modified method was used

for first comparative study of size-dependent orientation in NF families spun from different solvent systems (see Fig. 11c,d).[119]

In most previous studies of orientation in polymer NFs, only modest, gradual increase was demonstrated with the decrease in NF diameter (see *e.g.* ref [34]). This is most likely due to the fact that NF bundles were examined. However, examination of the Raman intensity ratio in Fig. 11c,d shows a sharp dependence on NF diameter. The ratio increased approximately eight-fold for NF diameter decrease from ~500 nm to ~140 nm. Size effect in orientation factor that was qualitatively more similar to this study was observed in recent studies of atactic polystyrene.[104] Note however, that the thinnest NFs in that work were ~500 nm in diameter. In this study the smallest diameter (~140 nm) was approximately three and a half times smaller, and four and a half times smaller than the laser wavelength used (633 nm). To our knowledge, this is the thinnest individual NF examined by polarized Raman technique to date. This diameter is well within the range of diameters of highest interest for mechanical properties optimization (<250 nm).[12] Demonstrated applicability of the new method for quantitative comparative analysis of nanofibers spun from different solvent systems shows high potential of this technique for fast inexpensive structural size effect studies and for quantitative parametric analyses of effects of processing on orientation. Coupled with size-dependent mechanical evaluation, this will enable uncovering the fundamental processing-structure-properties relationships for various nanofibers.

5. Emerging Techniques for Evaluation of Orientation

5.1. Detection of Fine-Scale Oriented Features by Atomic Force Microscopy

Atomic force microscopy (AFM) is a well-established technique for imaging and mapping local topography and properties of materials. AFM utilizes sharp mechanical probes that can be operated in contact, intermittent contact (tapping), and non-contact modes, each

having distinct advantages for imaging. AFM can resolve single molecules with high-resolution,[133,134] and is sensitive enough to characterize biological macromolecules, such as DNA, in both liquid and nonliquid environments.[135,136]

AFM can be useful for orientation characterization through detection of local topographical or property profiles with high spatial resolution. Early investigations of conventional microfibers using AFM were restricted to characterizing fiber surfaces. These studies revealed highly oriented surface features and ordered hierarchical (fractal) structures in high-performance fibers.[137,138] A critical advantage of AFM is its ability to probe the local mechanical response of materials. Mechanical property mapping, in conjunction with traditional topographic imaging, has been demonstrated on advanced polymer fiber surfaces.[139] Oriented features were identified along the fiber axis and the modulus maps revealed regions of decreased stiffness between these features. Similar AFM capabilities were demonstrated on surfaces of electrospun NFs.[140–142] In one of the latter studies, phase contrast imaging revealed enhanced surface orientation of the phase-separated structure along the axis of an elongated polyurethane nanofiber. However, relating surface information to orientation of substructures within the NF volume is not straightforward and needs to be further studied.

Recently, a novel sample preparation technique utilizing a focused ion beam (FIB) was developed where reciprocal notches are milled into individual fibers to expose the internal surface through guided shear (see schematic in Fig. 12a).[143] The resulting surfaces are subsequently characterized using AFM. In theory, the FIB notches need not to be symmetrical and examination of fiber structure at different depths is possible. This technique has been used to study structure and mechanical properties of several high-performance fibers.[144–146] Topographic and transverse stiffness maps acquired simultaneously revealed highly oriented fibrillar structure

with nanoscale fibrils oriented along the fiber axis. Such fibrils are usually associated with the crystal phase in the highly-crystalline advanced microfibers. Using samples prepared by the above FIB-notch technique, AFM has been recently utilized to characterize interfibrillar interactions in ultra-high molecular weight polyethylene fibers through AFM-enhanced indentation to separate the neighboring nanofibrils.[147]

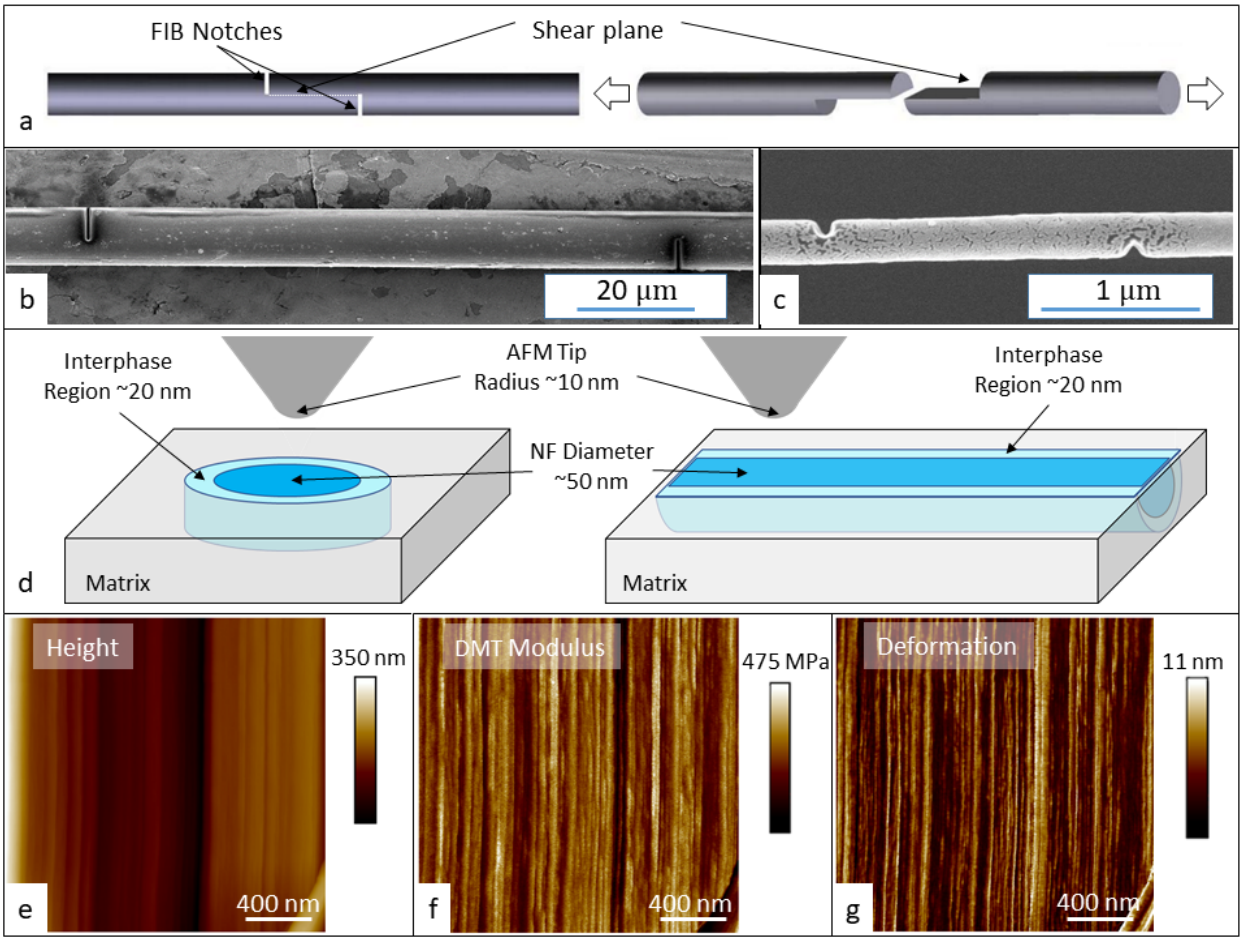

Figure 12: AFM orientation measurements using FIB-notch technique. (a) Schematic of the application of FIB-notch technique to expose the internal structure of the fiber. Adapted from ref [143]; Comparison of notch geometry between (b) conventional and (c) electrospun fibers, showing significantly better notch aspect ratio achieved in conventional fiber; (d) Schematic of mechanical anisotropy measurements on longitudinal and transverse cross-sections of a nanofiber embedded in the matrix, using AFM. The tip size starts to approach NF and interphase dimensions, requiring explicit 3D models for data reduction and property estimation; (e) Topography, (f) DMT modulus, and (g) PeakForce QNM deformation maps of the same internal

area of a high performance poly(*p*-phenylene-2,6-benzobisoxazole) (PBO) fiber. The property maps provide resolution of features not distinguishable in the topography map.

Extending the FIB-notch sample preparation technique to electrospun NFs should allow, in theory, examination of their internal structure, such as dimensions and orientation of crystalline and amorphous regions and interfaces, by mapping topography, stiffness, and other mechanical characteristics. However, achieving shear fracture needed to expose internal structure may be more difficult in NFs (see comparison of FIB-notch geometry between conventional and electrospun fibers in Fig 13b-c). Notch geometry and spacing will need to be optimized. Gallium liquid metal ion sources are used in most FIB systems, but the combination of small NF dimensions and the low thermal conductivity of polymers in general may require alternative techniques for milling high aspect ratio features, such as beams used in helium ion microscopy.[148,149]

One of the consequences of high macromolecular orientation in NFs is their expected high mechanical anisotropy. The difference between the longitudinal and transverse moduli in highly oriented polymer systems and fibers can exceed two orders of magnitude. This anisotropy can have significant effects on the effective properties of nanofiber reinforced composites. AFM can theoretically be used to evaluate such mechanical anisotropy, which can serve as a measure of polymer chain orientation. To obtain anisotropic mechanical data, nanofiber samples can be embedded into a matrix and longitudinal and transverse sections of the fiber can then be examined (see schematic in Fig. 12d). An example of an experiment of this type was performed on a conventional high-performance fiber.[150] Similar studies have been attempted on NFs.[151,152] However, quantitative extraction of NF mechanical properties using this technique may be significantly more complicated for fine NFs. Currently, elastic moduli in AFM and nanoindentation experiments are computed based on one of relatively simple classical

indentation models. These models consider probes of various geometries interacting with a homogeneous isotropic elastic half space. Such models may be appropriate for the analysis of microfibers with fiber diameters significantly larger than the diameter of the probe tip. For ultrafine nanofibers, however, the fiber diameter is comparable to the diameter of the AFM tip. In addition, the interphase region (a volume known to form at interfaces in composites due to physico-chemical interactions between the fiber and matrix) may now be sufficiently large compared to the fiber (see illustration in Fig. 12d). Such an interphase would need to be taken into account. As a result, a full multiphase 3D elastic model needs to be used for accurate data reduction. Nanofiber anisotropy and the generally unknown stiffness distribution through the thickness of the interphase layer further complicates the solution and requires appropriate mechanical assumptions. To our knowledge, no heterogeneous mechanical models have been developed to extract anisotropic fiber properties from nano-mechanics experiments to date. Note that even for conventional micrometer-sized fibers, the above described heterogeneity and anisotropy need to be taken into account if the regions of the fiber close to the interface are probed.

Recently, enhanced AFM techniques such as bimodal amplitude modulation-frequency modulation (AMFM) mode and peak force quantitative nanomechanical mapping (PF-QNM) have been shown capable of producing high-resolution maps of mechanical properties. The former uses two distinct lasers to modulate the cantilever at the first and second resonance frequency simultaneously.[153] Amplitude modulation corresponds to changes in sample topography while modulation of the second resonance frequency is related to changes in material stiffness. In PF-QNM, a high-frequency (2 kHz) force curve mapping technique generates high-resolution maps for modulus, adhesion, dissipation, and deformation, in addition to the

topography map.[154] Figure 12e-g shows that simultaneous mapping of different material properties applying PF-QNM in the section of an advanced PBO fiber prepared by FIB-notch technique resolved ultrafine substructures that were undetected in the topography maps (compare gradual variation of topographic height in Fig. 12e to much finer, higher frequency features on the mechanical maps in Figs. 13 f,g). Similar differences in topographic and property maps of fibers were observed using AMFM technique.[144–146] Combined with the innovative sectioning techniques, demonstrated high mechanical sensitivity and ultrahigh spatial resolution provide an intriguing possibility of performing internal feature metrology in NFs with ultrafine crystalline and pseudo-crystalline (or mesophase) structures that remain elusive to other characterization techniques. The latter structures are of special interest as their mechanical properties may be only subtly different from the properties of the surrounding amorphous phase. Information about presence, size, orientation, and mechanical characteristics of such structures would be invaluable for building more accurate nanofiber structural models. Such models, in turn, can produce critical advances in understanding nanofiber mechanical behavior.

5.2. Micro- and Nano- Focused X-Ray Microscopy with Advanced Light Sources

Initial experiments in quasi X-ray microscopy trace back to the discovery of X-rays in the late 19th century. In the 1950s, the first X-ray microscopy experiments using grazing incidence optics were developed. First lightsource-based X-ray microscopes were constructed in 1970s. Finally, large expansion of interest in X-ray microscopy, which continues to this date, started in the 1990s with the introduction of new equipment and new light sources, especially synchrotron based X-ray sources. Since then, X-ray microscopy has gained a wide variety of applications from soil science to biology and polymer science.[155]

In principle, the limitations of small interaction volumes of X-ray scattering from nanoscale fibers, which led to the demand for the examination of NF bundles, can be overcome by the use of micro- and nano-focused synchrotron X-ray beams. This focusing can be accomplished either through reflection, refraction, or diffraction of an incident synchrotron beam[156,157] with geometries that can be designed to match source parameters to a desired spot size and divergence. Grazing incidence Kirkpatrick-Baez focusing mirrors are typically used to provide high flux micron and sub-micron beam spots for microscopy.[158] Fresnel zone plate diffractive optics have been demonstrated to provide focused beam spots in the tens of nanometers and are commonly used for nanoscale microscopy in both the soft (100-1000eV)[159] and more recently hard (7,000 – 20,000eV)[160,161] X-ray regimes. The fundamental advantage of this approach is the creation of real space microscopy. The samples can be raster scanned to create a spatial map of sample properties, using any of the fundamental contrast modes of X-ray microscopy such as absorption, diffraction or fluorescence.

Scanning Transmission X-ray Microscopy (STXM) methods in the soft X-ray regime have been demonstrated to map local orientation and heterogeneity of biofibers at sub-100nm spatial resolution.[162] This was accomplished by Near Edge Absorption Fine Structure (NEXAFS) spectromicroscopy[163] where the dichroic absorption contrast relative to a linearly polarized X-ray beam is used. Similar technique revealed local radial alignment and a degree of orientation of functional groups in Kevlar fibres.[164] The potential of this method for soft material studies should be carefully viewed in the context of dose limitations due to radiation damage. Even though the X-ray probe is fundamentally more weakly interacting than an electron probe on a per-interaction-event basis, the dose required for either electron or X-ray microscopy to image volumes at a comparable voxel resolution and imaging contrast is comparable or in some cases

higher for X-ray microscopy. This has been explicitly calculated in the case of biological materials and is represented by the highest achievable imaging resolution that can be attained before the sample is exposed to a maximum allowed X-ray dose (where the maximum dose threshold is typically defined as a 50% reduction in scattered intensity). This results in a calculated limit of ~10 nm spatial resolution for X-ray microscopy following the Rose criterion[165,166] vs a ~5 nm resolution limit for electron microscopy,[167] showing the two methods are fundamentally comparable in this regime for biomaterials. The X-ray beam damage can be caused by a variety of interactions with an ionizing beam such as free radical generation, oxidation, chemical activation, differential charging, or local heating, leading to a loss of mass or loss of crystallinity in polymer material.[168] Some of these pathways have been shown to trigger the crystallization of polymer fibers,[169] and even to be unexpectedly present in more dose-tolerant semiconductor materials.[170] Consequently, it is difficult to estimate the damage potential of beam interaction in complex systems.

It has been attempted to overcome these limits by using coherent diffraction imaging techniques which both remove the need for a nano-focused beam and make an explicitly phase-sensitive measurement by using the scattered intensity distribution over a wide range of momentum transfer to iteratively reconstruct a real-space image.[171] However, resolutions even with coherent imaging techniques have not yet been demonstrated past the theoretical limit of direct imaging techniques in the case of biological materials.[172,173] This is most likely due to the fact that the damage limits calculated are based on fundamental contrast efficiency, which remains the same regardless of imaging methodology.

In the hard X-ray regime, the expanded momentum transfer of signal from microfocused beams provide a mechanism for both X-ray diffraction and Small Angle X-ray Scattering

(SAXS) contrast microscopies that are sensitive to local orientation and spacing of fiber bundles.[174] This technique has recently been demonstrated to create a 6D SAXS tomographic map, *i.e.* internal 3D orientation of a 3D voxel, at 100 μm^3 real-space voxel size (see Fig. 13).[175]

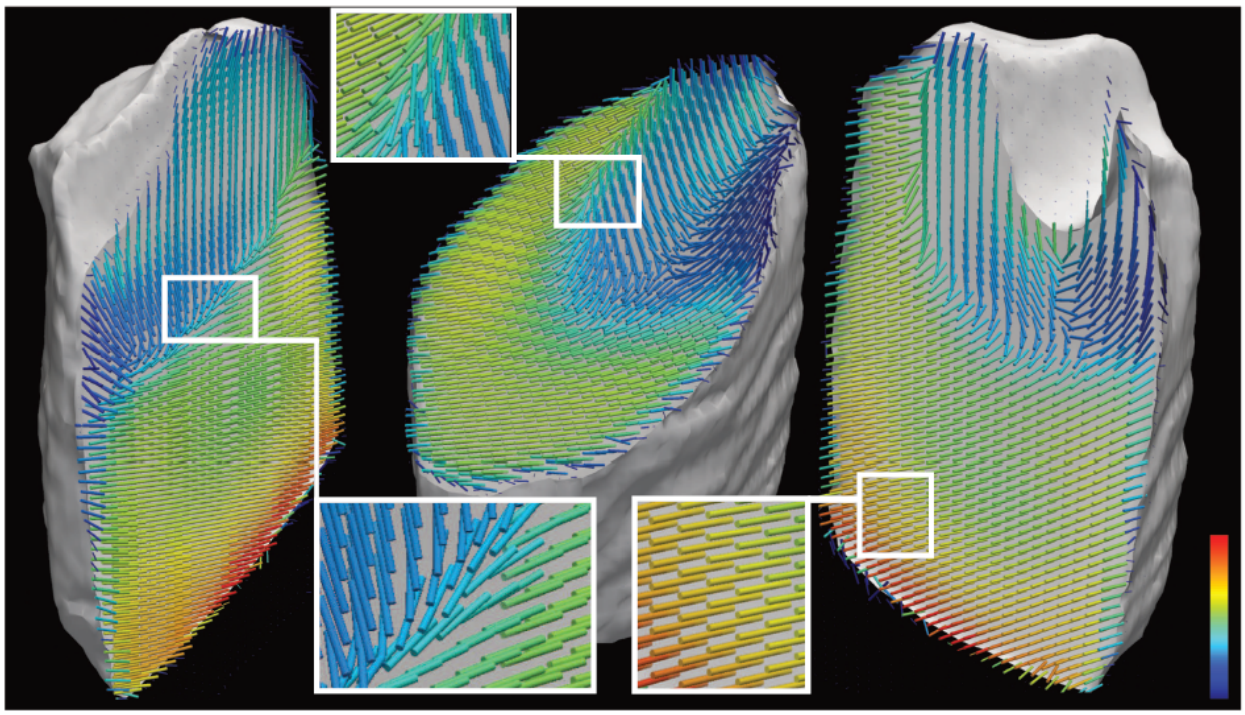

Figure 13: Real space image of collagen fiber within a tooth sample, showing 3D orientation distribution. From ref [175].

Nanofocused X-ray Bragg diffraction microscopy methods to date are typically applied to hard materials in highly crystalline states with known orientations such as epitaxial films and microcrystal materials in both 2D[176,177] and 3D.[178] The experimental realization of nanofocused hard X-ray diffraction microscopy methods gives the tantalizing possibility of single-fiber strain analysis. However, significant challenges are present for attempting orientation studies, using a nanofocused beam on a single fiber as one loses the passive benefit of an orientational average of multiple fibers being present at random positions and attitudes within a larger X-ray beam volume. To attain a single fiber diffraction signal, for example, the passive orientational diversity present in conventional XRD studies must be replaced by a tilt series, typically a rotational scan

of a fiber necessitating 2D maps at each angular position to re-align the nanobeam onto the nanofiber, resulting in significant dosing of the sample to attain any diffraction signal. Planned synchrotron source upgrades to Diffraction Limited Storage Rings (DLSR) such as the Advanced Photon Source Upgrade (APS-U) project (https://www.aps.anl.gov/APS-Upgrade) are expected to create two orders of magnitude improvement in nano-focused hard X-ray flux which may make these measurements feasible in the future. Even more brilliant X-ray sources such as Free Electron Lasers (FELs) give the intriguing possibility of avoiding beam damage limitations altogether in "diffract-before-destroy" single pulse imaging modes which use a femtosecond X-ray pulse so short in time that the entire scattering experiment is concluded before the beam damage can alter the structure of the sample.[179,180] However, these techniques have generally yet to be applied to polymer science.

5.3. Fast Scanning Calorimetry

Another potential emerging technique is fast scanning calorimetry (FSC), also called sometimes flash DSC. In this technique, a very small sample with mass ranging from 50 to 200 ng is placed directly on the sensor rather than into a crucible, like in conventional DSC. The required sample weight corresponds to the weight of 50 mm long section of single nanofiber with diameter in the range from 150-300 nm, that makes this technique potentially useable for interrogation of individual nanofibers. The measured heat flux is proportional to sample mass and heating rate. As a result, ultra-fast heating and cooling rates can be used, while retaining sensitivity. This technique can provide information on nucleation[181,182] and crystallization kinetics,[183] and on crystalline reorganization.[184] High scanning rate available with this technique allows determination of the heat capacity in polymers that cannot be easily amorphisized. It is also well suited for studying structural recovery[185,186] and early stages of polymer degradation.[187]

It offers the possibility to magnify changes in recovery kinetics due to structural constraints,[188] which could become a criteria for investigation of macromolecular alignment. In addition, this technique has shown great potential for investigating thermal events in material for which degradation under standard DSC conditions can occur. Examples of such materials include PAN, various silk proteins[189] and starch.[190]

Combination of FSC with other techniques such as X-ray microscopy offers an intriguing possibility of *in-situ* evaluation of structure formation. FSC was used in conjunction with synchrotron WAXD to study crystallization processes in high density polyethylene and polyamide.[191] It was also used together with nano-focus X-ray scattering to investigate the phenomenon of multiple melting behavior of poly(trimethylene terephthalate).[192]

Some non-equilibrium structures, which are hard to observe otherwise, can be produced in FSC. Micro-focus wide-angle X-ray scattering (WAXS) has been used to analyze polymorphism in isotactic polypropylene and polyamide 6 crystallized in a fast scanning chip calorimeter.[193] This capability may be of significant interest to studying structures of electrospun NFs, as fast solvent evaporation can theoretically create non-equilibrium structures similar to the ones produced by fast quenching.

One of the challenges for accurate FSC measurements is achieving good thermal contact between the sample and the sensor. An imperfect thermal contact is likely to result in broadening of the signatures related to each thermal event. Poor thermal contact can be severe in case of electrospun NFs, when porous mats of overlapping fibers are used. Low intrinsic thermal conductivity of polymers coupled with the fact that the bulk of the nanofiber sample will not be in direct contact with the sensor can lead to slower and more inhomogeneous heating. An example of consequences of poor thermal contact can be observed in the investigation of melting

behavior of electrospun polyamide fibers.[194] The authors observed thermal lag that intensified and became significant for heating rates above 500 K min^{-1}. Recently, possibility of fast scanning calorimetry with heating rates up to 2000 K s^{-1} was demonstrated on electrospun fiber bundles.[195] Fibers of poly(ethylene terephthalate) (PET) were directly spun on transmission electron microscopy copper grids. The grid was cut and placed on the chip sensor. Direct spinning is claimed to have improved the thermal conductivity between the sample and the sensor. However, provided images of nanofiber samples allow to suggest that only a few nanofibers in the bottom layer of the bundle were in direct thermal contact with the copper grid and there were fibers spanning holes in the grid, suggesting that thermal conductivity needs to be further improved.

The problem of poor thermal contact can possibly be alleviated by better sample preparation. For example, rarified aligned NF arrays (with minimum or no NF intersections – see examples of highly aligned spaced nanofibers in ref 6) can be spun on metallic substrate. This will assure good contact with a thermally conductive substrate. Alternatively, longer sections of individual NFs can be used. In the latter case, the NF sample needs to be coiled on a thermally conductive surface. Coiling can be achieved by proper nanofiber deposition control.

To our knowledge, no investigations of individual NFs using FSC were carried out to date. Our recent attempt to examine individual NFs using this technique showed promise, leading us to believe that with improved sample preparation such examination is possible.

5.4. Near-field Scanning Optical Microscopy (NSOM/SNOM)

Near-field Scanning Optical Microscopy (NSOM or *SNOM)* is a family of experimental techniques that can provide optical information with sub-diffraction-limit resolution. In traditional, far-field optics, the resolution is limited to approximately half the wavelength of the light. In order to overcome this limitation, near-field microscopy makes use of evanescent or

non-propagating fields that are present only near the surface of the object. Imaging beyond the diffraction limit was first proposed in 1928.[196] However, technical limitations limited widespread application of the approach until much later. Because the intensity of the evanescent field drops off exponentially with the increase in distance from the surface, the probe needs to be placed very close (typically within a few nanometers) to the surface. This distance is generally kept constant through either shear or normal force feedback mechanisms.

Near-field microscopy can examine several phenomena that have an equivalent in classical optics, such as reflection, absorption, scattering, and emission. In addition, it can provide information on uniquely near-field phenomena such as Förster transfer of excitation energy and localized plasmon resonance.[197]

Two different approaches are used to confine the light to the small area of the sample. The first one (aperture or *a-NSOM*) uses sub-wavelength aperture (on the order of 50-100 nanometers). In this approach the probe is generally either a tapered optical fiber coated with metal except for the opening at the end, or a traditional AFM tip with a hole in the center. The second approach focuses the light on a solid tip and is called scattering or *s-NSOM*.

5.4.1. Aperture Near-field Scanning Optical Microscopy (a-NSOM)

a-NSOM can be used in several configurations. In the illumination mode, the light is provided through the probe and then collected either in transmission, reflection, or scattering. In the collection mode, the light is generally provided from the bottom of the sample by a far-field source, while the collection is done by the probe through the aperture.

In general, *a-NSOM* can be used in a similar manner to traditional optical microscopy, including with polarization control. However, it faces several significant challenges. Metallic coating around the aperture produces significant losses that increase exponentially with increase

of the ratio of light wavelength over the size of the aperture.[197] Polarization of the light also deteriorates as the signal propagates through probe.[198] As a consequence, the practical resolution limit of *a-NSOM* is on the order of 50 nanometers, when used with visible light,[197] long scan times are needed, and vibrational spectroscopies such as FTIR are not practical for submicron feature sizes.[197] Although Raman spectroscopy using *a-NSOM* was demonstrated for some material systems,[199] it is generally impractical due to weak signal. In addition to the above limitations, *a-NSOM* technique can suffer from a variety of artifacts. The most severe of these are the so-called "*z*-motion" artifacts.[200,201] These artifacts cause the signal to correspond to sample topography rather than optical properties.[200] As a result, these artifacts can severely limit the application of *a-NSOM*.[201]

Despite the above limitations, *a-NSOM* version of techniques such as fluorescence spectroscopy,[202] polarization modulation (PM) optical microscopy,[203,204] as well as measurements of birefringence[205] are theoretically possible. Application of these techniques for macromolecular orientation quantification is similar in theory to their far-field counterparts (see Section 3.2), but with better spatial resolution. In case of NF examination, these techniques have an advantage of interaction area being smaller or comparable to NF diameter. This can potentially allow for orientation mapping along and across the NF.

However, *a-NSOM* measurement of birefringence faces limitations similar to its far-field counterpart (see Section 3.2.1) – *i.e.* difficulty with disentangling the signal from the crystalline and the amorphous phases, which have different intrinsic birefringence, and different reflectivity from the curved surface of the NFs for light polarized parallel perpendicular and to the NF. The problem of the effects of the crystal vs. amorphous phases might be even more acute in case of *a-NSOM* version of the technique. The aperture size (and lateral resolution) is comparable to

crystal sizes observed in NFs. As a result, at the very least, this will cause additional scatter of the results due to the waveguide tip movement over the different phases.

In addition, mapping of curved surfaces (such as in the case of NFs) faces a further complication. Intensity of the near-field signal deteriorates with the increase in distance between the probe and the subject. If the curvature is significant, there will be a distribution of distances between the probe and the sample across the spot size even if constant central distance is maintained (see example of a 50 nm sized aperture probe over NFs with diameters of 500, 200, and 50 nm in Fig. 14a). This distribution will change depending on the location in the map. As a result, the observed intensity will be artificially changed regardless of the orientation features. The problem will intensify as the curvature becomes larger (smaller NF diameter) relative to the aperture size. In comparative studies, even if the aperture is perfectly centered over the NFs, the distribution of distances will be change for different NF diameters (see the example of NF with 50 nm diameter in Fig. 14a). In general, the interaction between evanescent field and the curved surface needs to be further studied.

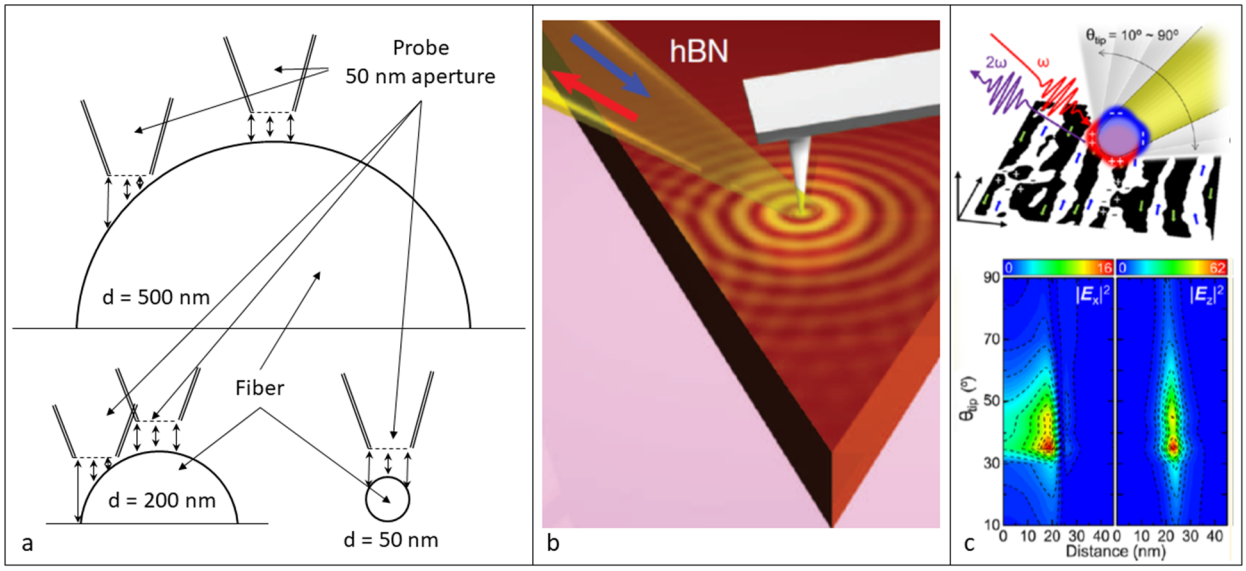

Figure 14: NSOM application. (a) Effect of NF diameter and curvature on the distribution of distances between the *a-NSOM* probe aperture and the surface. The distributed distance is expected to affect the evanescent light region and, therefore, the collected light characteristics;

(b) Traditional application of *s-NSOM* where the tip is illuminated by light at an angle to the surface, producing vertical and horizontal polarization. Adapted from ref [206]; (c) The use of inclined probe to vary the proportion of in-plane and out-of-plane polarization. Adapted from ref [207].

Quantification of macromolecular orientation in electrospun NFs was attempted using polarization modulation near-field optical microscopy (PM-NSOM).[208] The authors examined ribbon-shape NFs with approximately 1.6 μm X 140 nm cross-section and observed significant preferred orientation at the center ("core") of the NFs as expressed by the dichroic ratio. However, surprisingly, the dichroic ratio changed sign near the edges of the NF (the volume called "sheath" by the authors). This result was interpreted as indication of radial arrangement of the polymer chains within the NF sheath.[208]

Radial arrangement of polymer chains in the "sheath" is unlikely from the physical standpoint. In fact, since the solvent evaporation rate is highest at the surface of the electrospun jet, the degree of macromolecular orientation is expected to be highest in that area. Consequently, the observed switch in the dichroic ratio at the edges of the NF was likely the result of changing reflectivity between the different light polarization in the areas with pronounced curvature, as described in Section 4.3.2. This result indicates that the artifacts described in this work, stemming from different reflectivity of the curved surface due to polarization switch, could limit the application of *a-NSOM* version of the optical approaches described in Section 3.2 as well. Similar limitations would apply to any other technique that requires a switch in the polarization of the incoming light.

5.4.2. Scattering Near-field Scanning Optical Microscopy (s-NSOM)

In *s-NSOM* light is focused on a sharp metalized tip (generally an AFM tip) that is used as the probe. The apex of the probe tip enhances the light field in the immediate vicinity, acting as an antenna. The high evanescent field is confined to a volume with lateral dimensions of

approximately one radius of curvature of the tip apex. In case of *s-NSOM,* the confinement effect depends only on the apex radius, and is independent of the wavelength of the incoming light, which distinguishes it from both the far-field optics and from *a-NSOM*. As a result, this technique can produce nanometer resolution with a broad range of light wavelengths, including the mid-infrared region.[197] Several configurations of *s-NSOM* exist. Illumination can be brought in from the bottom in case of transparent samples, or from the side. Signal collection can also be placed either below or above the sample.

The current model of *s-NSOM* is the "lightning rod" model, which builds on the early "dipole" models.[209] It is generally believed that the light in the evanescent region is polarized along the probe axis (*i.e.* perpendicular to the sample surface) with no in-plane polarization components. This makes approaches such as PM optical microscopy or traditional birefringence measurements currently impossible with *s-NSOM*. However, recent experiments showed that an in-plane polarization may exist as well.[206] This may be due to the fact that the *p*-polarized incoming light delivered through the beam with non-zero incident angle (in the most popular *s-NSOM* configuration as shown in Fig. 14b) always has an in-plane polarization component (in addition to the vertical component exciting the "dipole"). In addition, it was recently shown that the light polarization direction can be altered through the use of an inclined probe (see Fig. 14c).[207] Implications of this possibility for macromolecular orientation quantification and the application of the above techniques can be profound and need to be further explored. It is, however, likely that the *s-NSOM* versions of PM microscopy and birefringence measurements would face the same challenges due to high sample curvature as the approaches based on *a-NSOM*.

In context of macromolecular orientation in fine NFs, *s-NSOM* versions of infrared and Raman spectroscopies would be of particular interest. Application of *s-NSOM* for infrared microscopy will be discussed in Section 5.6.

Tip-enhanced Raman spectroscopy (TERS) is a version of surface-enhanced Raman spectroscopy (SERS) where the Raman signal is enhanced by the presence of metallic nanoparticles. It can be considered as a *s-NSOM* version of Raman microscopy. TERS has been extensively studied (see *e.g.* refs [210–213]) and large enhancements of the signal were reported in the past. The enhancement calculations take into account the difference in the signal producing volume. Significant experimentation with tip coating and probe-sample distance needs to be undertaken in order to obtain best signal enhancement. However, in practice, the most important parameter is not the signal enhancement, but contrast (the ratio between the near-field to far-field signals).[212] This contrast determines whether the near-field signal can be separated from the background. Far-field signal can be partially suppressed by crossed polarization schemes in order to improve the contrast.[212,214] However, conditions for maximum contrast and maximum signal intensity are not the same, and often contradictory.[212] In addition, care needs to be taken as some spurious far-field signals, such as reflections from the pyramidal tip surfaces rather than signals from the apex region, can still remain even after suppression.[212] Importantly, for the purposes of this paper, the near-field Raman signal appears to be less polarization sensitive and might not be suited for orientation measurements.[212] Better understanding of polarization of the evanescent light in *s-NSOM* / TERS is needed. A version of the simplified Raman approach, using two bands ratio, proposed in Section 4.4, may be applicable. It should be noted, though, that the correction for crystallinity discussed earlier in this paper will be more difficult in the case of TERS than in the far-field Raman microscopy. Measuring local crystallinity under the tip is

difficult if not impossible. In addition, the crystal size in NFs is similar to the tip size. Both of these facts would lead to increased scatter in the results.

5.5. Combined Infrared Spectroscopy and Atomic Force Microscopy

Several promising techniques combining infrared spectroscopy and Atomic Force Microscopy (AFM) have been introduced in recent years. These techniques preserve the rich structural information provided by IR spectroscopy but provide much improved spatial resolution approaching the AFM tip radius, well below the far-field diffraction limit at IR wavelengths. The two main techniques are photothermal induced resonance (PTIR) spectroscopy, also called NanoIR or AFM-IR, and infrared scattering-type near-field optical microcopy (IR s-SNOM), also called Nano-FTIR when using a broadband IR source. Although both techniques combine AFM and infrared spectroscopy, their principle of operation is different.

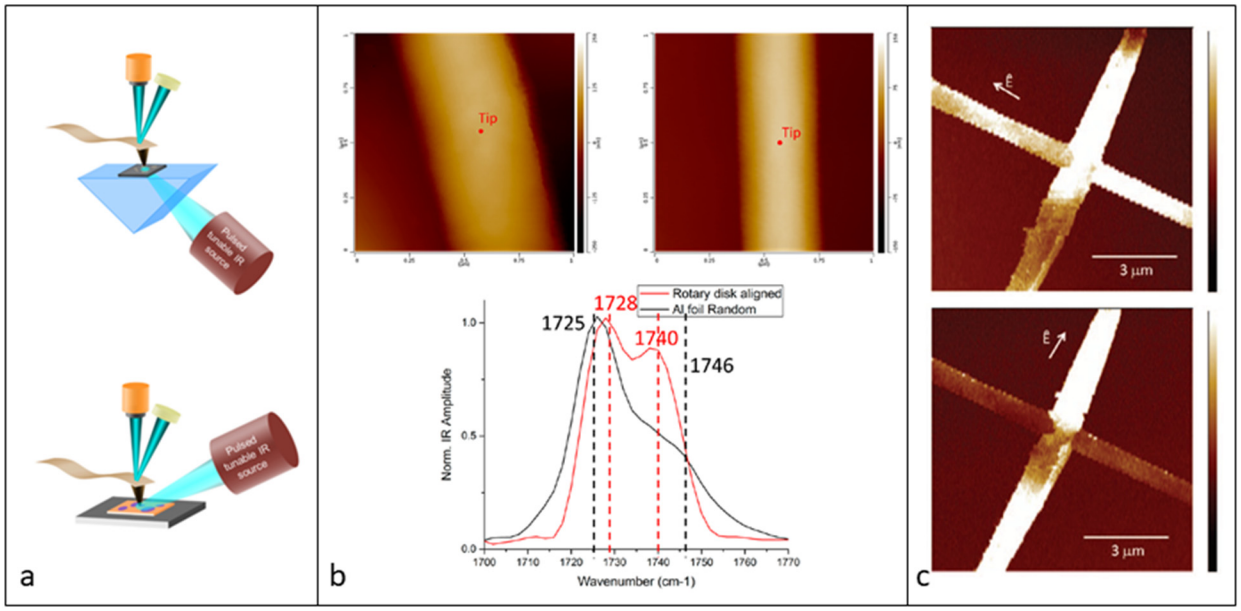

Figure 15: Applications of PTIR technique in the literature. (a) Top: the original AFM-IR configuration with bottom side illumination and the sample mounted on an infrared-transparent prism. Bottom: topside illumination, enabling sample measurements on arbitrary substrates; (b) AFM images and IR spectra of individual electrospun NFs, showing different phases as a result of different collection methods (adapted from ref [50]); (c) IR absorbance images of two PVDF fibers collected with the pulsed laser source tuned to 1404 cm^{-1} by using light polarized in the

two orthogonal directions indicated. Lighter color indicates stronger absorbance at that wavenumber (adapted from ref [215]).

PTIR[215,216] uses a tunable infrared laser to sweep through the mid-IR region. Absorption at a certain wavelength results in heating and thermal expansion of the sample. This localized expansion is recorded by AFM by probing the deflection of the AFM tip (see Fig. 15a). Spectra obtained by this technique were shown to correlate well to those obtained by FTIR as the photothermal effect is proportional to the absorption index. Recently, this technique was used to distinguish between different crystal phases in individual NFs (see Fig. 15b)[50] and even to map the distribution of crystal structures in the nanofiber, revealing the formation of a 10 nm thin shell containing an unusual crystal polymorph.[217] By rotating the intrinsically polarized laser light, the method has been used to probe anisotropy in organic thin films and plasmonic systems[218] and is also expected to be suitable for examining polymer chain orientation in individual NFs. Qualitative examination of single PVDF fibers with diameters of ~1 μm was demonstrated (see Fig. 15c).[215] However, suitability of this technique for quantitative analysis of NFs in the ultrafine diameter region is yet to be demonstrated. A limitation of earlier generations of PTIR instruments was the need to use the AFM tip in contact mode which is not well suited to the cylindrical shape of NFs. Recent instrumental developments, in particular the resonance enhancement of the signal when using quantum cascade lasers and the implementation of tapping mode AFM sampling, make PTIR a promising technique to study the molecular structure in individual nanofibers.

In Nano-FTIR, a technique derived from scanning near-field optical microscopy discussed in the previous section, a sharp metal-coated AFM tip is illuminated by a broadband IR source and the tip-scattered light (typically back-scattered) is collected as a function of the tip position and analyzed interferometrically.[219–221] In contrast to PTIR, analysis of the optical

amplitude and phase of the scattered light enables extracting the real (n) and imaginary (k) parts of the complex refractive index of the sample, the latter being generally comparable to standard FTIR absorption spectra.[221]

The technique has been used for chemical mapping with nanoscale resolution[221] and for structural analysis and mapping of individual protein complexes.[222] Figure 16 illustrates the use of Nano-FTIR to map different phases in individual electrospun NFs (images and spectra were acquired using a neaSNOM microscope from neaspec GmbH, Germany). However, direct applicability of this technique for quantification of macromolecular orientation is yet to be demonstrated. As in other *s-NSOM* based techniques, light in Nano-FTIR is primarily polarized perpendicular to the surface due to antenna effect of the metal-coated AFM tip. This enables probing out-of-plane orientations but, as was discussed in the context of traditional FTIR, polarization parallel to fiber axis is also needed in order to obtain orientation factors of NFs.

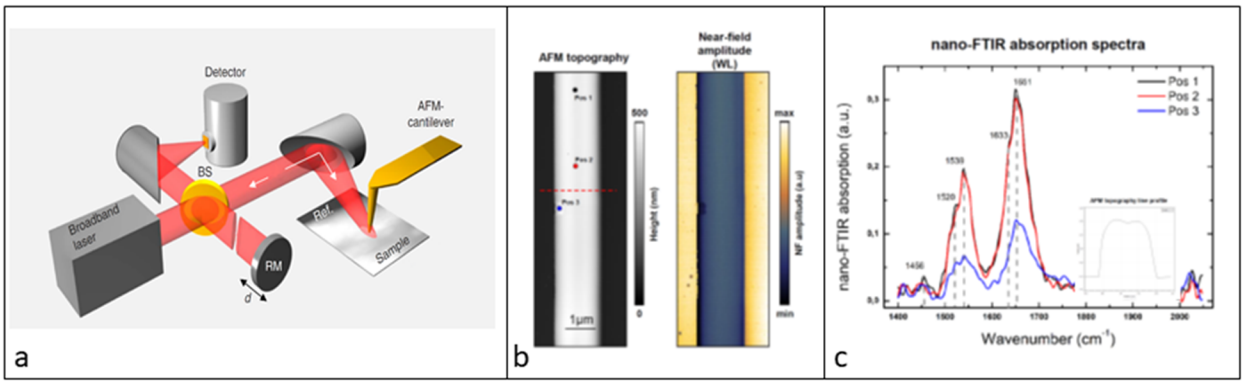

Figure 16: Nanoscale spectroscopic mapping in individual electrospun silk NFs using nano-FTIR. (a) Nano-FTIR technique based on s-SNOM using broadband IR radiation focused in the near-field using an AFM tip (modified from ref [223]); (b) AFM imaging of individual electrospun NFs; (c) Nano-FTIR absorption spectra measured at three different locations on the NF marked in (b). The inset shows AFM topography line profile corresponding to the dashed line in the left image in (b).

As was mentioned in the previous section, recent experiments showed possible presence of in-plane polarization components in the evanescent *s-NSOM* volume. If these components can be controlled to produce polarization in the direction of the fiber, it might be possible to obtain

infrared dichroism values, and, consequently, orientation parameters. Such a technique could still be affected by some of the artifacts described in Section 4.3.2. However, as the lateral dimensions of the examined area in the case of *s-NSOM* are comparable to the size of the tip apex, they can be made very small (5-10 nanometers). Consequently, the effects of local curvature are likely to be less severe than in the case of Raman microscopy.

Even if full examination of infrared dichroism by Nano-FTIR is not possible, qualitative indicators of orientation can be obtained by examining the ratios of bands that are differently polarized (similar to the polarized Raman approach described in Section 4.4). These orientation indicators can then be used for comparative studies. Use of Nano-FTIR for orientation evaluation was demonstrated in organic semiconductors[224] and collagen nanofibrils.[225] However, to our knowledge, polymer chain orientation in electrospun NFs was not yet evaluated using this approach. It is also important to note that similarly to the Raman approach, effects of changing crystallinity will need to be addressed.

6. Addressing Sample Preparation Limitations

6.1. NF Bundles

In addition to new or modified interrogation techniques, one can attempt to improve sample preparation methods. Currently, oriented NF bundles are prepared by direct electrospinning using one of several available NF alignment methods.[6] The resulting partially aligned NF assemblies or sheets are sometimes further post-processed using techniques such as bunching, rolling, twisting, or stretching (note that the latter may affect native chain orientation in individual nanofibers). The above protocols result in samples with distributed NF diameters and orientations within the bundle. These distributions often become broader as NF diameter decreases and/or the bundle diameter (*i.e.* sample size) increases.

It might be possible to apply some of the techniques described in Section 2 (*e.g.* XRD, FTIR, and DSC) to smaller NF bundles. If the bundles are small enough, it should be possible to construct them by picking and assembling selected individual NFs. Such an approach could result in narrower NF diameter and orientation distributions. Automating this proposed protocol of nanofiber-by-nanofiber sample assembly can lead to larger uniform samples and more accurate orientation information obtained using the techniques discussed in the previous sections.

Another possibility is modeling-assisted process control. Electrospinning is a complex multi-parameter process. Empirical optimization of such processes has limits. Models, describing jet instabilities and deposition on static or moving substrates[226] can guide experimental NF assembly and orientation control. Nearly perfect alignment is possible in special cases with proper process optimization.[6] Multiphysics continuum jet models that include solvent evaporation would be invaluable for precision control of NF diameter.

6.2. Individual NFs

As discussed above, NF properties and structure are strongly diameter-dependent in the ultrafine diameter range. Methods of chain orientation evaluation applicable to individual NFs are best suited for studies of structural size effects. Precise diameter measurement and ensuring diameter uniformity within the interrogated section of the NF are critical for such studies. Pronounced beading due to onset of capillary breakup instability in dilute solution jets can significantly affect the outcomes as beads can occupy substantial fraction of the sample volume. However, this instability usually produces beads in the micrometer diameter range that are relatively easy to detect and avoid by discarding the affected samples. Subtler variation of NF diameter that is more difficult to detect can still adversely affect the results by increasing the

experimental scatter (in case the diameter measurement error is randomized) or even leading to systematic errors.

Accurate measurement of NF diameter is not trivial. Optical evaluation is generally diffraction limited and cannot achieve accurate measurement for NFs in the diameter region of highest interest. Currently, the most reliable method to measure the diameter of ultrafine NFs is scanning electron microscopy (SEM). However, diameter measurement on the section to be structurally interrogated can affect the sample, even if environmental SEM modes are used with no fiber coating. NF continuity and generally weak diameter variation along the nanofiber axis (in absence of beading) allows to overcome this problem. Currently the best practice employed in our labs is to collect and analyze two adjacent sections of the same fiber. One section is evaluated in an SEM to accurately measure NF diameter, while the other is used for structural studies. This approach was used in our previous mechanical studies.[12,227] NF diameter is measured in several locations along the fiber, and if significant variation is observed, the sample is discarded. For samples with no systematic diameter variation, structural studies are carried out on the second, virgin NF section.

The above approach can be further expanded and used with several structural characterization techniques or simultaneous structural and mechanical characterization on the same nanofiber. Such multimodal characterization would require collection of three or more adjacent sections of NF. Evaluation of the structure of the same NF by several methods can significantly improve the accuracy of the method comparison studies. Such studies are important for evaluation of new techniques through their comparison to established methods. Use of the same NF for structural and mechanical testing (the latter known to produce especially high experimental scatter) can substantially reduce scatter and enable direct correlation of structural

features to observed mechanical behavior of individual NFs. Such correlation would enable better identification of mechanisms of NF deformation and failure and could accelerate analysis of fundamentals of the unique mechanical size effects.

7. Special Cases and Limitations

7.1. Changing Phase Composition

So far in this review we have considered the case of ultrafine NFs with low and variable crystallinity. We have shown that the degree of macromolecular alignment in such NFs can be quantified, for example, by a modified polarized Raman spectroscopic technique, which can also account for changing crystallinity of the NFs with different diameters. Other techniques such as Nano-FTIR can potentially be used in a similar way, although accounting for crystalline structure can be more difficult in these cases. However, the discussion so far focused on a relatively simple case when the structure of the polymer is described by a simple two-phase (amorphous-crystalline) material model. Already in our discussion of DSC/DRS experiments we touched on the fact that such a model is most likely insufficient, as the amorphous phase of the polymer can include both mobile and rigid fractions. In addition, presence of a mesophase is a possibility in electrospun NFs as well.[19]

Our recent examination of electrospun Nylon 6 NFs showed that a further complication is possible. XRD, DSC, and Raman examinations indicate that not only the crystallinity of NFs changes with the decrease in their diameter, but the crystal phase mix changes as well. Our preliminary investigation showed that thinner nanofilaments contained increasing amounts of metastable γ phase and decreasing amounts of α phase of the polymer (to be submitted). Under these conditions, disentangling the changes in the band ratio (for the simplified polarized Raman analysis) stemming from changes in crystallinity, crystal mix, and orientation is extremely

challenging. One way to solve this problem is to find bands that are only affected by two out of the three factors (orientation, crystallinity, and phase composition). This may or may not be possible for a particular polymer. In the latter case, a complicated series of experiments where the degree of crystallinity and the crystal mix are changed independently in unoriented samples is needed to deconvolute the different effects and to introduce the needed corrections when NFs are examined. Such experiments are not straightforward. Additional studies are needed in these special cases to obtain reliable indicators of polymer chain orientation.

7.2. Chain Orientation vs. Chain Extension

The degree of polymer chain alignment has been identified above as the critical parameter determining the mechanical properties of ultrafine NFs with low crystallinity. Another potentially important parameter is polymer chain extension. It is believed that *fully extended* polymer chains are responsible for high mechanical properties of conventional advanced polymer fibers.[228,229] Chain extension is normally achieved by preventing chain entanglement. Traditionally, in flexible chain polymers such as ultrahigh molecular weight polyethylene (UHMWPE), this is achieved through techniques such as gel spinning. Recently, an alternative route that involves specialized polymerization procedure to produce a solid preform in an unentangled state was proposed and implement to produce high modulus UHMWPE tapes.[230]

In electrospinning, NFs are generally produced from semi-dilute polymer solutions. As a result, polymer chain entanglement is expected to be low, and it is likely that the resulting NFs possess fully or almost fully extended chains. This hypothesis is supported by major increases in modulus and strength of thinner nanofilaments observed in multiple polymer systems. These high property values are generally well in excess of properties of conventional fibers made from the same polymer, and are achieved before significant process optimization. Still, experimental

confirmation of fully extended polymer chain state, and what are the critical parameters needed to obtain it, can be essential to optimize NF properties.

One of the ways to examine the degree of chain extension is by examining the radius of gyration of the polymer chain parallel and perpendicular to the fiber axis using small angle neutron scattering (SANS).[231] This method, which uses the elastic scattering of neutrons to probe length scales from approximately 1 to 100 nm, requires the addition of a deuterated reporter polymer to the electrospun solution. Ideally, the deuterated polymer should have the same molecular weight as the main polymer being investigated to avoid modification of the viscoelastic properties of the solution and any effect of molecular weight on chain extension and relaxation. This is only possible for some polymers such as polystyrene. As a consequence, SANS is essentially only applicable to model systems. It also needs large bundles of fibers to be examined and produces averaged information. Finally, SANS experiments can only be conducted in a limited number of dedicated facilities worldwide.

Another approach is to use fluorescence spectroscopy. Fluorescence microscopy has been used in the past to examine the length of DNA[232] and actin[233] molecules. It was also used to ascertain extension of DNA molecules embedded in an electrospun fiber matrix.[234] Two approaches can be undertaken. A marker fluorescent molecule with known length can be added to the electrospinning solution in very small quantities to ensure spatial separation. The length and extension of the molecule can then be examined post-spinning using fluorescence microscopy. Alternatively, a small quantity (again to ensure spatial separation) of the main electrospinning polymer molecule can be fluorescently labeled. The average distance between the different fluorescent sites needs to be measured prior to electrospinning. This can be accomplished, for example, by examining the labeled molecule stretched in a microfluidic

channel. After spinning, the degree of chain extension can be then estimated by measuring the distance between the fluorescent sites in the NF.

Similar approaches with better, subdiffraction limit resolution, can be undertaken using emerging super resolution microscopy techniques such as Structured Illumination Microscopy (SIM), Simulated Emission Depletion (STED), Stochastic Optical Reconstruction Microscopy (STORM), or Photo Activated Localization Microscopy (PALM). The techniques have already been used to examine spatial arrangement of protein nanofibrils,[235–237] measure the length of stretched DNA segments,[238] and for resolving the distances between adjacent fluorescent sites with spatial resolution unavailable in regular fluorescent microscopy.[239] It is likely that such approaches can be adopted to examine chain extension in electrospun NFs.

In the above techniques only small amount of molecules needs to be fluorescent in order to provide sufficient spatial separation between the fluorescent chains. This would allow simultaneous evaluation of polymer chain alignment and extension. However, it needs to be noted that in both approaches described above (addition of fluorescent marker molecule or labeling a small number of native polymer molecules), changes are made to the fiber-forming solution. In electrospinning nanofabrication process, even small changes in solution parameters can produce significant changes in the resulting NF morphology and structure. Consequently, effects on processing need to be studied and taken into account while interpreting the results of the proposed experiments.

8. Conclusions: Current Status and Prospects

In depth analysis of structure-properties relationships in advanced fibers in the second half of the 20th Century has led to development of fibers with extraordinary strength and modulus. These fibers are now ubiquitous in a myriad of applications from sporting goods to

aerospace structures. Ultrafine nanofibers have recently demonstrated unique ultrahigh *toughness* in addition to high strength and modulus. High toughness is believed to be due to low crystallinity as a result of ultrafast solvent evaporation during the electrospinning process. Crystallization in the thin electrospun jets is retarded by fast solidification, despite high macromolecular alignment in ultrafine-diameter nanofilaments. The degree of polymer chain alignment is therefore the main structural parameter determining nanofibers mechanical and physical properties. Polymer chain orientation in ultrafine NFs is responsible for their high strength and modulus. Chain sliding at large deformations, enabled by low NF crystallinity that is responsible for ultrahigh toughness, is also affected by chain orientation. Quantification of the degree of macromolecular alignment is, therefore, critically needed for better understanding and control of unusual mechanical behavior and size effects in NFs.

If there is any one central message that the authors would like to convey in this review, it is that evaluation of macromolecular chain orientation in fine polymer NFs is a formidable challenge. Many of the traditional techniques can provide valuable information, but all face significant difficulties when applied to ultrafine, sub-250 nanometer diameter NFs (see Table 1 summarizing advantages and limitations of different techniques).

Table 1: Summary of the Techniques Evaluated in this Review

Technique	Type of Sample	Phase Examined	Orientation Information	Comments and Limitations
X-Ray Diffraction (XRD)	Aligned bundles	Crystal phase	Quantitative (arc double angle or orientation function $\langle P_2 \rangle$)	Requires large amount of material; Restricted to crystal orientation analysis
Polarized Fourier Transform Infrared Spectroscopy (FTIR)	Large fibers, aligned bundles	Combined crystal and amorphous phases	System dependent quantitative* (dichroic ratio); quantitative (orientation function $\langle P_2 \rangle$)	For individual fibers likely not applicable below 1 μm; for quantitative analysis requires molecular conformation information; likely to suffer from size-dependent artifacts; modified system dependent quantitative method possible
Differential Scanning Calorimetry (DSC) / Dielectric Relaxation Spectroscopy (DRS)	Fiber mats	Combined crystal and amorphous phases	Qualitative (shift in glass transition, changes in temperature fluctuation for α relaxation)	Requires large amount of material; complicated interpretation; for quantitative information would require complicated calibration

Solid State Nuclear Magnetic Resonance (SSNMR)	Large aligned bundles	Separate orientation information on crystal and amorphous phases	System dependent quantitative (changes in the chemical shift), quantitative (orientation function $\langle P_2 \rangle$)	Requires very large amounts of material and long scan times; for proper interpretation requires large number of experiments for calibration
Selected Area Electron Diffraction (SAED)	Small diameter individual fibers or thin fiber slices	Crystal phase	Quantitative (arc double angle or orientation function $\langle P_2 \rangle$)	Restricted to the crystal phase; unknown radiation damage; for large fibers requires complicated sample preparation
Polarized Optical Microscopy	Large individual fibers	Combined crystal and amorphous phases	System dependent quantitative (birefringence); quantitative (orientation function $\langle P_2 \rangle$)	Likely to face sensitivity issues for smaller fibers; for quantitative information requires information on intrinsic birefringence; likely to suffer from size-dependent artifacts
Polarization-Modulation (PM) Microscopy	Large individual fibers	Combined crystal and amorphous phases	System dependent quantitative (dichroism/differential absorption)	Likely to face sensitivity issues for smaller fibers; likely to suffer from size-dependent artifacts

Polarized Raman Spectroscopy	Individual fibers	Combined crystal and amorphous phases	System dependent quantitative (1-I_{VV}/I_{HH}); quantitative (orientation functions $\langle P_2 \rangle$ and $\langle P_4 \rangle$); system dependent quantitative modified method (intensity ratio between two bands)	Quantitative method requires assumptions and multiple spectra acquisition; traditional system dependent quantitative and comprehensive quantitative analyses suffer from size dependent artifacts; correction for effects of crystallinity are needed in the modified method
Atomic Force Microscopy (AFM)	Individual fibers	Combined crystal and amorphous phases	Qualitative (anisotropy in topography and mechanical properties); however, single molecule resolution is theoretically possible	Surface technique; For internal orientation requires complicated sample preparation and data interpretation models
Micro- and Nano-focused X-Ray Microscopy	Small aligned bundles; potentially individual fibers	Separate orientation information on crystal and amorphous phases	Quantitative	Applicability to electrospun NFs not tested yet; requires advanced light sources (synchrotron)

Fast Scanning Calorimetry (FSC)	Small bundles or mats; potentially individual fibers	Combined crystal and amorphous phases	Qualitative (shift in glass transition, changes in temperature fluctuation for α relaxation)	Applicability to electrospun NFs have not been demonstrated yet; complicated interpretation; for quantitative information would require complicated calibration
Aperture Near-field Scanning Optical Microscopy (*a*-NSOM)	Individual fibers	Combined crystal and amorphous phases	System dependent quantitative (birefringence, dichroism/differential absorption); quantitative (orientation function $\langle P_2 \rangle$)	For quantitative information requires information on intrinsic birefringence; likely to suffer from size-dependent artifacts; needs information on local crystallinity and crystal structure
Tip-Enhanced Raman Spectroscopy (TERS)	Individual fibers	Combined crystal and amorphous phases	To be determined	Applicability for orientation studies not yet demonstrated
Photothermal Induced Resonance (PTIR)	Individual fibers	Combined crystal and amorphous phases	System dependent quantitative (dichroic ratio); quantitative (orientation function $\langle P_2 \rangle$)	Likely to face sensitivity issues for smaller fibers; for quantitative analysis requires molecular conformation information; likely to suffer from size-dependent artifacts

				modified system dependent quantitative method possible; for a modified method would require local crystallinity information and correction
Nano-FTIR	Individual fibers	Combined crystal and amorphous phases	System dependent quantitative (intensity ratio between two bands)	Needs information on local crystallinity and correction for crystallinity effects

*"System dependent quantitative" refers to orientation indicators that can be used for quantitative comparative studies, but is not a traditional orientation function, and thus is polymer system specific and depends on parameters chosen for that particular system.

Techniques such as XRD and SAED that examine the crystalline phase of the polymer, are limited in their utility due to low NF crystallinity. Results from techniques that need large amounts of material such as XRD, FTIR, DSC/DRS, and NMR are further confounded by the inherent and often severe misalignment and polydispersity of NF samples produced by the instabilities-driven nanofabrication process. Sample inhomogeneity usually increases with reduction of average NF diameter. Additionally, low viscosities, required to achieve ultrafine diameters, can lead to beading detrimental to structural evaluation in NF bundles. Consequently, the techniques relying on NF interrogation of bundles are currently providing only qualitative information when applied to ultrafine NFs. Such information is useful for qualitative evaluation of trends and visualization. It can provide complementary information for comparative studies of different nanofiber systems. Averaged information on bundles is also valuable for applications utilizing exact same bundles or other nanofiber assemblies with similar NF polydispersity. However, in-depth fundamental studies and nanofiber properties optimization would generally require higher accuracy. Better sample preparation techniques, such as the ones described in Section 6, can significantly improve the outcomes for the bundle-based methods and elevate them to the quantitative level.

Currently, techniques interrogating individual NFs are preferred for structural size effects studies in the ultrafine NF diameter range. Note, however, that all relevant spectroscopic techniques that rely on measuring light intensities under different polarizations face a variety of instrumental and inherent light-sample interaction-related artifacts due to high curvature of NFs with subwavelength diameters. Such artifacts, discussed in detail on a polarized Raman microscopy example, were shown to lead to quantitatively and even qualitatively erroneous results. Some of these artifacts can also appear in examination of NF bundles when a switch in

polarization is needed (*e.g.*, in using polarized FTIR – see Section 2.2). Further carefully designed studies are needed to better understand and avoid these artifacts.

A modified polarized Raman technique described in Section 4 emerges as a relatively simple option suitable for quick comparative orientation studies. It is inexpensive, relatively fast, uses widely available instrumentation, and is able to examine individual NFs. The technique was implemented for both amorphous and low-crystalline polymer systems. It was demonstrated to produce quantitative information that can be used to distinguish structural size effects in NFs produced using different nanofabrication parameters. The latter opens up possibilities for more detailed processing-structure-properties analyses that can lead to accelerated research and development of supertough strong continuous nanofibers. We expect that the artifact-free approach recently developed and demonstrated by the co-authors of this study for Raman spectroscopy (*i.e.* analysis of multiple bands with different orientation under single light polarization) should be applicable to other spectroscopic techniques discussed in the review. It can be used to avoid errors due to light interaction with subwavelength-diameter (ultrafine) NF samples with high curvature.

Several emerging techniques discussed in Section 5 show high potential for orientational studies on individual nanofibers or small bundles. However, their ability to reliably quantify polymer chain orientation in ultrafine electrospun NFs is yet to be demonstrated. Several anticipated problems, described in this review, need to be further analyzed and addressed.

Fast solvent evaporation in electrospinning can create metastable phases and unusual crystal phase mixes in some polymer systems. The content as well as orientation of these phases can vary with nanofiber diameters. Further studies are needed for quantification of macromolecular alignment and structural size effects in these more complex systems.

Currently, no single technique can provide comprehensive evaluation of orientation in ultrafine low-crystalline NFs. Techniques described in this review should be used with the appropriate caution, and several techniques should be employed to both provide complementary information and to cross reference the results for possible artifacts.

Reliable quantification of polymer chain alignment in ultrafine electrospun NFs will lead to better understanding of structural mechanisms behind their unique property combinations and will significantly accelerate property optimization. Development of simultaneously ultratough and strong continuous nanofibers can revolutionize structural nanomaterials research and lead to next generation bulk nanostructured materials and nanocomposites for safety-critical applications.

Acknowledgements: This work was supported in part by the grants from ONR (N000141410663), NSF (DMR-1310534, CMMI-1463636), and NIH (1R01HL125736-01). CP acknowledges the support from the Natural Sciences and Engineering Council of Canada. MH acknowledges the support of the Center for Nanoscale Materials, a U.S. Department of Energy Office of Science User Facility under Contract No. DE-AC02-06CH11357. The authors thank Bruce Chase of University of Delaware, Dmitri Basov of Columbia University, Alan D. English of *Macromolecules* journal, and Martha Morton of University of Nebraska-Lincoln for reading sections of this work and valuable comments; Tobias Gokus and Nicolai Hartmann from *neaspec GmbH* for their help with nano-FTIR measurements; and Joel Brehm of UNL for his help with creating graphical schematics for this paper.

SUPPORTING INFORMATION AVAILABLE: (1) Orientation studies in nanofibers; (2) Orientation evaluation using FTIR; (3) Experimental details for DSC and DRS tests; (4) SSNMR examination of PAN powder; (5) Orientation evaluation using polarized light microscopy; (6) Schematic of the optical path in Polarized Raman studies; (7) Comprehensive Orientation Evaluation using Polarized Raman Spectroscopy; (8) Explanation of different wave-plate operation; (9) Schematic of the effect of fiber movement on laser intensity that produces the Raman signal for different NF diameters; (10) Schematic of the difference between objectives with small and large numerical aperture; (11) Typical XRD patterns for PAN film and electrospun mat.This material is available free of charge *via* the Internet at http://pubs.acs.org.

References

(1) Dzenis, Y. A. Structural Nanocomposites. *Science (80-.).* **2008**, *319* (5862), 419–420.

(2) Ritchie, R. O.; Dzenis, Y. A. The Quest for Stronger , Tougher Materials : A Letter and a Response. *Science (80-.).* **2008**, *320* (5875), 448.

(3) Papkov, D.; Beese, A. M.; Goponenko, A.; Zou, Y.; Naraghi, M.; Espinosa, H. D.; Saha, B.; Schatz, G. C.; Moravsky, A.; Loutfy, R.; et al. Extraordinary Improvement of the Graphitic Structure of Continuous Carbon Nanofibers Templated with Double Wall Carbon Nanotubes. *ACS Nano* **2013**, *7* (1), 126–142.

(4) Papkov, D.; Goponenko, A.; Compton, O. C.; An, Z.; Moravsky, A.; Li, X.-Z.; Nguyen, S. T.; Dzenis, Y. A. Improved Graphitic Structure of Continuous Carbon Nanofibers via Graphene Oxide Templating. *Adv. Funct. Mater.* **2013**, *23*, 5763–5770.

(5) Reneker, D. H.; Chun, I. Nanometre Diameter Fibres of Polymer, Produced by Electrospinning. *Nanotechnology* **1996**, *7* (3), 216–223.

(6) Dzenis, Y. A. Spinning Continuous Fibers for Nanotechnology. *Science (80-.).* **2004**, *304* (5679), 1917–1919.

(7) Lannutti, J.; Reneker, D.; Ma, T.; Tomasko, D.; Farson, D. Electrospinning for Tissue Engineering Scaffolds. *Mater. Sci. Eng. C* **2007**, *27* (3), 504–509.

(8) Sill, T. J.; von Recum, H. A. Electrospinning: Applications in Drug Delivery and Tissue Engineering. *Biomaterials* **2008**, *29* (13), 1989–2006.

(9) Cho, H.; Min, S.-Y.; Lee, T.-W. Electrospun Organic Nanofiber Electronics and Photonics. *Macromol. Mater. Eng.* **2013**, *298* (5), 475–486.

(10) Camposeo, A.; Di Benedetto, F.; Stabile, R.; Neves, A. a R.; Cingolani, R.; Pisignano, D.

Laser Emission from Electrospun Polymer Nanofibers. *Small* **2009**, *5* (5), 562–566.

(11) Sun, B.; Long, Y.-Z.; Chen, Z.-J.; Liu, S.-L.; Zhang, H.-D.; Zhang, J.-C.; Han, W.-P.; Zhang, M.; Mai, Y. W.; Wang, N. H.; et al. Recent Advances in Flexible and Stretchable Electronic Devices via Electrospinning. *J. Mater. Chem. C* **2014**, *2* (7), 1209–1219.

(12) Papkov, D.; Zou, Y.; Andalib, M. N.; Goponenko, A.; Cheng, S. Z. D.; Dzenis, Y. A. Simultaneously Strong and Tough Ultrafine Continuous Nanofibers. *ACS Nano* **2013**, *7* (4), 3324–3331.

(13) Ritchie, R. O. The Conflicts between Strength and Toughness. *Nat. Mater.* **2011**, *10* (11), 817–822.

(14) Fennessey, S. F.; Farris, R. J. Fabrication of Aligned and Molecularly Oriented Electrospun Polyacrylonitrile Nanofibers and the Mechanical Behavior of Their Twisted Yarns. *Polymer (Guildf).* **2004**, *45* (12), 4217–4225.

(15) Naraghi, M.; Arshad, S. N.; Chasiotis, I. Molecular Orientation and Mechanical Property Size Effects in Electrospun Polyacrylonitrile Nanofibers. *Polymer (Guildf).* **2011**, *52* (7), 1612–1618.

(16) Dersch, R.; Liu, T.; Schaper, A. K.; Greiner, A.; Wendorff, J. H. Electrospun Nanofibers: Internal Structure and Intrinsic Orientation. *J. Polym. Sci. Part A Polym. Chem.* **2003**, *41* (4), 545–553.

(17) Maleckis, K.; Dzenis, Y. Continuous DNA Nanofibers with Extraordinary Mechanical Properties and High Molecular Orientation. **2018**, *1800302*, 1–8.

(18) Tosaka, M.; Yamaguchi, K.; Tsuji, M. Latent Orientation in the Skin Layer of Electrospun Isotactic Polystyrene Ultrafine Fibers. *Polymer (Guildf).* **2010**, *51* (2), 547–553.

(19) Richard-Lacroix, M.; Pellerin, C. Orientation and Structure of Single Electrospun Nanofibers of Poly(Ethylene Terephthalate) by Confocal Raman Spectroscopy. *Macromolecules* **2012**, *45* (4), 1946–1953.

(20) *High-Performance Structural Fibers for Advanced Polymer Matrix Composites*; National Academies Press: Washington, D.C., 2005.

(21) Hou, H.; Ge, J. J.; Zeng, J.; Li, Q.; Reneker, D. H.; Greiner, A.; Cheng, S. Z. D. Electrospun Polyacrylonitrile Nanofibers Containing a High Concentration of Well-Aligned Multiwall Carbon Nanotubes. *Chem. Mater.* **2005**, *17* (5), 967–973.

(22) Bunsell, R. A. *Fibre Reinforcements for Composite Materials*; Pipes, B. R., Ed.; Composite Materials; Elsevier: New York, 1988; Vol. 2.

(23) Naraghi, M.; Filleter, T.; Moravsky, A.; Locascio, M.; Loutfy, R. O.; Espinosa, H. D. A Multiscale Study of High Performance Double-Walled Nanotube−Polymer Fibers. *ACS Nano* **2010**, *4* (11), 6463–6476.

(24) Zhang, M.; Atkinson, K. R.; Baughman, R. H. Multifunctional Carbon Nanotube Yarns by Downsizing an Ancient Technology. *Science* **2004**, *306* (5700), 1358–1361.

(25) Motta, M.; Moisala, A.; Kinloch, I. A.; Windle, A. H. High Performance Fibres from "Dog Bone" Carbon Nanotubes. *Adv. Mater.* **2007**, *19* (21), 3721–3726.

(26) Miaudet, P.; Badaire, S.; Maugey, M.; Derré, A.; Pichot, V.; Launois, P.; Poulin, P.; Zakri, C.; Derre, A. Hot-Drawing of Single and Multiwall Carbon Nanotube Fibers for High

Toughness and Alignment. *Nano Lett.* **2005**, *5* (11), 2212–2215.

(27) Wu, X.-F.; Salkovskiy, Y.; Dzenis, Y. A. Modeling of Solvent Evaporation from Polymer Jets in Electrospinning. *Appl. Phys. Lett.* **2011**, *98* (22), 223108.

(28) Charch, W. H.; Moseley, W. W. Structure-Property Relationships in Synthetic Fibers. *Text. Res. J.* **1959**, *29* (7), 525–535.

(29) Watt, W.; Phillips, L. N.; Johnson, W. High-Modulus, High Strength Carbon Fibers. *Eng. 221*, 815.

(30) Bastiaansen, C. W. M. Tensile Strength of Solution-Spun, Ultra-Drawn Ultra-High Molecular Weight Polyethylene Fibres: 1. Influence of Fibre Diameter. *Polymer (Guildf).* **1992**, *33* (8), 1649–1652.

(31) Richard-Lacroix, M.; Pellerin, C. Molecular Orientation in Electrospun Fibers: From Mats to Single Fibers. *Macromolecules* **2013**, *46* (24), 9473–9493.

(32) Kakade, M. V; Givens, S.; Gardner, K.; Lee, K. H.; Chase, D. B.; Rabolt, J. F. Electric Field Induced Orientation of Polymer Chains in Macroscopically Aligned Electrospun Polymer Nanofibers. *J. Am. Chem. Soc.* **2007**, *129* (10), 2777–2782.

(33) Kongkhlang, T.; Tashiro, K.; Kotaki, M.; Chirachanchai, S. Electrospinning as a New Technique To Control the Crystal Morphology and Molecular Orientation of Polyoxymethylene Nanofibers. *J. Am. Chem. Soc.* **2008**, *130* (46), 15460–15466.

(34) Arinstein, A.; Burman, M.; Gendelman, O.; Zussman, E. Effect of Supramolecular Structure on Polymer Nanofibre Elasticity. *Nat Nano* **2007**, *2* (1), 59–62.

(35) Chen, W.; Tao, X.; Liu, Y. Carbon Nanotube-Reinforced Polyurethane Composite Fibers. *Compos. Sci. Technol.* **2006**, *66* (15), 3029–3034.

(36) Morgan, P. *Carbon Fibers and Their Composites*; Carbon Fibers and Their Composites; CRC Press, Taylor & Francis Group, LLC: Boka Raton, FL, 2005.

(37) Ward, I. M.; Coates, P. D.; Dumoulin, M. M. *Solid Phase Processing of Polymers*; Hanser Publishers, 2000.

(38) Jasse, B.; Koenig, J. L. *Orientational Measurements in Polymers Using Vibrational Spectroscopy*; 1979; Vol. 17.

(39) Bashir, Z.; Tipping, A. R.; Church, S. P. Orientation Studies in Polyacrylonitrile Films Uniaxially Drawn in the Solid State. *Polym. Int.* **1994**, *33* (1), 9–17.

(40) Chan, K. H. K.; Wong, S. Y.; Li, X.; Zhang, Y. Z.; Lim, P. C.; Lim, C. T.; Kotaki, M.; He, C. Bin. Effect of Molecular Orientation on Mechanical Property of Single Electrospun Fiber of Poly[(R)-3-Hydroxybutyrate-Co-(R)-3-Hydroxyvalerate]. *J. Phys. Chem. B* **2009**, *113* (40), 13179–13185.

(41) Griffiths, P. R.; De Haseth, J. A. *Fourier Transform Infrared Spectrometry*; Wiley-Interscience, 2007.

(42) Ma, X.; Zachariah, M. R.; Zangmeister, C. D. Crumpled Nanopaper from Graphene Oxide. *Nano Lett.* **2012**, *12* (1), 486–489.

(43) Cheng, Y.-W.; Lu, H.-A.; Wang, Y.-C.; Thierry, A.; Lotz, B.; Wang, C. Syndiotactic Polystyrene Nanofibers Obtained from High-Temperature Solution Electrospinning

Process. *Macromolecules* **2010**, *43* (5), 2371–2376.

(44) Tu, D.; Pagliara, S.; Camposeo, A.; Persano, L.; Cingolani, R.; Pisignano, D. Single Light-Emitting Polymer Nanofiber Field-Effect Transistors. *Nanoscale* **2010**, *2* (10), 2217–2222.

(45) Koenig, J. L. *Spectroscopy of Polymers*, 2nd ed.; Elsevier, 1999.

(46) Henrici-Olivé, G.; Olivé, S. Molecular Interactions and Macroscopic Properties of Polyacrylonitrile and Model Substances. In *Chemistry. Advances in Polymer Science*; Advances in Polymer Science; Springer Berlin Heidelberg, 1979; Vol. 32, pp 123–152.

(47) Litovchenko, G. D. Infrared Dichroism of the Band of Valence Vibrations of the C≡N Bonds in Polyacrylonitrile Fibers. *J. Appl. Spectrosc.* **1973**, *18* (6), 781–783.

(48) Gu, S.; Wu, Q.; Ren, J.; Vancso, G. J. Mechanical Properties of a Single Electrospun Fiber and Its Structures. **2005**, *1*, 716–720.

(49) Pagliara, S.; Vitiello, M. S.; Camposeo, A.; Polini, A.; Cingolani, R.; Scamarcio, G.; Pisignano, D. Optical Anisotropy in Single Light-Emitting Polymer Nanofibers. *J. Phys. Chem. C* **2011**, *115* (42), 20399–20405.

(50) Gong, L.; Chase, D. B.; Noda, I.; Liu, J.; Martin, D. C.; Ni, C.; Rabolt, J. F. Discovery of β-Form Crystal Structure in Electrospun Poly[(R)-3-Hydroxybutyrate-Co-(R)-3-Hydroxyhexanoate] (PHBHx) Nanofibers: From Fiber Mats to Single Fibers. *Macromolecules* **2015**, *48* (17), 6197–6205.

(51) Behabtu, N.; Young, C. C.; Tsentalovich, D. E.; Kleinerman, O.; Wang, X.; Ma, A. W. K.; Bengio, E. A.; ter Waarbeek, R. F.; de Jong, J. J.; Hoogerwerf, R. E.; et al. Strong, Light, Multifunctional Fibers of Carbon Nanotubes with Ultrahigh Conductivity. *Science* **2013**, *339* (6116), 182–186.

(52) Wang, C.; Chien, H.-S.; Yan, K.-W.; Hung, C.-L.; Hung, K.-L.; Tsai, S.-J.; Jhang, H.-J. Correlation between Processing Parameters and Microstructure of Electrospun Poly(D,l-Lactic Acid) Nanofibers. *Polymer (Guildf).* **2009**, *50* (25), 6100–6110.

(53) Isakov, D. V.; de Matos Gomes, E.; Vieira, L. G.; Dekola, T.; Belsley, M. S.; Almeida, B. G. Oriented Single-Crystal-like Molecular Arrangement of Optically Nonlinear 2-Methyl-4-Nitroaniline in Electrospun Nanofibers. *ACS Nano* **2011**, *5* (1), 73–78.

(54) Bashir, Z.; Church, S. P.; Price, D. M. The Formation of Polymer-Solvent Complexes of Polyacrylonitrile from Organic Solvents Containing Carbonyl Groups. *Acta Polym.* **1993**, *44* (5), 211–218.

(55) Miller, R. W.; Murayama, T. Dynamic Mechanical Properties of Partially Oriented Polyester (POY) and Draw-Textured Polyester (PTY) Yarns. *J. Appl. Polym. Sci.* **1984**, *29* (3), 933–939.

(56) Furushima, Y.; Ishikiriyama, K.; Higashioji, T. The Characteristic Length of Cooperative Rearranging Region for Uniaxial Drawn Poly(Ethylene Terephthalate) Films. *Polymer (Guildf).* **2013**, *54* (16), 4078–4084.

(57) Delpouve, N.; Delbreilh, L.; Stoclet, G.; Saiter, A.; Dargent, E. Structural Dependence of the Molecular Mobility in the Amorphous Fractions of Polylactide. *Macromolecules* **2014**, *47* (15), 5186–5197.

(58) Delpouve, N.; Lixon, C.; Saiter, A.; Dargent, E.; Grenet, J. Amorphous Phase Dynamics at the Glass Transition in Drawn Semi-Crystalline Polyester. *J. Therm. Anal. Calorim.* **2009**, *97* (2), 541–546.

(59) Hamonic, F.; Miri, V.; Saiter, A.; Dargent, E. Rigid Amorphous Fraction versus Oriented Amorphous Fraction in Uniaxially Drawn Polyesters. *Eur. Polym. J.* **2014**, *58*, 233–244.

(60) Wang, C.; Lee, M.-F.; Jao, C.-H. Phase Transition of Poly(Ethylene Terephthalate) in Nanofibers Electrospun from Phenol-Based Solution. *Eur. Polym. J.* **2014**, *52*, 127–136.

(61) Chen, H.; Liu, Z.; Cebe, P. Chain Confinement in Electrospun Nanofibers of PET with Carbon Nanotubes. *Polymer (Guildf).* **2009**, *50* (3), 872–880.

(62) Ma, Q.; Pyda, M.; Mao, B.; Cebe, P. Relationship between the Rigid Amorphous Phase and Mesophase in Electrospun Fibers. *Polym. (United Kingdom)* **2013**, *54* (10), 2544–2554.

(63) Monnier, X.; Delpouve, N.; Basson, N.; Guinault, A.; Domenek, S.; Saiter, A.; Mallon, P. E.; Dargent, E. Molecular Dynamics in Electrospun Amorphous Plasticized Polylactide Fibers. *Polymer (Guildf).* **2015**, *73*, 68–78.

(64) Zhang, P.; Tian, R.; Na, B.; Lv, R.; Liu, Q. Intermolecular Ordering as the Precursor for Stereocomplex Formation in the Electrospun Polylactide Fibers. *Polymer (Guildf).* **2015**, *60*, 221–227.

(65) Li, K.; Mao, B.; Cebe, P. Electrospun Fibers of Poly(Ethylene Terephthalate) Blended with Poly(Lactic Acid). *J. Therm. Anal. Calorim.* **2014**, *116* (3), 1351–1359.

(66) Lv, R.; Na, B.; Tian, N.; Zou, S.; Li, Z.; Jiang, S. Mesophase Formation and Its Thermal Transition in the Stretched Glassy Polylactide Revealed by Infrared Spectroscopy. *Polymer (Guildf).* **2011**, *52* (21), 4979–4984.

(67) Ma, Q.; Mao, B.; Cebe, P. Chain Confinement in Electrospun Nanocomposites: Using Thermal Analysis to Investigate Polymer–filler Interactions. *Polymer (Guildf).* **2011**, *52* (14), 3190–3200.

(68) Mao, B.; Geers, K.; Hu, S.; Mancera, M.; Sandoval, M.; Port, J.; Zhu, Y.; Cebe, P. Properties of Aligned Poly(L-Lactic Acid) Electrospun Fibers. *J. Appl. Polym. Sci.* **2015**, *132* (14), n/a-n/a.

(69) Zong, X. H.; Kim, K.; Fang, D.; Ran, S.; Hsiao, B. S.; Chu, B.; Hsiao, S. H. Structure and Process Relationship of Electrospun Bioabsorbable Nanofiber Membranes. *Polymer (Guildf).* **2002**, *43* (16), 4403–4412.

(70) Adam, G.; Gibbs, J. H. On the Temperature Dependence of Cooperative Relaxation Properties in Glass-Forming Liquids. *J. Chem. Phys.* **1965**, *43* (1), 139–146.

(71) Donth, E. The Size of Cooperatively Rearranging Regions at the Glass Transition. *J. Non. Cryst. Solids* **1982**, *53* (3), 325–330.

(72) Hamonic, F.; Prevosto, D.; Dargent, E.; Saiter, A. Contribution of Chain Alignment and Crystallization in the Evolution of Cooperativity in Drawn Polymers. *Polymer (Guildf).* **2014**, *55* (12), 2882–2889.

(73) Lixon, C.; Delpouve, N.; Saiter, A.; Dargent, E.; Grohens, Y. Evidence of Cooperative Rearranging Region Size Anisotropy for Drawn PET. *Eur. Polym. J.* **2008**, *44* (11), 3377–

3384.

(74) Hamonic, F.; Saiter, A.; Dargent, E. Evidence of Cooperativity Length Anisotropy in Drawn Polymers. *Mater. Lett.* **2014**, *128*, 12–14.

(75) Kremer, F.; Schönhals, A. (Andreas). *Broadband Dielectric Spectroscopy*; Springer Berlin Heidelberg, 2003.

(76) Esposito, A.; Delpouve, N.; Causin, V.; Dhotel, A.; Delbreilh, L.; Dargent, E. From a Three-Phase Model to a Continuous Description of Molecular Mobility in Semicrystalline Poly(Hydroxybutyrate- *Co* -Hydroxyvalerate). *Macromolecules* **2016**, *49* (13), 4850–4861.

(77) Tahalyani, J.; Datar, S.; Balasubramanian, K. Investigation of Dielectric Properties of Free Standing Electrospun Nonwoven Mat. *J. Appl. Polym. Sci.* **2018**, *135* (16), 46121.

(78) Santos, J. P. F.; da Silva, A. B.; Arjmand, M.; Sundararaj, U.; Bretas, R. E. S. Nanofibers of Poly(Vinylidene Fluoride)/Copper Nanowire: Microstructural Analysis and Dielectric Behavior. *Eur. Polym. J.* **2018**, *101*, 46–55.

(79) Tahalyani, J.; Rahangdale, K. K.; Aepuru, R.; Kandasubramanian, B.; Datar, S. Dielectric Investigation of a Conducting Fibrous Nonwoven Porous Mat Fabricated by a One-Step Facile Electrospinning Process. *RSC Adv.* **2016**, *6* (43), 36588–36598.

(80) Dhotel, A.; Rijal, B.; Delbreilh, L.; Dargent, E.; Saiter, A. Combining Flash DSC, DSC and Broadband Dielectric Spectroscopy to Determine Fragility. *J. Therm. Anal. Calorim.* **2015**, *121* (1), 453–461.

(81) Komorski, R. A. *High Resolution NMR Spectroscopy of Synthetic Polymers in Bulk*; Komorski, R. A., Ed.; VCH Publishers Inc., Deerfield Bch, FL, 1986.

(82) Ando, I. (Isao); Asakura, T. *Solid State NMR of Polymers*; Elsevier, 1998.

(83) Guo, W.; Fung, B. M. Determination of the Order Parameters of Liquid Crystals from Carbon-13 Chemical Shifts. *J. Chem. Phys.* **1991**, *95* (6), 3917–3923.

(84) Wei, Y.; Lee, D.-K.; Ramamoorthy, A. Solid-State ^{13}C NMR Chemical Shift Anisotropy Tensors of Polypeptides. *J. Am. Chem. Soc.* **2001**, *123* (25), 6118–6126.

(85) Henrichs, P. M. Molecular Orientation and Structure in Solid Polymers with 13C NMR: A Study of Biaxial Films of Poly(Ethylene Terephthalate). *Macromolecules* **1987**, *20* (9), 2099–2112.

(86) Asakura, T.; Yeo, J. H.; Demura, M.; Itoh, T.; Fujito, T.; Imanari, M.; Nicholson, L. K.; Cross, T. A. Structural Analysis of Uniaxially Aligned Polymers Using Solid-State Nitrogen-15 NMR. *Macromolecules* **1993**, *26* (24), 6660–6663.

(87) Yeo, J.-H.; Demura, M.; Asakura, T.; Fujito, T.; Imanari, M.; Nicholson, L. K.; Cross, T. A. Structural Analysis of Highly Oriented Poly(p-Phenylene-Terephthalamide) by 15N Solid-State Nuclear Magnetic Resonance. *Solid State Nucl. Magn. Reson.* **1994**, *3* (4), 209–218.

(88) Asakura, T.; Yeo, J.-H.; Ando, I. Structure of Polyamide Fibers in the Non-Crystalline Domain Studied by 15N Solid State NMR. *Polym. J.* **1994**, *26* (2), 229–233.

(89) Brandolini, A. J.; Alvey, M. D.; Dybowski, C. The Crystallite Orientation Distribution Functions of Deformed Polytetrafluoroethylene: Multiple-Pulse 19F NMR Spectroscopy.

J. Polym. Sci. Polym. Phys. Ed. **1983**, *21* (12), 2511–2524.

(90) Saito, H.; Ando, I. High-Resolution Solid-State NMR Studies of Synthetic and Biological Macromolecules. *Annu. Reports NMR Spectrosc.* **1989**, *21*, 209–290.

(91) Falk, U.; Spiess, H. W. Phase Behaviour and Macroscopic Alignment of Rigid Chain Polyesters with Short Flexible Side Chains. *Die Makromol. Chemie, Rapid Commun.* **1989**, *10* (4), 149–155.

(92) Hentschel, R.; Sillescu, H.; Spiess, H. W. Orientational Distribution of Polymer Chains Studied by 2H n.m.r. Line Shapes. *Polymer (Guildf).* **1981**, *22* (11), 1516–1521.

(93) Yeo, J.-H.; Demura, M.; Asakura, T.; Fujito, T.; Imanari, M.; Nicholson, L. K.; Cross, T. A. Structural Analysis of Highly Oriented Poly(p-Phenylene-Terephthalamide) by 15N Solid-State Nuclear Magnetic Resonance. *Solid State Nucl. Magn. Reson.* **1994**, *3* (4), 209–218.

(94) van Beek, J. D.; Hess, S.; Vollrath, F.; Meier, B. H. The Molecular Structure of Spider Dragline Silk: Folding and Orientation of the Protein Backbone. *Proc. Natl. Acad. Sci.* **2002**, *99* (16), 10266–10271.

(95) Asakura, T.; Ashida, J.; Yamane, T.; Kameda, T.; Nakazawa, Y.; Ohgo, K.; Komatsu, K. A Repeated β-Turn Structure in Poly(Ala-Gly) as a Model for Silk I of Bombyx Mori Silk Fibroin Studied with Two-Dimensional Spin-Diffusion NMR under off Magic Angle Spinning and Rotational Echo Double Resonance. *J. Mol. Biol.* **2001**, *306* (2), 291–305.

(96) Hyun Kim, S.; Sik Nam, Y.; Seung Lee, T.; Ho Park, W. Silk Fibroin Nanofiber. Electrospinning, Properties, and Structure. *Polym. J.* **2003**, *35* (2), 185–190.

(97) Mote, K. R.; Agarwal, V.; Madhu, P. K. Five Decades of Homonuclear Dipolar Decoupling in Solid-State NMR: Status and Outlook. *Prog. Nucl. Magn. Reson. Spectrosc.* **2016**, *97*, 1–39.

(98) Mithu, V. S.; Pratihar, S.; Paul, S.; Madhu, P. K. Efficiency of Heteronuclear Dipolar Decoupling Schemes in Solid-State NMR: Investigation of Effective Transverse Relaxation Times. *J. Magn. Reson.* **2012**, *220*, 8–17.

(99) Kovacs, H.; Moskau, D.; Spraul, M. Cryogenically Cooled Probes-a Leap in NMR Technology. *Prog. Nucl. Magn. Reson. Spectrosc.* **2005**, *46* (2–3), 131–155.

(100) Matsuzaki, K.; Uryu, T.; Ishigure, K.; Takeuchi, M. NMR Spectra of Polyacrylonitriles. *J. Polym. Sci. Part B Polym. Lett.* **1966**, *4* (2), 93–96.

(101) Hong, M. Oligomeric Structure, Dynamics, and Orientation of Membrane Proteins from Solid-State NMR. *Structure* **2006**, *14* (12), 1731–1740.

(102) Wang, Y.; Xu, L.; Wang, M.; Pang, W.; Ge, X. Structural Identification of Polyacrylonitrile during Thermal Treatment by Selective ^{13}C Labeling and Solid-State ^{13}C NMR Spectroscopy. *Macromolecules* **2014**, *47* (12), 3901–3908.

(103) Fong, H.; Chun, I.; Reneker, D. H. Beaded Nanofibers Formed during Electrospinning. *Polymer (Guildf).* **1999**, *40* (16), 4585–4592.

(104) Richard-Lacroix, M.; Pellerin, C. Orientation and Partial Disentanglement in Individual Electrospun Fibers: Diameter Dependence and Correlation with Mechanical Properties. *Macromolecules* **2015**, *48* (13), 4511–4519.

(105) Papkov, D.; Beese, A. M.; Goponenko, A.; Zou, Y.; Naraghi, M.; Espinosa, H. D.; Saha, B.; Schatz, G. C.; Moravsky, A.; Loutfy, R.; et al. Extraordinary Improvement of the Graphitic Structure of Continuous Carbon Nanofibers Emplated with Double Wall Carbon Nanotubes. *ACS Nano* **2013**, *7* (1), 126–142.

(106) Yoshioka, T.; Dersch, R.; Tsuji, M.; Schaper, A. K. Orientation Analysis of Individual Electrospun PE Nanofibers by Transmission Electron Microscopy. *Polymer (Guildf).* **2010**, *51* (11), 2383–2389.

(107) Ma, X.; Liu, J.; Ni, C.; Martin, D. C.; Chase, D. B.; Rabolt, J. F. Molecular Orientation in Electrospun Poly(Vinylidene Fluoride) Fibers. *ACS Macro Lett.* **2012**, *1* (3), 428–431.

(108) Davidson, J. A.; Jung, H.-T.; Hudson, S. D.; Percec, S. Investigation of Molecular Orientation in Melt-Spun High Acrylonitrile Fibers. *Polymer (Guildf).* **2000**, *41* (9), 3357–3364.

(109) Drake, A. F. *Polarisation Modulation-the Measurement of Linear and Circular Dichroism*; 1986; Vol. 19.

(110) Lewis, I. R.; Edwards, H. *Handbook of Raman Spectroscopy: From the Research Laboratory to the Process Line*; CRC Press, 2001.

(111) Singamaneni, S.; Bertoldi, K.; Chang, S.; Jang, J.-H.; Young, S. L.; Thomas, E. L.; Boyce, M. C.; Tsukruk, V. V. Bifurcated Mechanical Behavior of Deformed Periodic Porous Solids. *Adv. Funct. Mater.* **2009**, *19* (9), 1426–1436.

(112) Kattumenu, R.; Lee, C. H.; Bliznyuk, V. N.; Singamaneni, S. Micro-Raman Spectroscopy of Nanostructures. In *Raman Spectroscopy for Nanomaterials Characterization*; Springer Berlin Heidelberg: Berlin, Heidelberg, 2012; pp 417–444.

(113) Bower, D. I. Investigation of Molecular Orientation Distributions by Polarized Raman Scattering and Polarized Fluorescence. *J. Polym. Sci. Polym. Phys. Ed.* **1972**, *10* (11), 2135–2153.

(114) Bower, D. I. Raman Scattering from an Assembly of Partially Oriented Scatterers. *J. Phys. B At. Mol. Phys.* **1976**, *9* (18), 3275.

(115) Frisk, S.; Ikeda, R. M.; Chase, D. B.; Rabolt, J. F. Determination of the Molecular Orientation of Poly(Propylene Terephthalate) Fibers Using Polarized Raman Spectroscopy: A Comparison of Methods. *Appl. Spectrosc.* **2004**, *58* (3), 279–286.

(116) Purvis, J.; Bower, D. I. Molecular Orientation in Poly(Ethylene Terephthalate) by Means of Laser–raman Spectroscopy. *J. Polym. Sci. Polym. Phys. Ed.* **1976**, *14* (8), 1461–1484.

(117) Richard-Lacroix, M.; Pellerin, C. Accurate New Method for Molecular Orientation Quantification Using Polarized Raman Spectroscopy. *Macromolecules* **2013**, *46* (14), 5561–5569.

(118) Rousseau, M.-E.; Lefèvre, T.; Beaulieu, L.; Asakura, T.; Pézolet, M. Study of Protein Conformation and Orientation in Silkworm and Spider Silk Fibers Using Raman Microspectroscopy. *Biomacromolecules* **2004**, *5* (6), 2247–2257.

(119) Papkov, D.; Pellerin, C.; Dzenis, Y. A. Polarized Raman Analysis of Polymer Chain Orientation in Ultrafine Individual Nanofibers with Variable Low Crystallinity. *Macromolecules* **2018**, *51* (21), 8746–8751.

(120) Takajima, T. *Advanced Fiber Spinning Technology*; Woodhead Publishing, 1994.

(121) Galvis, L.; Dunlop, J. W. C.; Duda, G.; Fratzl, P.; Masic, A. Polarized Raman Anisotropic Response of Collagen in Tendon: Towards 3D Orientation Mapping of Collagen in Tissues. *PLoS One* **2013**, *8* (5), e63518.

(122) Thomas, G. J.; Benevides, J. M.; Overman, S. a; Ueda, T.; Ushizawa, K.; Saitoh, M.; Tsuboi, M. Polarized Raman Spectra of Oriented Fibers of A DNA and B DNA: Anisotropic and Isotropic Local Raman Tensors of Base and Backbone Vibrations. *Biophys. J.* **1995**, *68* (March), 1073–1088.

(123) McGraw, G. E. Investigation of Polyester Structure by Laser Raman Spectroscopy. In *Polymer Characterization: Interdisciplinary Approaches*; Craver, C. D., Ed.; Springer US: Boston, MA, 1971; pp 37–46.

(124) Melveger, A. J. Laser-Raman Study of Crystallinity Changes in Poly(Ethylene Terephthalate). *J. Polym. Sci. Part A-2 Polym. Phys.* **1972**, *10* (2), 317–322.

(125) Louden, J. D. Crystallinity in Poly(Aryl Ether Ketone) Films Studied by Raman Spectroscopy. *Polym. Commun.* **1986**, *27*, 82–84.

(126) Everall, N. J.; Lumsdon, J.; Chalmers, J. M.; Mason, N. The Use of Polarised Fourier Transform Raman Spectroscopy in Morphological Studies of Uniaxially Oriented PEEK Fibres—some Preliminary Results. *Spectrochim. Acta Part A Mol. Spectrosc.* **1991**, *47* (9–10), 1305–1311.

(127) Adar, F.; Noether, H. Raman Microprobe Spectra of Spin-Oriented and Drawn Filaments of Poly(Ethylene Terephthalate). *Polymer (Guildf).* **1985**, *26* (13), 1935–1943.

(128) Bulkin, B. J.; Lewin, M.; DeBlase, F. J. Conformational Change, Chain Orientation, and Crystallinity in Poly(Ethylene Terephthalate) Yarns: Raman Spectroscopic Study. *Macromolecules* **1985**, *18* (12), 2587–2594.

(129) Natarajan, S.; Michielsen, S. Determination of Density and Birefringence of Poly(Ethylene Terephthalate) Fibers Using Raman Microscopy. *J. Appl. Polym. Sci.* **1999**, *73* (6), 943–952.

(130) Schmidt, P.; Hendra, P. J. The Application of Fourier-Transform Raman Spectroscopy to the Determination of Conformation in Poly(ε-Caprolactam) Chains. *Spectrochim. Acta Part A Mol. Spectrosc.* **1994**, *50* (11), 1999–2004.

(131) Everall, N.; Tayler, P.; Chalmers, J. .; MacKerron, D.; Ferwerda, R.; van der Maas, J. . Study of Density and Orientation in Poly(Ethylene Terephthalate) Using Fourier Transform Raman Spectroscopy and Multivariate Data Analysis. *Polymer (Guildf).* **1994**, *35* (15), 3184–3192.

(132) Huang, Y. S.; Koenig, J. L. Raman Spectra of Polyacrylonitrile. *Appl. Spectrosc.* **1971**, *25* (6), 620–622.

(133) Gross, L.; Wang, Z. L.; Ugarte, D.; Mohn, F.; Moll, N.; Heer, W. a; Vincent, P.; Liljeroth, P.; Journet, C.; Meyer, G.; et al. The Chemical Structure of a Molecule Resolved by Atomic Force Microscopy. *Science (80-.).* **2009**, *325* (August), 1110–1114.

(134) Fukuma, T.; Kilpatrick, J. I.; Jarvis, S. P. Phase Modulation Atomic Force Microscope with True Atomic Resolution. *Rev. Sci. Instrum.* **2006**, *77* (12).

(135) Mou, J.; Czajkowsky, D. M.; Zhang, Y.; Shao, Z. High-Resolution Atomic-Force Microscopy of DNA: The Pitch of the Double Helix. *FEBS Lett.* **1995**, *371*, 279–282.

(136) Cerreta, A.; Vobornik, D.; Dietler, G. Fine DNA Structure Revealed by Constant Height Frequency Modulation AFM Imaging. *Eur. Polym. J.* **2013**, *49* (8), 1916–1922.

(137) Rebouillat, S.; Donnet, J. B.; Wang, T. K. Surface Microstructure of a Kevlar* Aramid Fibre Studied by Direct Atomic Force Microscopy. *Polymer (Guildf).* **1997**, *38* (9), 2245–2249.

(138) Dzenis, Y. A.; Reneker, D. H.; Tsukruk, V. V.; Patil, R. Fractal Analysis of Surfaces of Advanced Reinforcing Fibers by Atomic Force Microscopy. *Compos. Interfaces* **1994**, *2* (4), 307–319.

(139) Strawhecker, K. E.; Cole, D. P. Morphological and Local Mechanical Surface Characterization of Ballistic Fibers via AFM. *J. Appl. Polym. Sci.* **2014**.

(140) Sakamoto, H.; Asakawa, H.; Fukuma, T.; Fujita, S.; Suye, S. I. Atomic Force Microscopy Visualization of Hard Segment Alignment in Stretched Polyurethane Nanofibers Prepared by Electrospinning. *Sci. Technol. Adv. Mater.* **2014**, *15* (1), 1–7.

(141) Xu, Y.; Gao, Y.; Wang, X.; Jiang, J.; Hou, J.; Li, Q. Internal Structure of Amorphous Electrospun Nanofiber: Oriented Molecular Chains. *Macromol. Mater. Eng.* **2017**, *302* (7), 1–6.

(142) Chlanda, A.; Kijeńska, E.; Rinoldi, C.; Tarnowski, M.; Wierzchoń, T.; Swieszkowski, W. Structure and Physico-Mechanical Properties of Low Temperature Plasma Treated Electrospun Nanofibrous Scaffolds Examined with Atomic Force Microscopy. *Micron* **2018**, *107* (February), 79–84.

(143) Stockdale, T. A.; Strawhecker, K. E.; Sandoz-Rosado, E. J.; Wetzel, E. D. A Rapid FIB-Notch Technique for Characterizing the Internal Morphology of High-Performance Fibers. *Mater. Lett.* **2016**.

(144) Strawhecker, K. E.; Sandoz-Rosado, E. J.; Stockdale, T. A.; Laird, E. D. Interior Morphology of High-Performance Polyethylene Fibers Revealed by Modulus Mapping. *Polym. (United Kingdom)* **2016**.

(145) Roenbeck, M. R.; Sandoz-Rosado, E. J.; Cline, J.; Wu, V.; Moy, P.; Afshari, M.; Reichert, D.; Lustig, S. R.; Strawhecker, K. E. Probing the Internal Structures of Kevlar®fibers and Their Impacts on Mechanical Performance. *Polym. (United Kingdom)* **2017**.

(146) Sandoz-Rosado, E.; Roenbeck, M. R.; Strawhecker, K. E. Quantifying High-Performance Material Microstructure Using Nanomechanical Tools with Visual and Frequency Analysis. **2018**, *2018*, 1–16.

(147) McDaniel, P. B.; Strawhecker, K. E.; Deitzel, J. M.; Gillespie, J. W. Nanoscale Interfibrillar Adhesion in UHMWPE Fibers. *J. Polym. Sci. Part B Polym. Phys.* **2018**, *56* (5), 391–401.

(148) Hill, R.; Faridur Rahman, F. H. M. Advances in Helium Ion Microscopy. *Nucl. Instruments Methods Phys. Res. Sect. A Accel. Spectrometers, Detect. Assoc. Equip.* **2011**, *645* (1), 96–101.

(149) Livengood, R. H.; Tan, S.; Hallstein, R.; Notte, J.; McVey, S.; Faridur Rahman, F. H. M.

The Neon Gas Field Ion Source - A First Characterization of Neon Nanomachining Properties. *Nucl. Instruments Methods Phys. Res. Sect. A Accel. Spectrometers, Detect. Assoc. Equip.* **2011**, *645* (1), 136–140.

(150) McAllister, Q. P.; Gillespie, J. W.; VanLandingham, M. R. Evaluation of the Three-Dimensional Properties of Kevlar across Length Scales. *J. Mater. Res.* **2012**, *27* (14), 1824–1837.

(151) Camposeo, A.; Greenfeld, I.; Tantussi, F.; Pagliara, S.; Moffa, M.; Fuso, F.; Allegrini, M.; Zussman, E.; Pisignano, D. Local Mechanical Properties of Electrospun Fibers Correlate to Their Internal Nanostructure. *Nano Lett.* **2013**, *13* (11), 5056–5062.

(152) Wang, X.; Xu, Y.; Jiang, Y.; Jiang, J.; Turng, L. S.; Li, Q. Core/Shell Structure of Electrospun Polycarbonate Nanofibers. *Polym. Test.* **2018**, *70* (August), 498–502.

(153) Kocun, M.; Labuda, A.; Meinhold, W.; Revenko, I.; Proksch, R. Fast, High Resolution, and Wide Modulus Range Nanomechanical Mapping with Bimodal Tapping Mode. *ACS Nano* **2017**, *11* (10), 10097–10105.

(154) Pittenger, B.; Erina, N.; Su, C. Application Note # 128 Quantitative Mechanical Property Mapping at the Nanoscale with PeakForce QNM. *Bruker Corp.* **2012**, 1–12.

(155) Kirz, J.; Jacobsen, C. The History and Future of X-Ray Microscopy. *J. Phys. Conf. Ser.* **2009**, *186* (1), 012001.

(156) Macrander, A. T.; Huang, X. Synchrotron X-Ray Optics. *Annu. Rev. Mater. Res.* **2017**, *47* (1), 135–152.

(157) Roth, T.; Detlefs, C.; Snigireva, I.; Snigirev, A. X-Ray Diffraction Microscopy Based on Refractive Optics. *Opt. Commun.* **2015**, *340*, 33–38.

(158) Liu, W.; Ice, G. E.; Tischler, J. Z.; Khounsary, A.; Liu, C.; Assoufid, L.; Macrander, A. T. Short Focal Length Kirkpatrick-Baez Mirrors for a Hard x-Ray Nanoprobe. *Rev. Sci. Instrum.* **2005**, *76* (11), 113701.

(159) Sakdinawat, A.; Attwood, D. Nanoscale X-Ray Imaging. *Nat. Photonics* **2010**, *4* (12), 840–848.

(160) Holt, M.; Harder, R.; Winarski, R.; Rose, V. Nanoscale Hard X-Ray Microscopy Methods for Materials Studies. *Annu. Rev. Mater. Res.* **2013**, *43* (1), 183–211.

(161) Mohacsi, I.; Vartiainen, I.; Rösner, B.; Guizar-Sicairos, M.; Guzenko, V. A.; McNulty, I.; Winarski, R.; Holt, M. V.; David, C. Interlaced Zone Plate Optics for Hard X-Ray Imaging in the 10 Nm Range. *Sci. Rep.* **2017**, *7*, 43624.

(162) Hernández Cruz, D.; Rousseau, M.-E.; West, M. M.; Pézolet, M.; Hitchcock, A. P. Quantitative Mapping of the Orientation of Fibroin β-Sheets in B. Mori Cocoon Fibers by Scanning Transmission X-Ray Microscopy. *Biomacromolecules* **2006**, *7* (3), 836–843.

(163) Ade, H.; Stoll, H. Near-Edge X-Ray Absorption Fine-Structure Microscopy of Organic and Magnetic Materials. *Nat. Mater.* **2009**, *8* (4), 281–290.

(164) Ade, H.; Hsiao, B. X-Ray Linear Dichroism Microscopy. *Science (80-.).* **1993**, *262* (5138), 1427–1429.

(165) Howells, M. R.; Beetz, T.; Chapman, H. N.; Cui, C.; Holton, J. M.; Kirz, J.; Lima, E.; Marchesini, S.; Miao, H.; Sayre, D.; et al. An Assessment of the Resolution Limitation

Due to Radiation-Damage in X-Ray Diffraction Microscopy. *J. Electron Spectros. Relat. Phenomena* **2009**, *170* (1–3), 4–12.

(166) Holton, J. M. A Beginner's Guide to Radiation Damage. *J. Synchrotron Radiat.* **2009**, *16* (2), 133–142.

(167) Egerton, R. F. Control of Radiation Damage in the TEM. *Ultramicroscopy* **2013**, *127*, 100–108.

(168) Coffey, T.; Urquhart, S. .; Ade, H. Characterization of the Effects of Soft X-Ray Irradiation on Polymers. *J. Electron Spectros. Relat. Phenomena* **2002**, *122* (1), 65–78.

(169) Cui, H.; Pashuck, E. T.; Velichko, Y. S.; Weigand, S. J.; Cheetham, A. G.; Newcomb, C. J.; Stupp, S. I. Spontaneous and X-Ray-Triggered Crystallization at Long Range in Self-Assembling Filament Networks. *Science (80-.).* **2010**, *327* (5965), 555–559.

(170) Polvino, S. M.; Murray, C. E.; Kalenci, Ö.; Noyan, I. C.; Lai, B.; Cai, Z. Synchrotron Microbeam X-Ray Radiation Damage in Semiconductor Layers. *Appl. Phys. Lett.* **2008**, *92* (22), 224105.

(171) Dierolf, M.; Menzel, A.; Thibault, P.; Schneider, P.; Kewish, C. M.; Wepf, R.; Bunk, O.; Pfeiffer, F. Ptychographic X-Ray Computed Tomography at the Nanoscale. *Nature* **2010**, *467* (7314), 436–439.

(172) Shapiro, D.; Shapiro, D.; Thibault, P.; Thibault, P.; Beetz, T.; Beetz, T.; Elser, V.; Elser, V.; Howells, M.; Howells, M.; et al. Biological Imaging by Soft X-Ray Diffraction Microscopy. *Pnas* **2005**, *102* (43), 15343–15346.

(173) Lima, E.; Wiegart, L.; Pernot, P.; Howells, M.; Timmins, J.; Zontone, F.; Madsen, A. Cryogenic X-Ray Diffraction Microscopy for Biological Samples. *Phys. Rev. Lett.* **2009**, *103* (19), 198102.

(174) Chu, B.; Hsiao, B. S. Small-Angle X-Ray Scattering of Polymers. *Chem. Rev.* **2001**, *101* (6), 1727–1761.

(175) Schaff, F.; Bech, M.; Zaslansky, P.; Jud, C.; Liebi, M.; Guizar-Sicairos, M.; Pfeiffer, F. Six-Dimensional Real and Reciprocal Space Small-Angle X-Ray Scattering Tomography. *Nature* **2015**, *527* (7578), 353–356.

(176) Hruszkewycz, S. O.; Highland, M. J.; Holt, M. V.; Kim, D.; Folkman, C. M.; Thompson, C.; Tripathi, A.; Stephenson, G. B.; Hong, S.; Fuoss, P. H. Imaging Local Polarization in Ferroelectric Thin Films by Coherent X-Ray Bragg Projection Ptychography. *Phys. Rev. Lett.* **2013**, *110* (17), 1–5.

(177) Holt, M. V.; Hruszkewycz, S. O.; Murray, C. E.; Holt, J. R.; Paskiewicz, D. M.; Fuoss, P. H. Strain Imaging of Nanoscale Semiconductor Heterostructures with X-Ray Bragg Projection Ptychography. *Phys. Rev. Lett.* **2014**, *112* (16), 1–6.

(178) Hruszkewycz, S. O.; Allain, M.; Holt, M. V.; Murray, C. E.; Holt, J. R.; Fuoss, P. H.; Chamard, V. High-Resolution Three-Dimensional Structural Microscopy by Single-Angle Bragg Ptychography. *Nat. Mater.* **2017**, *16* (2), 244–251.

(179) Chapman, H. N.; Fromme, P.; Barty, A.; White, T. A.; Kirian, R. A.; Aquila, A.; Hunter, M. S.; Schulz, J.; DePonte, D. P.; Weierstall, U.; et al. Femtosecond X-Ray Protein Nanocrystallography. *Nature* **2011**, *470* (7332), 73–77.

(180) Seibert, M. M.; Ekeberg, T.; Maia, F. R. N. C.; Svenda, M.; Andreasson, J.; Jönsson, O.; Odić, D.; Iwan, B.; Rocker, A.; Westphal, D.; et al. Single Mimivirus Particles Intercepted and Imaged with an X-Ray Laser. *Nature* **2011**, *470* (7332), 78–81.

(181) Androsch, R.; Schick, C.; Schmelzer, J. W. P. Sequence of Enthalpy Relaxation, Homogeneous Crystal Nucleation and Crystal Growth in Glassy Polyamide 6. *Eur. Polym. J.* **2014**, *53*, 100–108.

(182) Schawe, J. E. K.; Pötschke, P.; Alig, I. Nucleation Efficiency of Fillers in Polymer Crystallization Studied by Fast Scanning Calorimetry: Carbon Nanotubes in Polypropylene. *Polymer (Guildf).* **2017**, *116*, 160–172.

(183) Paolucci, F.; Baeten, D.; Roozemond, P. C.; Goderis, B.; Peters, G. W. M. Quantification of Isothermal Crystallization of Polyamide 12: Modelling of Crystallization Kinetics and Phase Composition. *Polymer (Guildf).* **2018**.

(184) Schawe, J. E. K. Analysis of Non-Isothermal Crystallization during Cooling and Reorganization during Heating of Isotactic Polypropylene by Fast Scanning DSC. *Thermochim. Acta* **2015**, *603*, 85–93.

(185) Koh, Y. P.; Grassia, L.; Simon, S. L. Structural Recovery of a Single Polystyrene Thin Film Using Nanocalorimetry to Extend the Aging Time and Temperature Range. *Thermochim. Acta* **2015**, *603*, 135–141.

(186) Simon, S. L.; Koh, Y. P. The Glass Transition and Structural Recovery Using Flash DSC. In *Fast Scanning Calorimetry*; Springer International Publishing: Cham, 2016; pp 433–459.

(187) Schawe, J. E. K.; Ziegelmeier, S. Determination of the Thermal Short Time Stability of Polymers by Fast Scanning Calorimetry. *Thermochim. Acta* **2016**, *623*, 80–85.

(188) Monnier, X.; Fernandes Nassar, S.; Domenek, S.; Guinault, A.; Sollogoub, C.; Dargent, E.; Delpouve, N. Reduced Physical Aging Rates of Polylactide in Polystyrene/Polylactide Multilayer Films from Fast Scanning Calorimetry. *Polymer (Guildf).* **2018**, *150*, 1–9.

(189) Cebe, P.; Partlow, B. P.; Kaplan, D. L.; Wurm, A.; Zhuravlev, E.; Schick, C. Silk I and Silk II Studied by Fast Scanning Calorimetry. *Acta Biomater.* **2017**, *55*, 323–332.

(190) Monnier, X.; Maigret, J.-E.; Lourdin, D.; Saiter, A. Glass Transition of Anhydrous Starch by Fast Scanning Calorimetry. *Carbohydr. Polym.* **2017**, *173*, 77–83.

(191) Baeten, D.; Mathot, V. B. F.; Pijpers, T. F. J.; Verkinderen, O.; Portale, G.; Van Puyvelde, P.; Goderis, B. Simultaneous Synchrotron WAXD and Fast Scanning (Chip) Calorimetry: On the (Isothermal) Crystallization of HDPE and PA11 at High Supercoolings and Cooling Rates up to 200 °C s^{-1}. *Macromol. Rapid Commun.* **2015**, *36* (12), 1184–1191.

(192) Melnikov, A. P.; Rosenthal, M.; Rodygin, A. I.; Doblas, D.; Anokhin, D. V.; Burghammer, M.; Ivanov, D. A. Re-Exploring the Double-Melting Behavior of Semirigid-Chain Polymers with an in-Situ Combination of Synchrotron Nano-Focus X-Ray Scattering and Nanocalorimetry. *Eur. Polym. J.* **2016**, *81*, 598–606.

(193) van Drongelen, M.; Meijer-Vissers, T.; Cavallo, D.; Portale, G.; Poel, G. Vanden; Androsch, R. Microfocus Wide-Angle X-Ray Scattering of Polymers Crystallized in a Fast Scanning Chip Calorimeter. *Thermochim. Acta* **2013**, *563*, 33–37.

(194) Steyaert, I.; Delplancke, M.-P.; Van Assche, G.; Rahier, H.; De Clerck, K. Fast-Scanning Calorimetry of Electrospun Polyamide Nanofibres: Melting Behaviour and Crystal Structure. *Polymer (Guildf).* **2013**, *54* (25), 6809–6817.

(195) Thomas, D.; Schick, C.; Cebe, P. Novel Method for Fast Scanning Calorimetry of Electrospun Fibers. *Thermochim. Acta* **2018**, *667*, 65–72.

(196) Novotny, L. Chapter 5 The History of Near-Field Optics. *Prog. Opt.* **2007**, *50*, 137–184.

(197) Keilmann, F. Scattering-Type near-Field Optical Microscopy. *J. Electron Microsc. (Tokyo).* **2004**, *53* (2), 187–192.

(198) Ishibashi, T.; Cai, Y. Polarization Properties in Apertureless-Type Scanning Near-Field Optical Microscopy. *Nanoscale Res. Lett.* **2015**, *10* (1).

(199) Zhang, W.; Fang, Z.; Zhu, X. Near-Field Raman Spectroscopy with Aperture Tips. *Chem. Rev.* **2017**, *117* (7), 5095–5109.

(200) Hecht, B.; Bielefeldt, H.; Inouye, Y.; Pohl, D. W.; Novotny, L. Facts and Artifacts in Near-Field Optical Microscopy. *J. Appl. Phys.* **1997**, *81* (6), 2492–2498.

(201) Gucciardi, P. G.; Bachelier, G.; Allegrini, M.; Ahn, J.; Hong, M.; Chang, S.; Jhe, W.; Hong, S. C.; Baek, S. H. Artifacts Identification in Apertureless Near-Field Optical Microscopy. *J. Appl. Phys.* **2007**, *101* (6), 1–8.

(202) Huckabay, H. A.; Armendariz, K. P.; Newhart, W. H.; Wildgen, S. M.; Dunn, R. C. Near-Field Scanning Optical Microscopy for High-Resolution Membrane Studies. In *Nanoimaging*; Humana Press: Totowa, NJ, 2013; Vol. 950, pp 373–394.

(203) Gucciardi, P. G.; Micheletto, R.; Kawakami, Y.; Allegrini, M. Polarization-Modulation Techniques in Near-Field Optical Microscopy for Imaging of Polarization Anisotropy in Photonic Nanostructures. In *Applied Scanning Probe Methods II*; Bhushan, B., Fuchs, H., Eds.; Springer Berlin Heidelberg, 2006; pp 321–360.

(204) Higgins, D. A.; Vanden Bout, D. A.; Kerimo, J.; Barbara, P. F. Polarization-Modulation near-Field Scanning Optical Microscopy of Mesostructured Materials. *J. Phys. Chem.* **1996**, *100* (32), 13794–13803.

(205) Qin, J.; Umeda, N. Near-Field Birefringence Response of IPS Liquid Crystal Thin Film Detected by Bi-SNOM. In *Proc. SPIE 7133, Fifth International Symposium on Instrumentation Science and Technology*; Tan, J., Wen, X., Eds.; 2008; p 71333D.

(206) Dai, S.; Fei, Z.; Ma, Q.; Rodin, A. S.; Wagner, M.; McLeod, A. S.; Liu, M. K.; Gannett, W.; Regan, W.; Watanabe, K.; et al. Tunable Phonon Polaritons in Atomically Thin van Der Waals Crystals of Boron Nitride. *Science* **2014**, *343* (6175), 1125–1129.

(207) Park, K. D.; Raschke, M. B. Polarization Control with Plasmonic Antenna Tips: A Universal Approach to Optical Nanocrystallography and Vector-Field Imaging. *Nano Lett.* **2018**, *18* (5), 2912–2917.

(208) Camposeo, A.; Greenfeld, I.; Tantussi, F.; Moffa, M.; Fuso, F.; Allegrini, M.; Zussman, E.; Pisignano, D. Conformational Evolution of Elongated Polymer Solutions Tailors the Polarization of Light-Emission from Organic Nanofibers. *Macromolecules* **2014**, *47* (14), 4704–4710.

(209) McLeod, A. S.; Kelly, P.; Goldflam, M. D.; Gainsforth, Z.; Westphal, A. J.; Dominguez,

G.; Thiemens, M. H.; Fogler, M. M.; Basov, D. N. Model for Quantitative Tip-Enhanced Spectroscopy and the Extraction of Nanoscale-Resolved Optical Constants. *Phys. Rev. B - Condens. Matter Mater. Phys.* **2014**, *90* (8), 1–17.

(210) Hayazawa, N.; Tarun, A.; Inouye, Y.; Kawata, S. Near-Field Enhanced Raman Spectroscopy Using Side Illumination Optics. *J. Appl. Phys.* **2002**, *92* (12), 6983–6986.

(211) Xue, L.; Li, W.; Hoffmann, G. G.; Goossens, J. G. P.; Loos, J.; De With, G. High Resolution Tip Enhanced Raman Mapping on Polymer Thin Films. *Macromol. Symp.* **2011**, *305* (1), 73–80.

(212) Lee, N.; Hartschuh, R. D.; Mehtani, D.; Kisliuk, A.; Maguire, J. F.; Green, M.; Foster, M. D.; Sokolov, A. P. High Contrast Scanning Nano-Raman Spectroscopy of Silicon. *J. Raman Spectrosc.* **2007**, *38* (6), 789–796.

(213) Cialla, D.; Deckert-Gaudig, T.; Budich, C.; Laue, M.; Möller, R.; Naumann, D.; Deckert, V.; Popp, J. Raman to the Limit: Tip-Enhanced Raman Spectroscopic Investigations of a Single Tobacco Mosaic Virus. *J. Raman Spectrosc.* **2009**, *40* (3), 240–243.

(214) Poborchii, V.; Tada, T.; Kanayama, T. Subwavelength-Resolution Raman Microscopy of Si Structures Using Metal-Particle-Topped AFM Probe. *Japanese J. Appl. Physics, Part 2 Lett.* **2005**, *44* (1–7), 4–7.

(215) Dazzi, A.; Prater, C. B.; Hu, Q.; Chase, D. B.; Rabolt, J. F.; Marcott, C. AFM-IR : Combining Atomic Force Microscopy and Infrared Spectroscopy for Nanoscale Chemical Characterization. *Appl. Spectrosc.* **2012**, *66*, 1365–1384.

(216) Dazzi, A.; Prater, C. B. AFM-IR: Technology and Applications in Nanoscale Infrared Spectroscopy and Chemical Imaging. *Chem. Rev.* **2017**, *117* (7), 5146–5173.

(217) Gong, L.; Chase, D. B.; Noda, I.; Marcott, C. A.; Liu, J.; Martin, D. C.; Ni, C.; Rabolt, J. F. Polymorphic Distribution in Individual Electrospun Poly[(*R*)-3-Hydroxybutyrate- *Co* -(*R*)-3-Hydroxyhexanoate] (PHBHx) Nanofibers. *Macromolecules* **2017**, acs.macromol.7b01086.

(218) Hinrichs, K.; Shaykhutdinov, T. Polarization-Dependent Atomic Force Microscopy–Infrared Spectroscopy (AFM-IR): Infrared Nanopolarimetric Analysis of Structure and Anisotropy of Thin Films and Surfaces. *Appl. Spectrosc.* **2018**, *72* (6), 817–832.

(219) Amarie, S.; Ganz, T.; Keilmann, F. Mid-Infrared near-Field Spectroscopy. *Opt. Express* **2009**, *17* (24), 21794.

(220) Huth, F.; Schnell, M.; Wittborn, J.; Ocelic, N.; Hillenbrand, R. Infrared-Spectroscopic Nanoimaging with a Thermal Source. *Nat. Mater.* **2011**, *10* (5), 352–356.

(221) Huth, F.; Govyadinov, A.; Amarie, S.; Nuansing, W.; Keilmann, F.; Hillenbrand, R. Nano-FTIR Absorption Spectroscopy of Molecular Fingerprints at 20 Nm Spatial Resolution. *Nano Lett.* **2012**, *12* (8), 3973–3978.

(222) Amenabar, I.; Poly, S.; Nuansing, W.; Hubrich, E. H.; Govyadinov, A. A.; Huth, F.; Krutokhvostov, R.; Zhang, L.; Knez, M.; Heberle, J.; et al. Structural Analysis and Mapping of Individual Protein Complexes by Infrared Nanospectroscopy. *Nat. Commun.* **2013**, *4*, 2890.

(223) Amenabar, I.; Poly, S.; Goikoetxea, M.; Nuansing, W.; Lasch, P.; Hillenbrand, R.

Hyperspectral Infrared Nanoimaging of Organic Samples Based on Fourier Transform Infrared Nanospectroscopy. *Nat. Commun.* **2017**, *8*, 14402.

(224) Muller, E. A.; Pollard, B.; Bechtel, H. A.; Blerkom, P. van; Raschke, M. B. Infrared Vibrational Nano-Crystallography and -Imaging. *Sci. Adv.* **2016**, *1601006* (October), 1–7.

(225) Wiens, R.; Findlay, C. R.; Baldwin, S. G.; Kreplak, L.; Lee, J. M.; Veres, S. P.; Gough, K. M. High Spatial Resolution (1.1 Mm and 20 Nm) FTIR Polarization Contrast Imaging Reveals Pre-Rupture Disorder in Damaged Tendon. *Faraday Discuss.* **2016**, *187*, 555–573.

(226) Liu, L.; Dzenis, Y. Simulation of Electrospun Nanofibre Deposition on Stationary and Moving Substrates. *Micro Nano Lett.* **2011**, *6* (6), 408.

(227) Papkov, D.; Maleckis, K.; Zou, Y.; Andalib, M.; Goponenko, A.; Dzenis, Y. Nano to Macro: Mechanical Evaluation of Macroscopically Long Individual Nanofibers. In *MEMS and Nanotechnology, Volume 5 SE - 6*; Prorok, B. C., Starman, L., Eds.; Conference Proceedings of the Society for Experimental Mechanics Series; Springer International Publishing, 2016; pp 35–43.

(228) Lemstra, P. J.; Kirschbaum, R.; Ohta, T.; Yasuda, H. High-Strength/High-Modulus Structures Based on Flexible Macromolecules: Gel-Spinning and Related Processes. In *Developments in Oriented Polymers—2*; Springer Netherlands: Dordrecht, 1987; pp 39–77.

(229) Lemstra, P. J.; Bastiaansen, C. W. M.; Meijer, H. E. H. Chain-extended Flexible Polymers. *Angew. Makromol. Chemie* **1986**, *145* (1), 343–358.

(230) Rastogi, S.; Yao, Y.; Ronca, S.; Bos, J.; Van Der Eem, J. Unprecedented High-Modulus High-Strength Tapes and Films of Ultrahigh Molecular Weight Polyethylene via Solvent-Free Route. *Macromolecules* **2011**, *44* (14), 5558–5568.

(231) Mohan, S. D.; Mitchell, G. R.; Davis, F. J. Chain Extension in Electrospun Polystyrene Fibres: A SANS Study. *Soft Matter* **2011**, *7* (9), 4397.

(232) Smith, S. B.; Bendich, A. J. Electrophoretic Charge Density and Persistence Length of DNA as Measured by Fluorescence Microscopy. *Biopolymers* **1990**, *29* (8–9), 1167–1173.

(233) Ott, A.; Magnasco, M.; Simon, A.; Libchaber, A. Measurement of the Persistence Length of Polymerized Actin Using Fluorescence Microscopy. *Phys. Rev. E* **1993**, *48* (3), R1642–R1645.

(234) Bellan, L. M.; Gross, J. D.; Strychalski, E. A.; Moran-Mirabal, J.; Craighead, H. G. Individually Resolved DNA Molecules Stretched and Embedded in Electrospun Polymer Nanofibers. *Nano Lett.* **2006**, *6* (11), 2526–2530.

(235) Bückers, J.; Wildanger, D.; Vicidomini, G.; Kastrup, L.; Hell, S. W. Simultaneous Multi-Lifetime Multi-Color STED Imaging for Colocalization Analyses. *Opt. Express* **2011**, *19* (4), 3130.

(236) Ries, J.; Udayar, V.; Soragni, A.; Hornemann, S.; Nilsson, K. P. R.; Riek, R.; Hock, C.; Ewers, H.; Aguzzi, A. A.; Rajendran, L. Superresolution Imaging of Amyloid Fibrils with Binding-Activated Probes. *ACS Chem. Neurosci.* **2013**, *4* (7), 1057–1061.

(237) Pinotsi, D.; Kaminski Schierle, G. S.; Kaminski, C. F. Optical Super-Resolution Imaging

of β-Amyloid Aggregation In Vitro and In Vivo: Method and Techniques. In *Methods in molecular biology (Clifton, N.J.)*; 2016; Vol. 1303, pp 125–141.

(238) Kim, N.; Kim, H. J.; Kim, Y.; Min, K. S.; Kim, S. K. Direct and Precise Length Measurement of Single, Stretched DNA Fragments by Dynamic Molecular Combing and STED Nanoscopy. *Anal. Bioanal. Chem.* **2016**, *408* (23), 6453–6459.

(239) Rust, M. J.; Bates, M.; Zhuang, X. Sub-Diffraction-Limit Imaging by Stochastic Optical Reconstruction Microscopy (STORM). *Nat. Methods* **2006**, *3* (10), 793–796.